UNIVERSIDADE DE SANTIAGO DE COMPOSTELA

Electronic, magnetic and structural properties of systems close to a metal-insulator transition: an ab initio study

by

Alberto Piñeiro Rodríguez

A thesis submitted in partial fulfillment for the degree of Doctor of Philosophy

in the

Facultade de Física
Departamento de Física Aplicada

6^{th} March, 2013

USC
UNIVERSIDADE
DE SANTIAGO
DE COMPOSTELA

Declaration of the Advisors

We, DANIEL BALDOMIR FERNÁNDEZ, professor of the Applied Physics Department at the University of Santiago de Compostela, and VICTOR PARDO CASTRO, doctor of Philosophy in Physics by the University of Santiago de Compostela

DECLARE THAT:

- This thesis entitled '*Electronic, magnetic and structural properties of systems close to a metal-insulator transition: an ab initio study*' and the work presented in it was carried out by ALBERTO PIÑEIRO RODRÍGUEZ under our advising.
- The thesis is submitted in partial fulfillment for the degree of Doctor of Philosophy in the Applied Physics Department at the University of Santiago de Compostela.

Signed Prof. Daniel Baldomir Fernández

Signed Dr. Victor Pardo Castro

Santiago de Compostela, 6^{th} March, 2013.

USC
UNIVERSIDADE
DE SANTIAGO
DE COMPOSTELA

Declaration of Authorship

I, ALBERTO PIÑEIRO RODRÍGUEZ, declare that this thesis titled, '*Electronic, magnetic and structural properties of systems close to a metal-insulator transition: an ab initio study*' and the work presented in it are my own. I confirm that:

- This work was done wholly or mainly while in candidature for a research degree at this University.
- Where any part of this thesis has previously been submitted for a degree or any other qualification at this University or any other institution, this has been clearly stated.
- Where I have consulted the published work of others, this is always clearly attributed.
- Where I have quoted from the work of others, the source is always given. With the exception of such quotations, this thesis is entirely my own work.
- I have acknowledged all main sources of help.
- Where the thesis is based on work done by myself jointly with others, I have made clear exactly what was done by others and what I have contributed myself.

Signed:

Date: 6^{th} March, 2013

USC
UNIVERSIDADE
DE SANTIAGO
DE COMPOSTELA

"Patientia, mater scienciae."

USC
UNIVERSIDADE
DE SANTIAGO
DE COMPOSTELA

UNIVERSIDADE DE SANTIAGO DE COMPOSTELA

Abstract

Facultade de Física
Departamento de Física Aplicada

Doctor of Philosophy

by Alberto Piñeiro Rodríguez

This PhD thesis deals with the study of several materials that present different types of metal-insulator transitions (MIT) or are close to one. All of them differ in their chemical and structural properties and also in the way they approach the transition. The basic phenomenology of these transitions and their implications is discussed by means of *ab initio* techniques, based on the DFT framework.

First we have performed electronic structure calculations on the low-dimensional spin-1/2 compound TiOCl at several pressures, finding that the electronic structure is quasi-one-dimensional. The most important magnetic coupling occurs via direct Ti-Ti interactions along the *b*-axis. At about 10GPa, the system presents a spin-Peierls insulator-insulator transition, with an important reduction of the charge gap. On the high-pressure monoclinic phase, TiOCl presents two possible dimerized structures with a long or short dimerization. Long dimerized state occurs above 15GPa, which corresponds to a more standard Peierls distortion. Similar physics has been found in three-dimensional systems like, vanadium-based cubic spinels AV_2O_4. We have studied the effects of pressure in the appearance of a metallization when V-V distance is reduced. The proximity to the transition leads also in this case to a dimerized structure that prevents the system to cross to a metallic phase at moderate pressures. If the system were non-dimerized, a transition to the metallic side would occur.

When a system approaches a MIT, changes in the chemical bond occur that not only affect the electronic properties of materials but it can also drastically change their mechanical properties. This has been analyzed in the case of CrN. We report a drastic, about 25%, reduction of the bulk modulus in CrN at a pressure above ≈ 1 GPa. We demonstrate that this anomalous softening has its origin in a purely electronic effect that lies at the very nature of the chemical bond.

We have also studied perovskite manganites, whose phase diagram includes various MIT. We observed the consequences on the electronic structure of a doping-induced MIT, focusing on the phase separation phenomenon (coexistence of two different electronic phases in the same system). Supercells have been used to simulate a phase-separated state, that occurs at Ca concentrations close to the localized-to-itinerant crossover. We have first considered a model with two types of magnetic ordering coexisting within the same compound, finding it to be unstable. However, a non-isotropic distribution of chemical dopants is found to be the ground state. This leads to regions in the system with different effective concentrations that would always accompany the magnetic phase separation at the same nanometric scale, with hole-rich regions being more ferromagnetic in character and hole-poor regions being in the antiferromagnetic region of the phase diagram.

The last part of the Thesis consists of the study of CoS_2, an itinerant (on the opposite side of the transition) ferromagnet whose magnetic properties can be understood in terms of spin fluctuation theory. We have identified the nesting features in the Fermi surface of the compound, active for long-wavelength spin fluctuations. The electronic structure of the material is close to a half-metal. We show the importance of introducing spin-orbit coupling in the calculations, which partially destroys the half-metallicity of the material. By means of transport properties calculations, we have quantified the influence of spin-orbit coupling in the conductivity at room temperature.

All in all, we have analyzed how a system approaches a metal-insulator transition. In particular, bond-length fluctuations occur that have consequences on structural transition, changes in the electronic structure and the nature of the chemical bond that show up as different electronic/phases with distinct electronic or mechanical properties. We show that these can be manipulated and lead to interesting technological applications.

USC
UNIVERSIDADE
DE SANTIAGO
DE COMPOSTELA

USC
UNIVERSIDADE
DE SANTIAGO
DE COMPOSTELA

Acknowledgements

First of all I would like to thank my Phd Advisor, Prof. Daniel Baldomir Fernández, for giving me the opportunity to start my research career. From the first day, he gave me a lot of advice that helped me to improve my scientific quality, and treated me as a "scientific son". I must give special thanks to Dr. Victor Pardo Castro, who worked together with me as a colleague and friend, and also as co-advisor of my thesis. He taught me everything I know about WIEN2k, *ab initio* calculations and more. Without your help this thesis could not be possible.

I would like to thank all the 26 co-authors who worked with me along these years.

During this stage of my life, I visited some scientific groups for a small time. I should thank Prof. D. I. Khomskii and Prof. Peter Blaha for their reception at Köln and Wien respectively, and helping me to understand the physical properties of several materials.

Special thanks to "The Team", my group mates: Prof. Javier Castro (the critical voice of the group, that pushes us to improve), Dr. Manuel Pereiro (you taught me the meaning of the word "hard-worker"), Dr. Jorge Botana (the best live-wikipedia to know everything), Dr. David Serantes (the philosopher, he needs to check the sources of all the news), MSc. Antía S. Botana (the heart of the group, and the next Doctor of that), and MSc. Iván Conde (the last acquisition of the group, who help us a lot in all about informatics).

Now I wish to thank the group led by Prof. José Rivas (who now is at Braga) for our collaboration. Nowadays, one of his members has started his career as scientific group leader. This is Prof. Francisco Rivadulla, which is one of the most promising scientists of the University of Santiago de Compostela. But I should not forget about Marta, Santi, Manolo and Camilo. We spent a lot of time talking about science, but also sharing experiences in conferences, in the bar and so on.

Part of this thesis is owed to the CESGA research staff, who helped me with my doubts about supercomputing. So, thanks to Andrés and Aurelio.

I would like to thank all the people in the Instituto de Investigacións Tecnolóxicas, led by Prof. Juan E. Arias, and also the members Rafa Fuentes, Marisol Balsa and Emilio Moldes.

I should not forget about my friends during my degree in Physics: Paloma, Tarrío, Saúl, Isa, Ana... Should I mention all of them, I would not finish for a long time. Most of you have accompanied me in the adventure of the Phd degree. Thanks for the great moments we have shared.

Thanks also to Elisardo Temperán, who helped me with the expressions in latin in the thesis.

I would like to thank specially my friends: Emilio (also my cousin and a nice mathematician), Javi (biologist and great fisherman), Belén (English philologist and very good teacher). Whenever we went together to the cinema, or had a beer, or spoke about important (and less important) things, I felt very well. By your side, problems felt smaller.

And finally, but most important, I would like to thank my family. Thanks to my parents, Pepe and Cati. I know it is difficult to understand a "crazy" physicist, but you did it and you told me what I needed to listen every day. You were, are and will always be one of the most important parts of my life.

Thanks also to my brother Carlos. Despite being younger, you teach me new things every day. Special thanks to my girlfriend, Bea. You were a shoulder where I could cry, a friend to laugh and smile, my confidant and definitively my love.

Thanks also to my Grandma, María, and my aunt Begoña, because you always believe in me. And to my godson Juan Alberto, for played with me a lot of weekends and made me feeling happy.

Agradecimientos

En primer lugar quiero dar las gracias a mi director de Tesis, el Profesor Daniel Baldomir Fernández, por darme la oportunidad de empezar mi carrera investigadora. Desde el primer dia, me dió numerosos consejos que me ayudaron a mejorar mi calidad científica, y me trató como un "hijo cientifico". Debo dar un agradecimiento especial al Doctor Victor Pardo Castro, que trabajó conmigo como compañero y amigo, y también como codirector de mi Tesis. El me enseñó todo lo que se sobre el WIEN2k, cálculos *ab initio* y demás. Sin vuestra ayuda esta Tesis no sería posible.

Me gustaría agradecer a los 26 coautores que trabajaron conmigo a lo largo de estos años.

Durante esta etapa de mi vida, visité algunos grupos científicos durante un corto tiempo. Debo agradecer al Profesor D. I. Khomskii y al Profesor Peter Blaha por su acogida en Colonia y Viena respectivamente, y por ayudarme a entender las propiedades físicas de varios materiales.

Un agradecimiento especial para "The Team", mis compañeros de grupo: Prof. Javier Castro (la voz crítica del grupo, que nos empuja a mejorar), Dr. Manuel Pereiro (me enseñaste el significado del trabajo duro), Dr. Jorge Botana (la mejor wikipedia viva para saber cualquier cosa), Dr. David Serantes (el filósofo, que necesita comprobar las fuentes de todas las noticias), MSc. Antía S. Botana (el corazón del grupo, y la próxima Doctora del mismo), y MSc. Iván Conde (la última adquisición del grupo, que nos ayuda mucho en todo lo referente a la informática).

Quiero manifestar mi agradecimiento al grupo liderado por el Profesor José Rivas (que actualmente está en Braga) por nuestra colaboración. Actualmente, uno de sus miembros ha empezado su carrera como lider de grupo científico. Este es el Profesor Francisco Rivadulla, que es uno de los científicos más prometedores de la Universidad de Santiago de Compostela. Pero no me puedo olvidar de Marta, Santi, Manolo y Camilo. Hemos invertido mucho tiempo hablando de ciencia, pero también compartidendo experiencias en congresos, en la cafetería y demás.

Parte de esta Tesis se debe al personal investigador del CESGA, que me ayudaron con mis dudas sobre supercomputación. Por lo tanto, gracias a Andrés y a Aurelio.

Muchas gracias a toda la gente del Instituto de Investigacións Tecnolóxicas, liderados por el Profesor Juan E. Arias, y tambien a los miembros Rafa Fuentes, Marisol Balsa y Emilio Moldes.

No me puedo olvidar de los amigos durante la licenciatura en Física: Paloma, Tarrío, Saúl, Isa, Ana... Si los mencionase a todos, no terminaria en un rato largo. Muchos de vosotros me habeis acompañado en la aventura de la Tesis doctoral. Gracias por todos los buenos momentos que hemos compartido.

Gracias también a Elisardo Temperán, que me ayudó con las expresiones en latin en esta Tesis.

Quiero dar las gracias especialmente a mis amigos: Emilio (también mi primo y un estupendo matemático), Javi (biólogo y un gran pescador), Belén (filóloga inglesa y muy buena profesora). Cada vez que íbamos juntos al cine, o a tomar una cerveza, o hablábamos de cosas importantes (y menos importantes), me sentía muy bien. A vuestro lado, los problemas se sienten mucho más pequeños.

Y finalmente, pero más importante, quiero dar las gracias a mi familia. Gracias a mis padres, Pepe y Cati. Sé que es dificil entender a un físico "loco", pero lo hicisteis y me dijisteis aquello que necesitaba oir todos los días. Vosotros fuisteis, sois y sereis siempre una de las partes más importantes de mi vida.

Gracias también a mi hermano Carlos. A pesar de ser más joven que yo, me enseñas cosas nuevas todos los días. Un agradecimiento especial a mi novia, Bea. Fuiste un hombro sobre el que llorar, una amiga con la que reir y sonreir, mi confidente y definitivamente mi amor.

Gracias también a mi abuela, María, y a mi tía Begoña, porque siempre creiste en mi. Y a mi ahijado Juan Alberto, por jugar conmigo muchos fines de semana y hacerme sentir feliz.

Contents

USC
UNIVERSIDADE
DE SANTIAGO
DE COMPOSTELA

*Dedicated in the loving memory of my grandfather—***Carlos**—*. You were a second father for me.*

USC
UNIVERSIDADE
DE SANTIAGO
DE COMPOSTELA

1 Introduction

1.1 Motivation

The purpose of Science, and particularly of physics, is to find answers to the questions that mankind has posed about the reality that surrounds us. Historically many mysteries were resolved though at the same time a whole new set of questions arose. Each step that science overcomes is an evolution in people's lives, and usually the smallest ones have a big influence in society. This is the main reason that makes a lot of young students want to pursue a Science degree, and even continue after that with a research career: to discover something new.

One of the main aims of Materials Science is the study of compounds with potential technological applications, and to find the adequate material that satisfies a particular industrial need. Up to relatively recent years, this was carried out by measuring the physical properties of several materials, finding and explaining the phenomena that allows them to be used in industry. It is true that scientists also performed analytical calculations, obtaining formulae to describe the main physical properties of materials, but when they wanted to analyze analytically certain problems (such as the many-body problem), they quickly found it was impossible to solve. It is well known that the three-body problem is not solvable analytically. In the beginning of the 20th century, some models appeared to simplify the many-body problem, and since then a lot of theories were develop to minimize the complexity of this problem. But until the first computers were designed scientists could not test them.

Nowadays, the increasing capabilities of modern supercomputers and also the precision attained by the methods and packages used at present, has made possible to study a wide range of materials in very different situations and for many applications. The present situation allows us to dream with the possibility of a computational design of materials.

The so-called strongly correlated materials (that we will describe in detail throughout this Thesis) are a wide class of materials that show unusual electronic and magnetic properties, such as metal-insulator transitions or half-metallicity. We will see below what all this means in more detail, but we can say here that the behavior of their electrons cannot be described effectively in terms of non-interacting particles. This kind of materials often have technologically important applications, such as memristors, smart windows, optical and magnetic sensors, disk read-and-write heads, etc.

The goal of this Thesis is to study this type of materials, specially those which present a metal-insulator transition (or are near it). All the materials studied in this Thesis are chemically and structurally different, but show some similar properties. All of them are close to a metal-insulator transition, that could take place by applying pressure, chemical variations in the dopants, changes in temperature, and even starting from the itinerant side of the transition, the system could show some interesting properties such as half-metallicity or spin-density fluctuations. These are features typical of 3d electron systems, which are the main ones we have studied here. The flexibility of the 3d electrons to behave both as more localized or more itinerant depending on the system they are in makes them more difficult to study but also more interesting in terms of new phenomenology. In the Thesis, first, in Chapter 2, we will study the evolution with pressure of the chemical and electronic structure of the quasi-one-dimensional compound TiOCl, and the evolution of its electronic structure with pressure. After that, we will make an analysis of the effects of applied pressure in two vanadium spinels, MgV_2O_4 and ZnV_2O_4, studying the effects of pressure in the appearance of a metallization (Chapter 3). The study of changes in the variation of the chemical bond close to a metal-insulator transition and its consequences will be seen in Chapter 4, observing variations in the electronic properties of CrN, that are closely linked to dramatic changes in the mechanical properties of this material. We will continue the study of the phenomenology close

to a metal-insulator transition with one of the most heavily studied systems, perovskite manganites, in Chapter 5, observing the implications of doping in approaching the metal-insulator transition, and trying to shed some light in the problem of phase separation and its relationship with doping inhomogeneities. To conclude the Thesis, we will analyze results on an itinerant system, a half metallic one, CoS_2, whose properties are governed by spin density fluctuations.

The importance of the present work is twofold: on the one hand the results and conclusions presented for all the materials studied, that have significantly increased the knowledge the community had of them, but also the confirmation of the reliability of the methods used to calculate. Theory and experiment are in good agreement in all the results presented in the Thesis. While experiment shows important measurements varying temperature, theory helps complementing experiments in pressure studies because measuring the pressure dependence of the various physical variables studied is far from easy, whereas density functional theory techniques can introduce the effect of pressure in a relatively simple way via volume variations, and the same is true with a proper control of doping inhomogeneities or small structural distortions, which is very difficult to do in experiments, but trivial in the calculations. Because the agreement between both experimental and computational data, density functional theory proves to be a reliable tool to acquire new knowledge in materials physics, even in the complicated case of strongly correlated electron systems.

1.2 Electronic structure calculations

The study of electron systems started out in the beginning of the century, with the appearance of Quantum Mechanics. In 1926, the famous time-dependent Schrödinger equation came out as the first tool for predicting the properties of electron systems.

$$i\hbar\frac{\partial\Psi}{\partial t} = -\frac{\hbar^2}{2m}\frac{\partial^2\Psi}{\partial x^2} + V(x)\Psi(x,t) \tag{1.1}$$

The properties of the ground state of the system are described by the wave function Ψ. With this equation, it was possible to solve simple systems as the H atom and even the He atoms or the simplest of the molecules: H_2. An explanation was found for the spectral lines of H and new series of lines were predicted. But it was clear soon that the solution of the Schrödinger equation for many-electron

systems was not possible. Further proposals appeared shortly after, such as the Thomas-Fermi model,[1] published in 1927, only one year later than the Schrödinger equation. This model tries to study a multi-electron system based on the Fermi-Dirac statistics, assuming that it behaves as a homogeneous electron gas. The main inconvenient of the model, apart from being a very crude approximation of an electronic system, is that it does not predict any chemical bond[2] or other fundamental physical magnitudes as the specific heat. However, and probably without knowing it at the time, Thomas and Fermi established the idea of treating all the electronic structure properties of a system based only on one variable, the electron density, and not on the wave function. This model went almost unnoticed at that time, but the idea of using the electronic density would prove successful decades afterwards.

One of the most successful attempts for dealing with many-electron systems was the Hartree-Fock hypothesis, developed in 1930 by Hartree, Fock and Slater.[3, 4] Within this approximation, a multielectron wave function Ψ_{HF} can be calculated as an antisymmetric combination (the so-called Slater determinant) of the wavefunctions ψ_i of the N electrons, called spin-orbitals, composing it, including already the Pauli exclusion principle.

$$\Psi_{HF} = \frac{1}{\sqrt{N!}} det[\psi_1 \psi_2 \cdots \psi_N] \tag{1.2}$$

The Hartree-Fock theory is only approximate by definition, since a particular shape of the all-electron wave function is assumed and, hence, in cases where a big accuracy is needed or when the electron-electron interactions are strong, it is inferior to other methods. It is, however, still widely used at present, even for periodic systems.

1.2.1 Density Functional Theory

Over the past few decades, density functional theory (DFT)[5] has been the most successful, widely used method in condensed-matter physics, which include not only standard bulk materials but also complex systems such as molecules, proteins, films, interfaces and nanoparticles. The main idea of DFT is to describe a many-body interacting system via its particle density and not via its many-body wavefunction. It reduces the 3N degrees of freedom of the N-body system to only three spatial coordinates through its particle density. It is based on the Hohenberg-Kohm theorems.[6] These basically state that the properties of the ground state of a many-electron

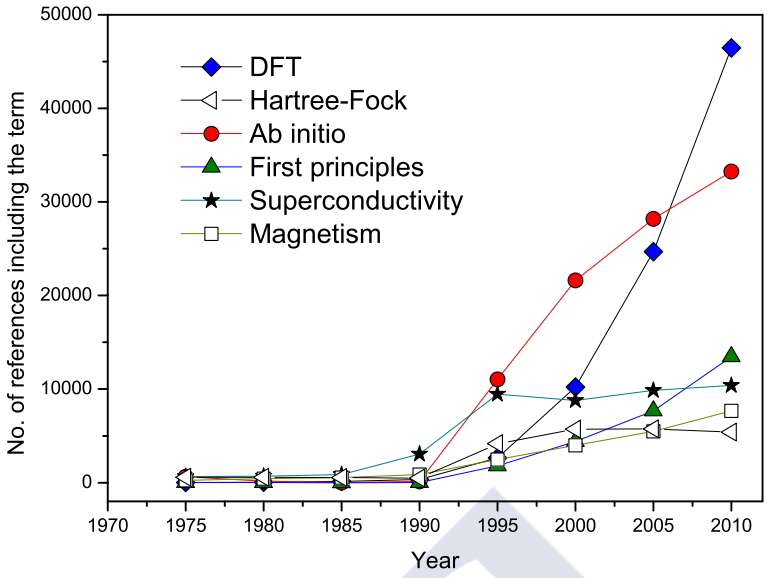

Figure 1.1:
Total number of references (source ISI Web of Science) including the terms "density functional theory", "Hartree-Fock", "ab initio", "first principles", "superconductivity" and "magnetism" over the last 40 years, accumulating every 5 years (the periods 1971-1975, 1976-1980, 1981-1985, 1986-1990, 1991-1995, 1996-2000, 2001-2005 and 2006-2010).

system are determined uniquely by the electron density (first theorem) and that this quantity can be calculated by a variational principle (second theorem). The ground state energy is, hence, a functional of the density and, together with the energy, all the physical properties of the system are also a functional of the density. This simplifies enormously the problem of a many-electron system. The idea of Hohenberg and Kohn became operative with the so-called Kohn-Sham equations that describe a method to actually calculate the electron density in the multi-electronic systems.[7] These two articles were worth a Nobel Prize in Chemistry for Walter Kohn in 1998,[8] after DFT started to become very popular for Materials Science calculations.

Figure 1.1 gives us an idea of the importance of DFT over the last years. This shows the evolution of the number of articles published using DFT compared to other methods such as Hartree-Fock. DFT came out in 1964 and, as can be seen

in the figure, became popular with the appearance of modern supercomputers and personal computers at the end of the eighties. By the mid-90's, it overtook Hartree-Fock as the most popular method for calculating properties of all kinds of materials. The increase in the use of DFT can be seen also by the huge amount of papers including terms as "*ab initio*" or "first principles" (terms that are not exclusive to DFT, but that grew together with it) and the importance of this methodology becomes obvious when compared to the number of articles published in very popular topics as "superconductivity" or "magnetism". In the last ten years, publications using DFT techniques have doubled every 5 years, from 10,000 papers in the period 1995-2000 to 25,000 in the period 2001-2005 and to 45,000 in the period 2006-2010. This is also a consequence of how computationally cheap it is to calculate with DFT codes. The ever increasing capabilities of computers and the evolution of the codes allows to calculate the properties of matter with higher and higher accuracy and, at this stage, we are on the way to design materials theoretically with the desired properties, being DFT an extraordinary tool for that sake. In some respects, this PhD thesis intends to be a work in that direction, as we will see below.

1.2.2 The Born-Oppenheimer approximation

A solid is a collection of heavy, positively charged particles (nuclei) and lighter, negatively charged particles (electrons). If we have N nuclei, we are dealing with a problem of N+ZN electromagnetically interacting particles. This is a many-body problem, and because the particles are so light, quantum mechanics is needed: it is a quantum many-body problem. The exact many-particle Hamiltonian for this system is:

$$\begin{aligned}\hat{H} &= -\frac{\hbar^2}{2}\sum_I \frac{\nabla^2_{\vec{R}_I}}{M_I} - \frac{\hbar^2}{2}\sum_i \frac{\nabla^2_{\vec{r}_i}}{m_e} \\ &- \frac{1}{4\pi\epsilon_0}\sum_{I,i}\frac{e^2 Z_i}{\left|\vec{R}_I - \vec{r}_i\right|} + \frac{1}{8\pi\epsilon_0}\sum_{i\neq j}\frac{e^2}{|\vec{r}_i - \vec{r}_j|} + \frac{1}{8\pi\epsilon_0}\sum_{I\neq J}\frac{e^2 Z_I Z_J}{\left|\vec{R}_I - \vec{R}_J\right|} \quad (1.3)\end{aligned}$$

where the indices I, J run on nuclei, i and j on electrons, the mass of the nucleus at $\vec{R}_I$ is M_I, the electrons have mass m_e and are located at $\vec{r}_i$. The first term is the kinetic energy operator for the nuclei, the second for the electrons. The last three terms describe the Coulomb interaction between electrons and nuclei, between

electrons and other electrons, and between nuclei and other nuclei, respectively. Solving this problem exactly is out of the question.

The Born-Oppenheimer approximation was first introduced in 1927, during the time young Robert Oppenheimer was visiting Europe learning the new quantum theory.[9] The nuclei are much heavier and therefore much slower than the electrons. We can hence "freeze" them at fixed positions and assume the electrons to be in instantaneous equilibrium with them. In other words: only the electrons are kept as players in our many-body problem. The nuclei are deprived from this status, and reduced to being the source of positive charge, they become "external" to the electron cloud. After having applied this approximation, we are left with a collection of NZ interacting negative particles, moving in the (now external or given) potential of the nuclei.

The Born-Oppenheimer approximation has consequences in the Hamiltonian of a many-particle system. The nuclei do not move any more, so their kinetic energy is zero and the first term in Eq. 1.3 vanishes, the last one being reduced to a constant. We are left with the kinetic energy of the electron gas, the potential energy due to electron-electron interactions and the potential energy of the electron in the (now external) potential of the nuclei. We write this formally as:

$$\hat{H} = \hat{T} + \hat{V} + \hat{V}_{ext} \tag{1.4}$$

The significance of the Born-Oppenheimer approximation is to separate the movement of electrons and nuclei. Now we can consider that the electrons are moving in a static external potential V_{ext} formed by the nuclei, which is the starting point of DFT. It is interesting to note here that the kinetic and electron-electron term in Eq. 1.4 depend only on the fact that we are dealing with a many-electron system (and not with a many-proton system for instance, where the strong nuclear force would play a role). They are independent of the particular kind of many-electron system. System-specific information (which nuclei, and on which positions) is given entirely by $\hat{V}_{ext}$.

1.2.3 The Hohenberg and Kohn theorems

The quantum many body problem obtained using the Born-Oppenheimer approximation is much simpler than the original, but still far too difficult to solve. Several methods exist to reduce equation 1.4 to an approximate but tractable form. As

we have mentioned above, a historically very important one is the Hartree-Fock method. It performs very well for atoms and molecules, and is therefore used a lot in quantum chemistry. For solids it is less accurate, however. As Hartree-Fock, DFT is a general method to solve the quantum many body problem. Not only multielectron systems can be studied by means of DFT, a neutron star,[10] e.g., can also be treated using DFT.

DFT was formally established in 1964 with two theorems due to Hohenberg and Kohn,[6] whose formulation is as follows:

First theorem:

There is a one-to-one correspondence between the ground-state density $\rho(\vec{r})$ of a many-electron system (atom, molecule, solid) and the external potential V_{ext}. An immediate consequence is that the ground-state expectation value of any observable $\hat{O}$ is a unique functional of the exact ground-state electron density:

$$< \Psi \left| \hat{O} \right| \Psi >= O[\rho] \tag{1.5}$$

Second theorem:

For $\hat{O}$ being the Hamiltonian $\hat{H}$, the ground-state total energy functional $H[\rho] \equiv E_{V_{ext}}[\rho]$ is of the form:

$$\begin{aligned} E_{V_{ext}}[\rho] &= \underbrace{< \Psi \left| \hat{T} + \hat{V} \right| \Psi >}_{F_{HK}[\rho]} + < \Psi \left| \hat{V}_{ext} \right| \Psi > \\ &= F_{HK}[\rho] + \int \rho(\vec{r}) V_{ext}(\vec{r}) d\vec{r} \end{aligned} \tag{1.6}$$

where the Hohenberg-Kohn density functional $F_{HK}[\rho]$ is universal for any many-electron system. $E_{V_{ext}}[\rho]$ reaches its minimal value (equal to the ground-state total energy) for the ground state density corresponding to V_{ext}.

The implications of these theorems are that the ground state properties are dependent only on the electron density and also that a variational principle would give the electron density of the problem, and hence all the ground state properties.

1.2.4 The Kohn-Sham equations

In 1965, the work of Kohn and Sham[11] put Hohenberg-Kohn theorems into practical use and made DFT calculations possible with even a single personal computer.

This is part of the reason why DFT became the most popular tool for electronic structure calculations.

With Kohn-Sham equations the original many-body system is replaced by an auxiliary independent-particle system, such that the two systems have exactly the same ground state density. It maps the original interacting system with the real potential into a fictitious non-interacting system whereby the electrons move within an effective Kohn-Sham single-particle potential $V_{KS}(\vec{r})$. For the auxiliary independent-particle system, the auxiliary Hamiltonian is

$$\hat{H}_{KS} = -\frac{1}{2}\nabla^2 + V_{KS}(\vec{r}) \tag{1.7}$$

in atomic units $\hbar = m_e = e = 4\pi/\epsilon_0 = 1$. For a system with N independent electrons, the ground state is obtained by solving the N one-electron Schrödinger equations,

$$\left(-\frac{1}{2}\nabla^2 + V_{KS}(\vec{r})\right)\psi_i(\vec{r}) = \epsilon_i\psi_i(\vec{r}) \tag{1.8}$$

where there is one electron in each of the N orbitals $\psi_i(\vec{r})$ with the lowest eigenvalues ϵ_i. These are called Kohn-Sham equations. The density of the auxiliary system is constructed from:

$$\rho(\vec{r}) = \sum_{i=1}^{N} |\psi_i(\vec{r})|^2 \tag{1.9}$$

which is subject to the conservation condition: $\int \rho(\vec{r})d\vec{r} = N$. The non-interacting independent-particle kinetic energy $T_S[\rho(\vec{r})]$ is given by,

$$T_S[\rho(\vec{r})] = -\frac{1}{2}\sum_{i=1}^{N}\int \psi_i^*(\vec{r})\nabla^2\psi_i(\vec{r})d\vec{r} \tag{1.10}$$

which is actually expressed in terms of the one-electron orbitals and not directly as a function of the density.

The ground state energy of the system with the external potential $v(\vec{r})$ can be expressed by the following energy functional:

$$E[\rho] = T[\rho] + \int \rho(\vec{r})v(\vec{r})d\vec{r} + V_{ee}[\rho] \tag{1.11}$$

$T[\rho]$ is the kinetic energy and V_{ee} represents all electron-electron interaction energy. For a non-interacting system, $V_{ee} = 0$.

In DFT, the Kohn-Sham equation is the Schrödinger equation of a fictitious system (the "Kohn-Sham system") of non-interacting particles that generate the same density as any given system of interacting particles. The Kohn-Sham equation is defined by a local effective (fictitious) external potential $V_{KS}(\vec{r})$, in which the non-interacting particles move. In order to find a more explicit representation of the Kohn-Sham potential, the energy functional is rewritten as:

$$E[\rho] = T_{KS}[\rho] + \int \rho(\vec{r})v(\rho)d\vec{r} + J[\rho] + E_{xc}[\rho] \tag{1.12}$$

where $J[\rho]$ is the electronic Coulomb energy,

$$J(\rho) = \frac{1}{2}\int\int \frac{\rho(\vec{r_1})\rho(\vec{r_2})}{|\vec{r_1} - \vec{r_2}|} d\vec{r_1} d\vec{r_2} \tag{1.13}$$

and the new introduced exchange-correlation energy functional ($E_{xc}[\rho]$) in equation 1.12 is defined as:

$$E_{xc}[\rho] \equiv T(\rho) - T_{KS}(\rho) + V_{ee} - J(\rho) \tag{1.14}$$

This quantity collects all non-classical interactions between the electrons and the difference of the kinetic energies of the interacting and non-interacting N electron system. Thus, as commented above, the accuracy of DFT is mainly determined by the quality of the approximation used for the calculation of $E_{xc}[\rho]$. This is the major problem with DFT because the exact functionals for the exchange and correlation are not known except for the free homogeneous electron gas. However, good approximations have been implemented during the last 30 years, and new ones continue to appear.

1.2.5 The exchange-correlation functional

In principle, DFT is an exact theory. However, its implementation requires the knowledge of the energy functional that determines the ground state properties of the N-electron system. In particular, it is necessary to know the so-called exchange-correlation functional, that accounts for the "quantum" effects of the electron-electron interactions within the system. Several approximations exist for calculating these effects. One of the first developed approximations was the local-density

approximation (LDA),[7] where the functional depends solely upon the value of the electronic density at each point in space

$$E_{xc}^{LDA}[\rho] = \int \epsilon_{xc}(\rho)\rho(\vec{r})d\vec{r} \tag{1.15}$$

where $\epsilon_{xc}(\rho)$ is the exchange-correlation energy density. The LDA is so accurate for solids that it is still widely used in condensed matter physics, but however it is less used for atoms and clusters because they bear less equivalence to a uniform electron gas although it is not a bad starting point. It means that the exchange-correlation energy due to a particular density $\rho(\vec{r})$ could be found by dividing the material in infinitesimally small volumes filled with a homogeneous electron gas, that has the same overall density as the original material has in this volume.

A next logical step to improve on the LDA, is to make the exchange-correlation contribution of every infinitesimal volume not only dependent on the local density in that volume, buy also on the density in the neighbouring volumes. It means that the gradient of the density will play a role. This new approximation is the generalized gradient approximation (GGA)

$$E_{xc}^{GGA}[\rho] = \int \epsilon_{xc}^{GGA}(\rho, \nabla\rho)\rho(\vec{r})d\vec{r} \tag{1.16}$$

which introduces the density gradients $\nabla\rho(\vec{r})$ as additional local arguments of the exchange-correlation energy density.

Although GGA performs in general slightly better than LDA, there are a few drawbacks. There is only one LDA exchange-correlation functional, because there is a unique definition for ϵ_{xc}. But some freedom exists in how to incorporate the density gradient, and therefore many versions of GGA exist (and also the so-called meta-GGA functionals). Common GGA functionals are Perdew-Wang[12] and Perdew-Burke-Ernzerhof.[13]

GGA generally works better than LDA in predicting bond length and binding energy of molecules, crystal lattice constants, and so on, especially in systems where the charge density is rapidly varying. However GGA sometimes overcorrects LDA results in ionic crystals where the lattice constants from LDA calculations fit well with experimental data but GGA will overestimate them. Nevertheless, both LDA and GGA perform badly in materials where the electrons tend to be localized and strongly correlated such as transition metal oxides and rare-earth elements and

compounds. This drawback has led scientists to find new approximations beyond LDA and GGA.

Strongly correlated systems usually contain transition metal or rare-earth metal ions with partially filled d or f shells. For dealing with strong electron correlations, where the situation is even more different from a homogeneous electron gas, one of the possible alternatives is the so-called LDA+U approximation[14] to treat the exchange-correlation functional. It is based on the LDA but includes a correlation term, U, imported from the Hubbard model.[15–17]

The method assumes two different electron subsystems:

- localized electrons, with an on-site Coulomb interaction within the same orbital with the form: $\frac{1}{2}U\sum_{i\neq j} n_i n_j$, where n_i, n_j are the orbital occupancies.
- delocalized electrons, that are described by an orbital-independent potential (LDA).

The LDA+U approximation takes into account the orbital dependence of the electron-electron interactions. Let us consider an ion with d electrons as a system with a variable number of electrons and we will use the LDA to approximate the exchange-correlation energy as a function of $N = \sum_i n_i$, but not for the orbital energies (the eigenvalues). Hence, the total energy is, subtracting a term to take double counting into account:

$$E = E_{LDA} - U\frac{N(N-1)}{2} + \frac{1}{2}U\sum_{i\neq j} n_i n_j \tag{1.17}$$

The orbital energies are, then:

$$\epsilon_i = \frac{\delta E}{\delta n_i} = \epsilon_{LDA} + U\left(\frac{1}{2} - n_i\right) \tag{1.18}$$

So, if

$$\left\{ \begin{array}{lcl} n_i = 1 & \Rightarrow & \epsilon_i^{occ} = \epsilon_{LDA} - \frac{U}{2} \\ n_i = 0 & \Rightarrow & \epsilon_i^{unocc} = \epsilon_{LDA} + \frac{U}{2} \end{array} \right\} \tag{1.19}$$

Something similar is done with the potential:

$$V_i(\vec{r}) = \frac{\delta E}{\delta n_i(\vec{r})} = V_{LDA}(\vec{r}) + U\left(\frac{1}{2} - n_i\right) \tag{1.20}$$

This produces a separation in energy between an occupied and an unoccupied level of value U, that gives rise to two energy bands (typically called lower and upper Hubbard bands). This reproduces the physics of the so-called Mott-Hubbard insulators, that are insulating due to this type of electron-electron interaction.

The LDA+U approximation improves qualitatively with respect to LDA in:

- properties of excited states such as energy gaps.
- ground state properties such as magnetic moments or exchange coupling constants.
- it gives more precise results for: orbital polarization, Jahn-Teller distortions or polaron formation.

One of the biggest achievements of the LDA+U method was the prediction of the correct antiferromagnetic insulating state of some transition metal oxides, that is not attainable within LDA or GGA alone. This has made the LDA+U widely used nowadays for calculations on this type of systems: strongly correlated systems in the localized-electron limit.

1.2.6 APW+lo method

The APW+lo (augmented plane wave plus local orbitals) is one of the most efficient methods to solve the Kohn-Sham equations. It is a full-potential (no approximation is made to the shape of the potential or the electron density) and all-electron (all the electrons are included in the calculations: core, semicore and valence electrons are calculated and no pseudopotential is used). It is based on the APW method developed by Slater in 1937.[18] This uses the so-called muffin-tin approximation, that divides the unit cell in two regions: the interstitial part and the muffin-tin spheres centered on the atoms, as can be seen in Figure 1.2. Muffin-tin radii need to be chosen according to atomic sizes.

In the interstitial part, the electron density is decomposed in an expansion of plane waves and within the muffin-tin spheres, a combination of solutions of the radial Schrödinger equation is used:

$$\phi(\vec{r}) = \left\{ \begin{array}{ll} \frac{1}{\Omega^{\frac{1}{2}}} \sum_{\vec{G}} c_{\vec{G}} e^{i(\vec{G}+\vec{k})\vec{r}} & \vec{r} \in I \\ \sum_{lm} A_{lm} u_l(r) Y_{lm}(\vec{r}) & \vec{r} \in MTS \end{array} \right\} \tag{1.21}$$

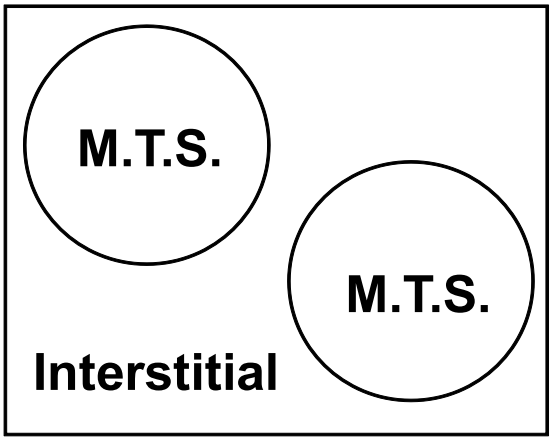

Figure 1.2:
Schematic representation of how the unit cell is divided in the muffin-tin approximation for a case with two atoms. Two different regions appear: the muffin-tin spheres (M.T.S.) around the atoms and the interstitial (I) part between them.

where $\phi(\vec{r})$ is a wave function, Ω is the volume of the cell, $c_{\vec{G}}$ and A_{lm} are the coefficients of the expansion and $u_l(\vec{r})$ is a regular solution of the radial Schrödinger equation. The quality of our description in the interstitial is given by the maximum $\vec{K}$ vector we use for the plane wave expansion. In LAPW language, the quantity that controls basis set size is $R_{mt}K_{max}$ (where R_{mt} is the minimum muffin-tin radius in this case). The value of $R_{mt}K_{max}$ needs to be tested for convergence, and it is usually $6-7$ for the type of systems we will discuss in this thesis.

The main problem with the APW method is that the basis set is energy-dependent (within the muffin-tin spheres). The basis must be evaluated at the eigenergies for being efficient, and hence, it must be recalculated at every iteration. A first attempt to create an energy-independent basis set was developed in the seventies by Ole Andersen among others,[19, 20] the so-called LAPW method.

A different way to "linearize" the APW method is the APW+lo method.[21] This has been proven to be much faster and efficient than other linearizations of the APW method.[22] It adds so-called local orbitals (local meaning that they vanish at the interstice) to the basis set. These look like:

$$\phi(\vec{r},\vec{k}) = \left\{ \begin{array}{ll} 0 & \vec{r} \in I \\ (a_L^{lo} u_l(r,E_l) + b_L^{lo} \dot{u}_l(r,E_l)) Y_L(\vec{r}) & \vec{r} \in MTS \end{array} \right\} \qquad (1.22)$$

where a_L^{lo} and b_L^{lo} are coefficients of the expansion and E_l are the linearization energies where the solutions of the radial Schrödinger equation are evaluated. The APW's are, hence, evaluated at a fixed energy (basis set does not need to be updated at every iteration) and the flexibility is added by including these local orbitals in the basis set.

1.2.7 WIEN2k code: computational details

All the calculations in this Thesis were carried out using a full-potential, all-electron scheme, electronic structure calculations based on the density functional theory[6] utilizing the Augmented Plane Wave + local orbitals (APW+lo) method[21] using the WIEN2k software.[23, 24] The WIEN2k package is a computer program written in Fortran which performs quantum mechanical calculations on periodic solids. It uses the full-potential (linearized) augmented plane-wave and local-orbitals [FP-(L)APW+lo] basis set to solve the Kohn-Sham equations of density functional theory. Nowadays there are more than 1800 licenses of this code worldwide.

This package allows to study most of the electronic structure properties of a crystalline solid: electron density, density of states (DOS), various types of spectra, magnetism (ferromagnetic, antiferromagnetic and non-magnetic configurations), non-collinear magnetism, band structure, Fermi surface, different exchange-correlation potentials including the local density approximation (LDA), various generalized gradient approximation (GGA) (Perdew-Wang[12] or Perdew-Burke-Ernzerhof[13]), meta-GGA[25, 26] and the LDA+U method.[14]

In the case of this Thesis, the exchange-correlation potential utilized in most of the calculations was the Perdew, Burke and Ernzerhof (PBE) version of the general gradient approximation (GGA).[13] Geometry optimizations were carried out minimizing the forces in the atoms and the total energy of the system. The parameter $R_{mt}K_{max}$ controls the size of the plane-wave basis, and is defined as the product of the plane-wave cut-off and the smallest atomic-sphere radii (muffin-tin radii). We have used an appropriate sampling of the full Brillouin zone for electronic structure calculations and geometry optimization in all the cases. The parameters of our calculations [27] depend on the type of calculation but for any of them we converged with respect to the k-mesh and to $R_{mt}K_{max}$.

For modelling the behaviour of the d electrons of systems in this Thesis, we included the strong correlation effects by means of the Local Density Approximation

plus Hubbard U (LDA+U) scheme,[28] where the correlation effects were controlled by an effective U ($U_{eff} = U - J$), being U the on-site Coulomb repulsion and J the on-site exchange constant. In all the calculations we have taken J as $J = 0$, as is common practice in literature.[29] The value of U was chosen based on the correct reproduction of experimental measurements. The parameters of our calculations were fully converged for every particular case to the required precision.

For the calculations of transport properties we utilized the BoltzTraP code,[30] that uses the energy bands obtained from the WIEN2k software and performs a semiclassical calculation to solve Boltzmann equation within the constant scattering time approximation. For this type of calculation a very fine sampling of the Brillouin zone is required, well beyond what is needed for a self-consistent calculation.

1.3 Localized and Itinerant electrons

1.3.1 Itinerant Systems

The expressions "delocalized", "itinerant" and "band-like" have all come to refer to magnetic systems in which the spin-polarized density cannot be neatly assigned to a given ion or to a recognizable atomic (ionic) configuration. The extreme limit of an itinerant magnetic system would be a spin polarized uniform electron gas (with a similarly uniform positive background). The eigenstates of a non-interacting, homogeneous electron gas are plane waves and therefore maximally distributed throughout the system. If the interactions between electrons are assumed to be highly screened and treated as a perturbation, the wave functions will still be very plane-wave-like and extended. In any real system, the background is not a constant positive charge density, but rather a configuration of periodic ion cores. The atomic functions which are eigenstates of isolated atoms are strongly hybridized in itinerant systems. Hybridization broadens the electronic bands and delocalizes the electrons. The stronger the hybridization, the more the effect of the ion cores is masked and the more band-like the magnetic picture becomes. Eventually, the plane wave picture is more accurate than the atomic picture and the magnetic moment is carried by wave functions which are spread throughout the crystal. Though a crossover region exists, one can say that metallic magnets are generally in the itinerant-electron limit, while insulators are on the localized one.

An important feature of the delocalized magnetic systems is the disappearance of the orbital angular momentum. The total magnetic moment in an atom is given by $\vec{M} = \mu_B(2\vec{S} + \vec{L})$, where the 2 is the spin g-factor ratio. The total angular momentum is given by $\vec{J} = \vec{L} + \vec{S}$. Hund's rules can be used to determine how spin and angular momentum combine to produce the total moment. In itinerant systems the picture is quite different. Hund's rules which often work in extended systems, provided the orbitals are atomic-like, are completely invalid when the orbitals are not well localized. The orbital angular momentum, $\vec{L}$, is no longer a good quantum number, as the electron's environment is not spherical. Electrons are not localized to any given ion core and therefore the potential they experience is hugely distorted from the atomic one by the crystal electric field, caused by the static arrangement of nearest neighbour ions. This results in a cancellation of orbital angular momenta, known as "quenching". To a good degree of accuracy in many itinerant (and also localized) electron systems, $\vec{M} = 2\vec{S}$ and $\vec{J} = \vec{S}$.[31]

1.3.1.1 Treatment of Itinerant Systems

Itinerant magnetic systems are well treated by conventional first principles band theory methods. The main approximation of current DFT methods is the LDA. As mentioned above, the LDA uses an exchange-correlation potential borrowed from the homogeneous electron gas, rather than employing the accurate (but completely unknown) non-local potential that exists in reality. The closer a real system is to the homogeneous electron gas, the less error is introduced into the calculation through the use of the LDA. Delocalized electrons are generally weakly correlated with one another such that the underestimation of correlation effects inherent to the LDA does not significantly affect the accuracy of the calculated properties.

Some aspects of itinerant systems can be captured by model calculations (also for localized ones). The tight binding model and all its relatives for localized systems (Hubbard model, t-J model, etc) can reproduce features of delocalized systems by correctly modeling the hybridization of atomic-like orbitals. However, this involves parameters which are not known beforehand (without input from a first-principles band calculation) and must be guessed or adjusted to fit experimental data. If the hybridization is due to a large number of atomic-like orbitals the fitting process can become cumbersome.

Itinerancy is not a well-defined property, nor can clear lines necessarily be drawn between it and localized systems. There are systems which exhibit behaviours associated with both itineracy and localization. Certainly there is no ironclad way of identifying *a priori* whether a system is band-like enough to be modeled accurately using DFT methodology. Often, after a system is shown to be tractable by band theory, it inherits the classification of itinerant electron system.

1.3.2 Localized Systems

In contrast to the itinerant systems, magnetic compounds which are classified as localized have magnetic moments that are well-defined in real space. The orbitals which are spin-polarized can be localized within some radius and connected to a particular ion or ions in the crystal. A term in the inverse susceptibility which falls off $\approx 1/T$ (i.e. according to the Curie Law) can be regarded as experimental evidence of a local magnetic moment.[31] To discuss local moments in a general way, it is helpful to define two terms, with a picture of periodic ions containing atomic-like orbitals in mind. The first term, called t, which describes the tendency of an electron to hop from one atom site to another. This tendency is governed by the overlap of orbitals located on the two sites in question. One can often say that bandwidth (W) is related directly to t, in the form of the simplest band in one dimension: $\epsilon_k = tcos(k_a)$, hence $W = 2t$ (the smaller the hopping, the smaller W and the more localized the electrons are). This will be a common motif throughout this thesis. The second term, named U, which is the repulsion energy (Coulomb energy) between two electrons which occupy orbitals on the same ion. If t is large compared to U, there is little price to be paid for double occupancy of a single site and electrons hop from site to site continuously and cannot be said to be localized. In systems where t is large, bands will disperse strongly and the density of states will be broad. In the opposite limit, U is much larger than t and the price of double occupancy is large. Electrons prefer to stay on a single ion, rather than hop to another which already contains an electron. The extent to which a system is localized can be gauged by the ratio U/t.

In a localized picture, if the electrons are screened from their surrounding crystal fields, Hund's rules apply (electrons are sharing an ion) and partially filled shells on each ion will have aligned spins. In addition, the orbital angular momentum, $\vec{L}$ will

be approximately a good quantum number, as the potential felt by localized electrons is approximately spherical. The total angular momentum $\vec{J}$ and the magnetic moment $\vec{M}$ will involve both the spin and angular moments. In many localized systems, particularly those involving very heavy ions, the spin-orbit interaction is extremely important and in f-electron systems, it generally dominates the crystal field effect. d-electron systems, however, even if they act as localized electrons, will always be substantially spread out to feel the crystal field strongly.

1.3.2.1 Treatment of Localized Systems

The energy U which allows to localize electrons is also a gauge of correlation. The exchange-correlation potential of the LDA is based on a homogeneous gas of electrons bearing little resemblance to electrons localized near specific ions. Correlation between these localized electrons will no doubt be strongly underestimated through application of the LDA. The degree to which the LDA fails in localized magnetic systems depends largely on the extent of the localization. At least, the LDA underestimates the gap in insulators, sometimes very badly. The worst results are obtained in d- and f-electron systems with partially filled shells.

The biggest failure of the LDA is the wrong prediction of correlated insulators as metallic, due to an underestimation of electron correlation effects. The appearence of partly filled bands at the Fermi level needs to be connected by, e.g., adding a U-term that produces a lower-lying fully occupied band and a higher-lying fully unoccupied band that mimics the physics of the lower and upper Hubbard bands typical of the Hubbard model. This is what the LDA+U method that we described above tries to do.

Model Hamiltonians, such as the Hubbard model, have had great success with the same systems which are badly described by the LDA. The different flavours of the Hubbard model provide a good description of systems in the large U/t limit. There are many models derived from or based on the Hubbard model, the vast majority of which are unsolvable except in very specific instances. However, the appearance of newer and better computational tools gives an approximate solution to this and other model Hamiltonians.

This PhD Thesis will be devoted to the study of systems mainly formed by 3d electrons, whose electronic properties reside in the vicinity of a metal-to-insulator transition, e.g. small changes in those systems could make them behave as localized

or itinerant. We will explore the electronic structure of various of these compounds where pressure, chemical doping or temperature can induce a transition from a more localized to a more itinerant behaviour, and this shows up in the electronic properties in terms of structural distortions, magnetic transitions, changes in the chemical bond or even phase separation.

In the following Chapters we will discuss all this in a little more detail, focusing on different materials.

2

Pressure effects in 1-D electronic system TiOCl

2.1 Introduction

TiOCl is a layered Mott insulator at room temperature, with Ti^{3+} cations in a $3d^1$ configuration. In recent years, much attention has been drawn to the oxyhalides TiOCl and TiOBr, specially after the finding of these materials undergoing a spin-Peierls[1] transition at low temperature[32] brought about by the strong one dimensionality of the material. The low-dimensional spin-1/2 compound TiOCl shows two consecutive phase transitions at the incommensurate spin-Peierls temperature ($T_{ISP} \approx 91K$) and at the commensurate spin-Peierls temperature ($T_{SP} \approx 66K$).[33, 34] A coupling of a one-dimensional (1-D) antiferromagnetic (AF) $S = \frac{1}{2}$ chain with the lattice results in a spin-Peierls transition with a nonmagnetic (singlet) dimerized ground state. $CuGeO_3$ was the first well-established example for such a transition in an inorganic compound,[35–37] and TiOCl is an even more intricate case.

On the other hand, Kuntscher et al. [38] observed a strong suppression of the transmittance and an abrupt increase of the near infrared reflectance above ≈ 10 GPa in TiOCl. These effects were interpreted as a pressure-induced metallization of the 1-D chain, but in Kuntscher's measurements a Drude peak does not appear

[1] A Peierls transition or Peierls distortion is a distortion of the periodic lattice of a one-dimensional (1-D) crystal. Atomic positions oscillate so that the perfect order of the 1-D crystal is broken. Such an instability triggers a charge ordering phenomenon and a metal-insulator phase transition, called Peierls transition. A spin-Peierls transition corresponds to the dimerization of a one-dimensional $S = 1/2$ antiferromagnetic chain coupled to a three dimensional elastic medium.

(which must be present in an insulator-metal transition when metallicity is reached). Recently, the strong suppression of the electronic gap above $\approx$ 12 GPa was confirmed directly through high-pressure resistivity,[39] although the semiconducting behaviour at high pressures is still maintained ($E_g \approx 0.3$ eV). On the other hand, Blanco-Canosa et al. [40] found evidences of a spin-Peierls to Peierls transition as a function of pressure due to an enhanced dimerization of the Ti chain along the *b*-axis that puts the material close to the itinerant electron limit. This effect was observed previously in other similar materials near a metal-insulator transition.[41–43]

In this Chapter we discuss our *ab initio* calculations on the evolution with pressure of the chemical and electronic structure of TiOCl. It is very important to corroborate the quasi-1-D electronic nature and to study the evolution of the transition temperatures with pressure. We will show here that the structural transition from the low-pressure orthorhombic to the high-pressure monoclinic dimerized phase is probably more complex than anticipated, due to the possible existence of two dimerized phases on the monoclinic structure with different short and long bonds between Ti atoms along the b-direction chains.

2.2 Computational details

As we saw in section 1.2.7, we have used the WIEN2k software[23, 24] to calculate the properties of the material.

Local Density Approximation plus Hubbard U (LDA+U) scheme[28] was used for modelling the behaviour of the d electrons of the system. A value of $U_{eff} = 5$ eV was used in the calculations, since it reproduces the ambient pressure band gap, but the results presented are consistent for values of U_{eff} from 4 to 7 eV. The structural minimization was carried out using the General Gradient Approximation in the Perdew Burke and Ernzerhof (GGA-PBE) scheme.[13] $R_{mt}K_{max} = 6.0$ is chosen for all the calculations. We used a k-mesh in a $6 \times 5 \times 5$ sampling of the full Brillouin zone, and have calculated over 75 k-points in the irreducible Brillouin zone (200 total k-points), where convergence was achieved. Local orbitals were added for a bigger flexibility in dealing with the semi-core states: 3s and 3p for Ti; 2s for O; and 3s for Cl. Muffin-tin radii chosen were the following: 1.94 a.u. for Ti, 1.72 a.u. for O and 2.13 a.u. for Cl. These muffin-tin radii were reduced by 3 % for the structural relaxation calculations. The parameters of our calculations were fully converged for every particular case to the required precision.

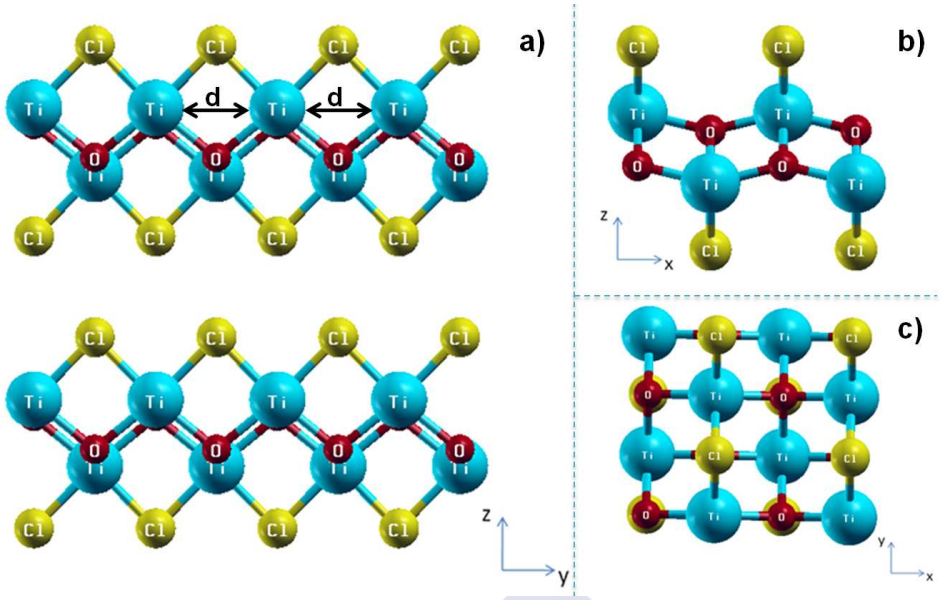

Figure 2.1:
Structure of the TiOCl compound on the ambient pressure orthorhombic phase. The value of the Ti-Ti distance along b-axis is $d = 3.36$ Å.

2.3 Structure

2.3.1 Orthorhombic phase

TiOCl crystal structure consists of an orthorhombic quasi-two dimensional network [34] (FeOCl-type) where buckled Ti-O bilayers within the ab plane are well separated by Cl^- ions as it can be seen in Figure 2.1 a). Ti atoms form 1-D chains along b-direction, and the planes pile up along the c-axis. Each Ti atom is coordinated by a heavily distorted octahedron formed by four O and two Cl atoms. Magnetic neighbours are two Ti along b (showing a large hopping), two Ti along a (far enough for neglecting that magnetic interaction) and four Ti closest atoms out of the ab plane.

TiOCl crystallizes in an orthorhombic space group (different lattice parameters, $a \neq b \neq c$, and the three lattice vectors remain mutually orthogonal, $\alpha = \beta = \gamma = 90^o$). Lattice parameters were measured using high-pressure X-ray diffaction for pressures up to 9 GPa, in the orthorhombic space group Pmmm.[40] The low

Table 2.1:
Experimental atomic positions in the orthorhombic phase of TiOCl obtained by neutron powder diffraction and calculated atomic positions after a structural relaxation based on the experimental structure (space group Pmmm, whith lattice values of $a = 3.79$ Å, $b = 3.37$ Å and $c = 8.06$ Å).

	Position	Experimental atomic positions	Relaxed atomic positions
Ti	2(b)	(0.0000, 0.5000, 0.1220)	(0.0000, 0.5000, 0.1133)
Cl	2(a)	(0.0000, 0.0000, 0.3273)	(0.0000, 0.0000, 0.3200)
O	2(a)	(0.0000, 0.0000, 0.9350)	(0.0000, 0.0000, 0.9435)

pressure structure shows the lattice values of $a = 3.79$ Å , $b = 3.37$ Å and $c = 8.06$Å. Experimental atomic positions can be seen in Table 2.1.

Based on this experimental data, we made a structural relaxation of the structure, using the GGA-PBE exchange-correlation potential. This approximation is widely used in structural relaxation calculations of strongly correlated electron systems, which are formed by compounds with 3d electrons in the valence band. After minimizing interatomic forces, the relaxed atomic positions obtained is presented in Table 2.1.

We have observed that the atomic position variation of Ti atoms is the largest one ($\approx 7\%$) compared with the variation on Cl atom ($\approx 2\%$) or O atom ($\approx 0.2\%$). The largest contributive forces in the structure came from the magnetic Ti atoms, as it is expected.

The distance between two Ti atoms along the *b*-direction chain at room pressure is 3.36 Å. This distance is higher than metal Ti-Ti bond length, estimated around 2.95 Å. The distance of the Ti atoms along the *a*-direction is 3.79 Å, while the 4 Ti atoms which appear to be along the *ab*-direction in Figure 2.1 c), but really are out of the *ab*-plane, are the nearest to the reference Ti atoms, showing a distance of 3.12 Å.

We employ the experimental lattice parameters at several pressures (4, 7 and 9 GPa), use the same starting atomic positions than the low pressure one (neutron difraction data shows the same atomic positions for all pressures) and we repeat the structural relaxation calculations, minimizing interatomic forces for each pressure. The values of the lattice parameters of the orthorhombic structure of TiOCl at all

Table 2.2:
Structural data of the orthorhombic phase of TiOCl at several pressures. Upper table shows the lattice parameters of the structures. Bottom table shows the distances between the nearest Ti atoms along the *a*-direction, *b*-direction and *ab*-direction out of *ab*-plane (called short distance). In this bottom table, the number of nearest Ti atoms along the indicated directions are written in parentheses.

P (GPa)	*a* (Å)	*b* (Å)	*c* (Å)
0	3.79	3.37	8.06
4	3.68	3.20	7.36
7	3.66	3.15	7.23
9	3.65	3.12	7.10

P (GPa)	Ti-Ti (Å) (2) along the *a*-axis	Ti-Ti (Å) (2) along the *b*-axis	Ti-Ti (Å) (4) short distance
0	3.79	3.36	3.12
4	3.68	3.20	3.10
7	3.66	3.15	3.09
9	3.65	3.12	3.07

the pressures mentioned above are presented in Table 2.2. This table also presents the calculated Ti-Ti distances along the different directions.

It can be observed that the structure is very compressible along the *c*-direction, and compressibility is lower along the directions which form the *ab* bilayers. This is because of the large distance between the biplanes along the *c*-direction and their low interaction (van der Waals-type), i.e. the two-dimensional behaviour of the compound (see Figure 2.1).

2.3.2 Monoclinic phase

TiOCl presents a structural transition to a monoclinic phase at low temperature,[44] which is associated to the spin-Peierls transition.[33] High-pressure X-ray diffraction at 15 GPa confirms that this monoclinic structure also occurs at high pressure at ambient temperature.[40, 45] As it can be seen in Figure 2.2 the Ti-O bilayers inside the *ab* plane are well separated by Cl^- ions. These bilayers are piled up along the *c*-axis. Ti atoms form 1-D dimerized chains along the *b* direction. Each Ti is

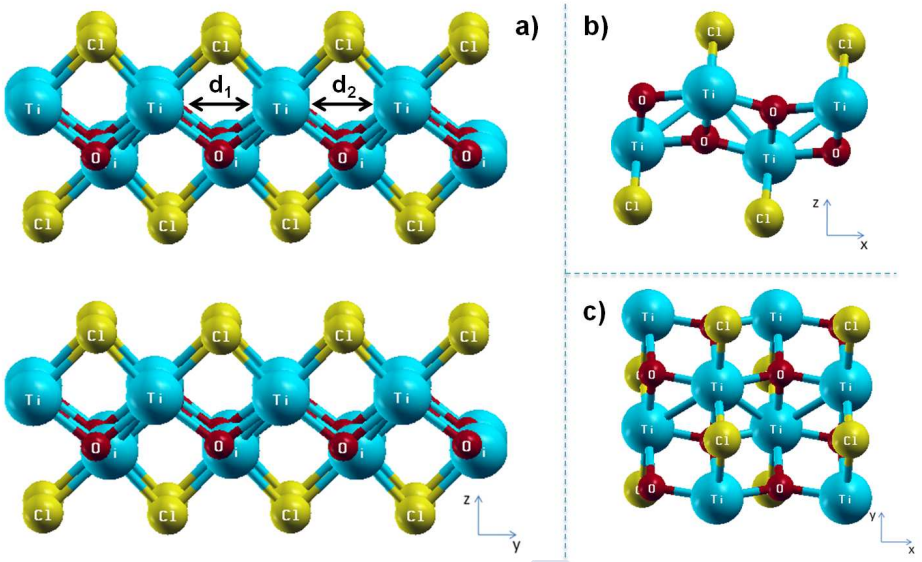

Figure 2.2:
Structure of the TiOCl compound on the high-pressure monoclinic phase. Values of the Ti-Ti distances along the b-chains are $d_1 = 3.25$ Å and $d_2 = 3.39$ Å.

surrouded by a distorted octahedral environment, formed by four O atoms and two Cl atoms. The Ti magnetic environment is formed by two Ti along the b direction, two Ti along the a direction and four Ti along the ab-direction out of the ab-plane.

The unit cell which determines the structure of the material is a monoclinic one (which has different cell parameters: $a \neq b \neq c$ and two equal perpendicular axes: $\alpha = \gamma = 90^o$, $\beta \neq 90^o$). In this work we have used experimental lattice parameters at pressures P = 0 GPa [34] and P = 15 GPa.

We have also studied this monoclinic phase at intermediate pressures (this phase is stable below room temperature for P < 15 GPa). For carrying out the corresponding *ab initio* calculations at the pressures presented, we have made an extrapolation of the lattice parameters in the space group $P2_1/m$ based on the study of its evolution performed by Forthaus *et al.*,[39] because it was found by those authors to be the low temperature, P = 0 GPa phase, and our understanding is that this same symmetry occurs at high pressure and room temperature (and above). We will argue more of this below. We initially take the atomic positions of the orthorhombic structure, and we construct a 1×2×1 supercell, which implies a doubled value for the b parameter. In all the monoclinic structures we have used the value of the angle

Table 2.3:
Lattice parameters of the monoclinic phase of TiOCl at several pressures. Column 3 shows the b lattice parameters of the structures in the 1×2×1 supercell.

P (GPa)	a (Å)	b (Å) (× 2)	c (Å)
0	3.79	6.74	8.06
4	3.72	6.67	7.77
7	3.67	6.66	7.56
10	3.62	6.65	7.36
15	3.54	6.63	7.02
20	3.45	6.61	7.69

$\beta = 98.893^o$, which has been measured experimentally at P = 15 GPa (the main conclusions hold correct without an optimization of this angle for each pressure). In order to find the atomic positions of Ti atoms which allow a dimerized structure, we make a displacement on the atomic positions of Ti atoms along the b-direction. Then, we make a structural relaxation of the compound, which yields two possible dimerized states: short one and long one. In the short dimerized state we observed short Ti-Ti bonds (≈ 3.25 Å) and long Ti-Ti bonds (≈ 3.35 Å) along the b-axis, while in the long dimerized state we observed very short Ti-Ti bonds (≈ 2.95 Å) and a very long Ti-Ti bonds (≈ 3.67 Å) along the same b-axis.

The calculated lattice parameters at different pressures are presented in Table 2.3.

2.4 Discussion

2.4.1 Electronic structure

An ionic picture of TiOCl with the usual valences for O^{2-} and Cl^{-} anions yields a Ti^{3+} ionic configuration. Because of this, Ti atoms contribute with only one electron in the valence band. The family of TiOX (X = Cl or Br) are low-dimensional spin-1/2 compounds, whose electronic configuration is $3d^1$. We have performed all the electronic structure calculations within the LDA+U approximations to model the exchange-correlation functional potential. Based on this LDA+U calculations in

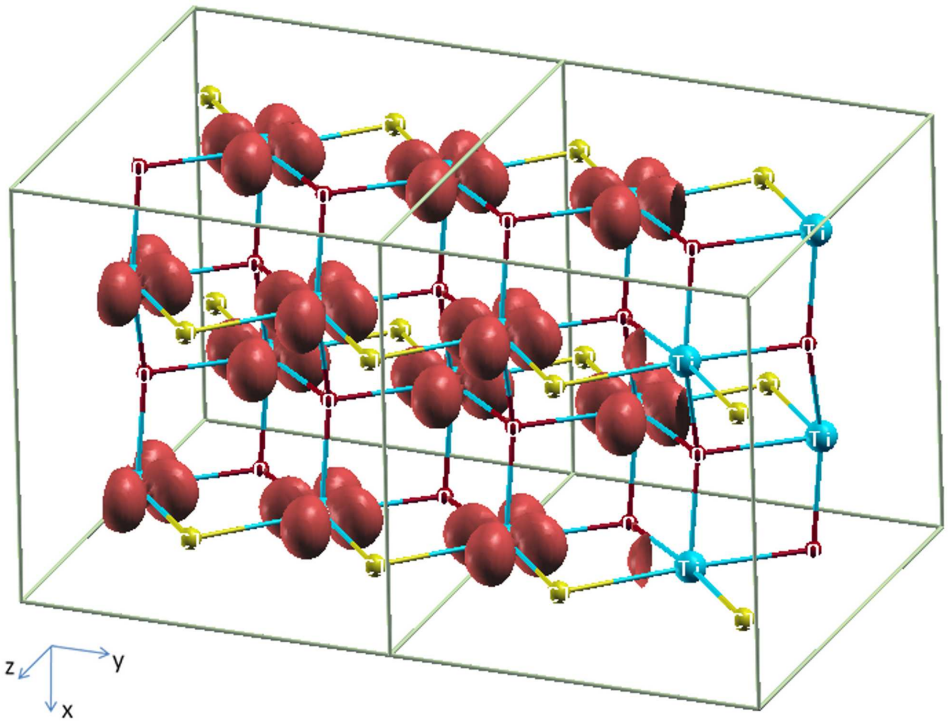

Figure 2.3:
Electron spin density plot of TiOCl in the orthorhombic structure (isosurface at 0.08 e/Å) produced using XCrysDen.[47] Yellow and small red spheres correspond to Cl and O atoms, respectively. x, y and z-axes are associated to a, b and c directions, respectively. Most of the spin-density shows the occupied Ti d_{yz} orbital.

the orthorhombic structure at P = 0 GPa, we have plot the electron spin density of TiOCl,[46] in Figure 2.3.

This plot helps us to understand the electronic structure in the vicinity of the Fermi level. We can see the electronic structure of TiOCl and its quasi-one-dimensional nature. The Ti^{3+} (d^1) ions have one t_{2g} orbital occupied (d_{yz}) with a large hopping integral along the b-direction of the crystal, leading to a highly 1-D electronic structure. The interactions along the a-axis are very small due to the symmetry of the occupied orbital; along the c-axis, interactions are negligible due to the large Ti-Ti distance (about 8.1 Å). Hence, there is an electronic reduction of the dimensionality of the system.

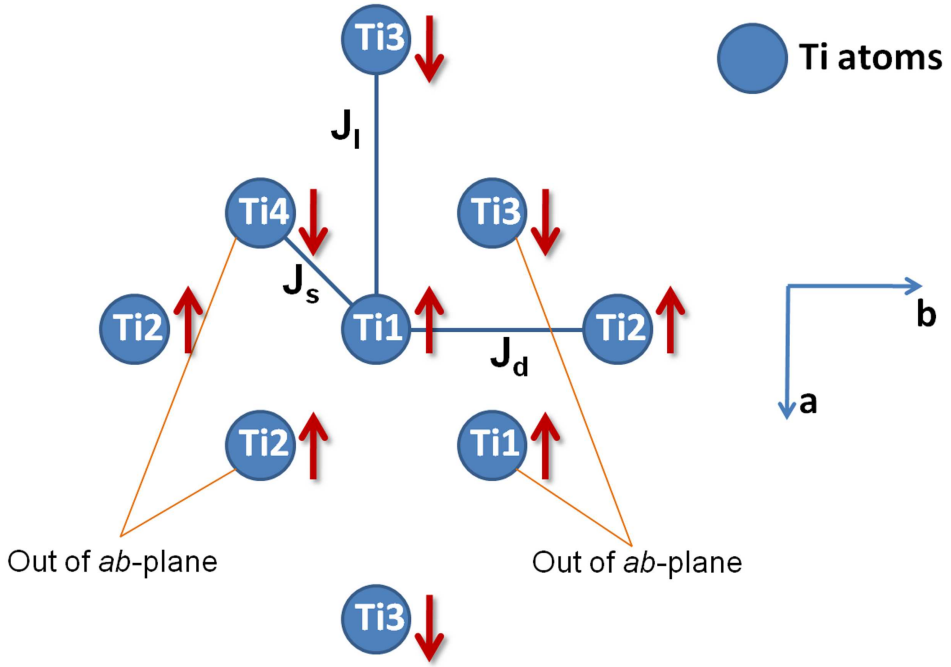

Figure 2.4:
Magnetic couplings in the orthorhombic structure between the closest Ti atoms. The environment of each Ti consists in two far Ti along the *a*-direction, two Ti along the *b*-direction and four closest Ti atoms which appear to be along the *ab*-direction, but really are out of the *ab*-plane. Couplings along the *c*-axis are regrlected because of their weak character. The three main magnetic couplings, as it can be seen, are J_s, J_d and J_l. Arrows indicate the magnetic configuration in the ground state of the compound.

TiOCl is structurally bidimensional, as we mention before, but its dimensionality has been reduced electronically as in the well-know cubic systems with reduced dimensional electronic properties, as $KCuF_3$ (1-D) and $LaMnO_3$ (2-D).[48]

2.4.2 Evolution of magnetic couplings (J)

We have also calculated the different magnetic couplings in the structure and their variations with pressure. To obtain the different exchange constants, we have calculated the total energies within the LDA+U scheme for various magnetic configurations and several pressures within the orthorhombic structure (P $<$ 9 GPa). Due to the structure of the material, we consider three different magnetic couplings: J_d, within the 1-D chains along the *b*-axis; J_s, the coupling beween a Ti and its four

Table 2.4:
Magnetic couplings (expressed in Kelvin) between Ti atoms at several pressures (units in GPa) in the orthorhombic structure. The last row shows the calculated T_c (in Kelvin) from a 1-D Heisenberg model at several pressures (units in GPa) in the orthorhombic structure.

P (GPa)	0	4	7	9
J_s (K)	-12	-10	0	10
J_d (K)	300	1100	1400	1650
J_l (K)	-1	-4	-4	-4
T_c (K)	50	180	230	275

closest neighbours; and J_l, the coupling along the a-axis. We have considered a structure with four inequivalent Ti atoms (labelled as Ti1, Ti2, Ti3 and Ti4). A scheme of the magnetic couplings in the structure can be seen in Figure 2.4.

We have fit our total energies to a Heisenberg-type Hamiltonian of the form

$$J = \sum_{i,j} J_{ij} S_i S_j \tag{2.1}$$

where the sum runs over spin pairs.

With such a Hamiltonian, J positive means AF coupling is favored and J negative means ferromagnetic coupling is favored. In this scenario, with four inequivalent Ti atoms, we can construct four possible magnetic configurations (Ti1, Ti2, Ti3, Ti4): $\uparrow\downarrow\uparrow\downarrow$; $\uparrow\uparrow\uparrow\uparrow$; $\uparrow\downarrow\downarrow\uparrow$; $\uparrow\uparrow\downarrow\downarrow$. The last one is the ground state acording to our calculations, in good agreement with experimental measurements. The magnetic configuration which corresponds to the ground state has been plot in Figure 2.4.

From those energies, we have obtained the magnetic coupling values for all the pressures studied in the orthorhombic structure: P = 0 GPa, P = 4 GPa, P = 7 GPa and P = 9 GPa. The results are summarized in Table 2.4.

We have observed that the coupling along the b-axis is much bigger than the others ($[J_b/J_a] \approx 300$ and $[J_b/J_s] \approx 25$ in the P = 0 case) due to the highly 1-D electronic structure of the material, and increases rapidly with pressure.

The calculated in-chain couplings are in good agreement with fittings to a spin-1/2 Heisenberg chain model of the experimental susceptibility curves.[49–51] This coupling will give rise to the low-temperature spin-Peierls phase. The increase with pressure of the magnetic exchange constant along the b-axis indicates a large increase

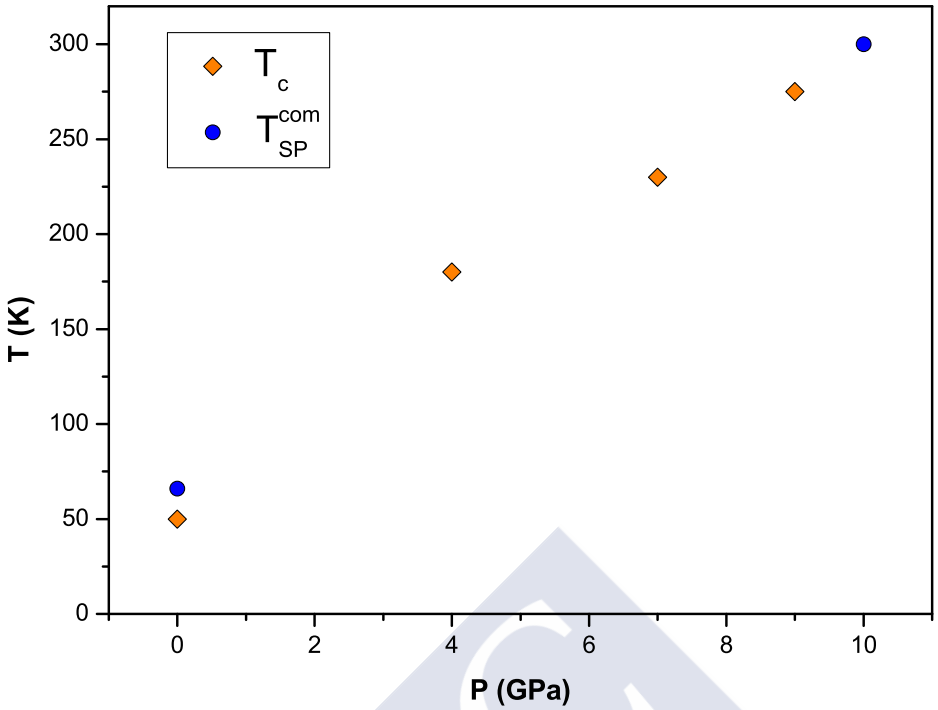

Figure 2.5:
Theoretical evolution of T_c with pressure and measured evolution of T_{SP}^{com} with pressure. Pressure values are in GPa and transition temperatures are in K.

with pressure of the associated transition temperatures to the spin-Peierls phase, and more important an increase of the one-dimensionality (at least magnetically) of the system with pressure.

Fitting the magnetic couplings to a 1-D Heisenberg model, we can estimate the transition temperature, using the standar mean-field expresion.

$$K_B T_c = \frac{1}{3} z J S^2 \tag{2.2}$$

In this equation, z is the number of nearest neighbours (z=2 in this case, the number of nearest neighbours along the b-direction, which is the magnetic coupling that changes whith pressure) and the factor 1/3 comes from the 1-D character of the magnetic structure.

This fit yields values of the transition temperatures close to those obtained experimentally.[49] The values we have calculated are summarized in Table 2.4.

Noting that the exchange coupling constants we calculate are one half of those due to the different choice of the Hamiltonian we have made. For P > 10 GPa, a transition is expected at room temperature, as has been found experimentally.[40] Our theoretically estimated transition temperature of about 275 K for P = 9 GPa also agrees with experiment. Hence, our calculations explain how the evolution with pressure of this magnetic coupling is associated to the transition temperature to a spin-Peierls phase. The appearance of a dimerized spin-Peierls phase at room temperature when pressure is increased above 10 GPa is a consequence of the large pressure dependence of the magnetic exchange coupling along the *b*-axis and the strong σ-type bond along that direction. In Figure 2.5 we can observe the trend of the transition temperature with pressure (note that the calculated T_c at low pressure is 50 K, and experimentally $T_{SP}^{com} = 70K$, and at high pressures measured T_{SP}^{com} is about room temperature, and calculated T_c is 275 K). Thus, our calculations help to understand the connections between the experimental evidences al low temperature and P = 0 GPa and also at room temperature and high pressures.

2.4.3 Electronic gap evolution

In a previous paper, Kuntscher *et al.*[38] observed a strong suppression of the transmitance and an abrupt increase of the near-infrared reflectance above $\approx$ 10 GPa in TiOCl, with an accompanying change of colour from transparet-brown at low pressure to black at high pressure (Figure 2.6).

These effects were interpreted as an indication of a pressure-induced metallization of the 1-D chain. This finding, if confirmed, could provide an exceptional opportunity to study the low-energy electronic excitations of a 1-D itinerant-electron system, as well as a type of Mott transition in reduced dimensions.

Later on, a structural phase transition was observed from high pressure X-ray diffraction experiments in isostructural TiOBr at 14 GPa, coincident with the proposed pressure-induced metallization.[52] This structural transition was suggested as the possible origin of the collapse of the charge gap at high pressures. However, the high-pressure phase was not previously resolved and the issue of whether the system is truly metallic was not clarified.

Recently, Forthaus *et al.*[39] measured the resistivity up to $\approx$ 25 GPa and reported a decrease of the electronic gap above $\approx$ 8 GPa in TiOCl, but ruled out any structural transition and the existence of a metallic phase at high-pressure. These

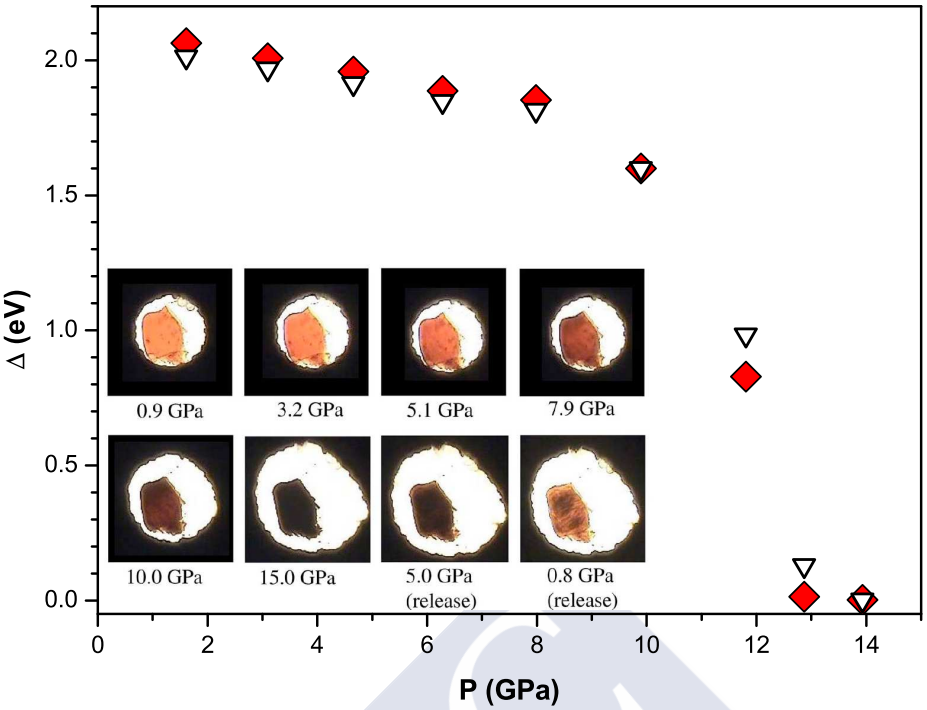

Figure 2.6:
Optical gap as function of pressure for E || a (solid symbols) and E || b (open simbols) obtained from optical measurementes by Kuntscher *et al.*[38] Apparently, the gap drops to zero at 13-14 GPa, which has interpreted as a signature of pressure-induced insulator-metal transition. The inset shows the change of colour of TiOCl under pressure, taken from ref. [38].

authors attributed the reduction of the gap to the high sensitivity of the hopping to the pressure-induced changes in the bond lengths and angles along the Ti-O-Ti path.

Above 10 GPa, TiOCl shows a monoclinic structure at room temperature. Ti-Ti dimers appear along the *b*-direction. This structural transition produces changes in the electronic structure with the formation of molecular orbitals within the dimer. This modifies strongly the excitation spectra, leading to a dramatic reduction of the electronic gap with respect to the undimerized orthorhombic phase. In Figure 2.7 the changes in the electronic gap that come out from our calculations can be seen. Within the orthorhombic structure, below 10 GPa, the gap decreases with pressure by about 30%, from 1.5 eV at 0 GPa to $\approx$ 1 eV at 9 GPa, in good agreement with the

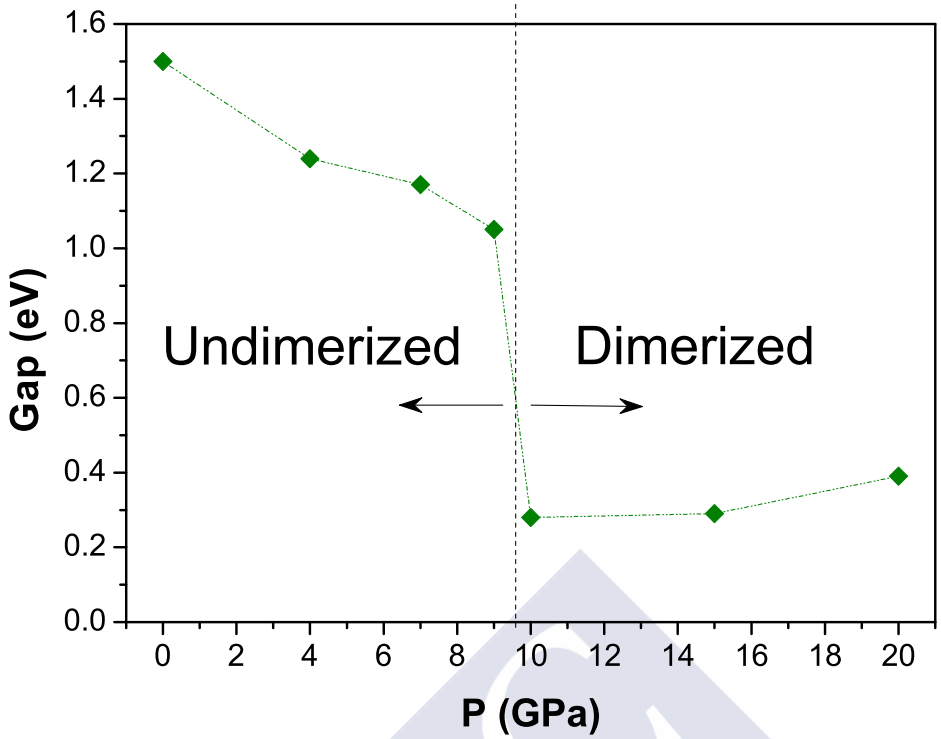

Figure 2.7:
Calculated evolution of the band gap with pressure. Dashed vertical line indicates the transition pressure from the orthorhombic structure to monoclinic structure. The lines are a guide to the eye.

reduction observed experimentally.[38, 39] The calculations were performed with a value of U of 5 eV, which reproduces nicely the experimental gap at low pressures. In the dimerized monoclinic structure, stable at room temperature beyond $\approx$ 10 GPa, the gap reduces drastically to $\approx$ 0.3 eV. This is again in very good agreement with the experimental observation of a sudden decrease of the charge gap at room temperature above $\approx$ 10 GPa.[38] Our calculations predict that more than 30 GPa would be necessary to obtain such a reduction of the electronic gap without considering a structural transition. Electronic gap, however, does not disappear with pressure. From these evidences, the insulator-metal transition is not the real scenario under pressure, as the lack of a Drude peak in optical conductivity suggests. Considering the structural transition, the observed electronic properties can be understood.

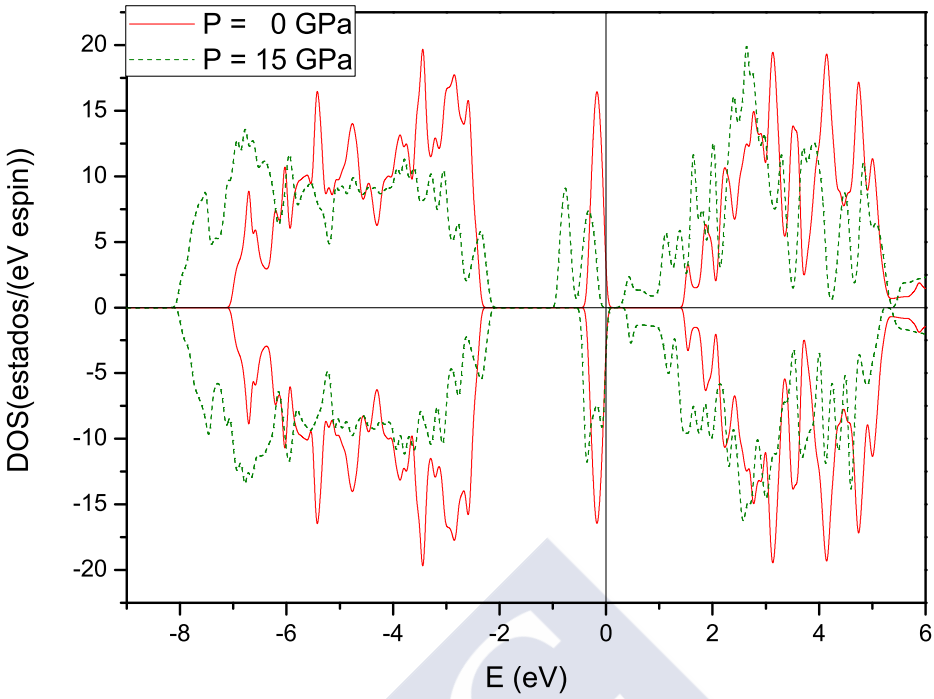

Figure 2.8:
Spin-up (positive values) and spin-down (negative values) total density of states (DOS) plots for the TiOCl in the ground state magnetic configuration at ambient pressure ($Pmmn$) and at P = 15 GPa ($P2_1/m$). The vertical line marks the Fermi energy.

The trend of the electronic gap can also be observed in the density of states plots of the low-pressure orthorhombic and high-pressure monoclinic structures of TiOCl (Figure 2.8). In the figure, it can be seen a drastic reduction of the electronic gap near the Fermi energy with increased pressure (from 1.5 eV in the orthorhombic low-pressure structure to 0.3 eV in the monoclinic high-pressure structure, P = 15 GPa). The band gap is a Mott-Hubbard-type gap, showing a direct gap between d-states (d-d gap). The states of d^1 electron of Ti are well localized in a $\approx$ 1 eV band near the Fermi energy, with pressure producing an increase of $\approx$ 20 % of the bandwith. The oxygen bands are in energies lower than -2 eV.

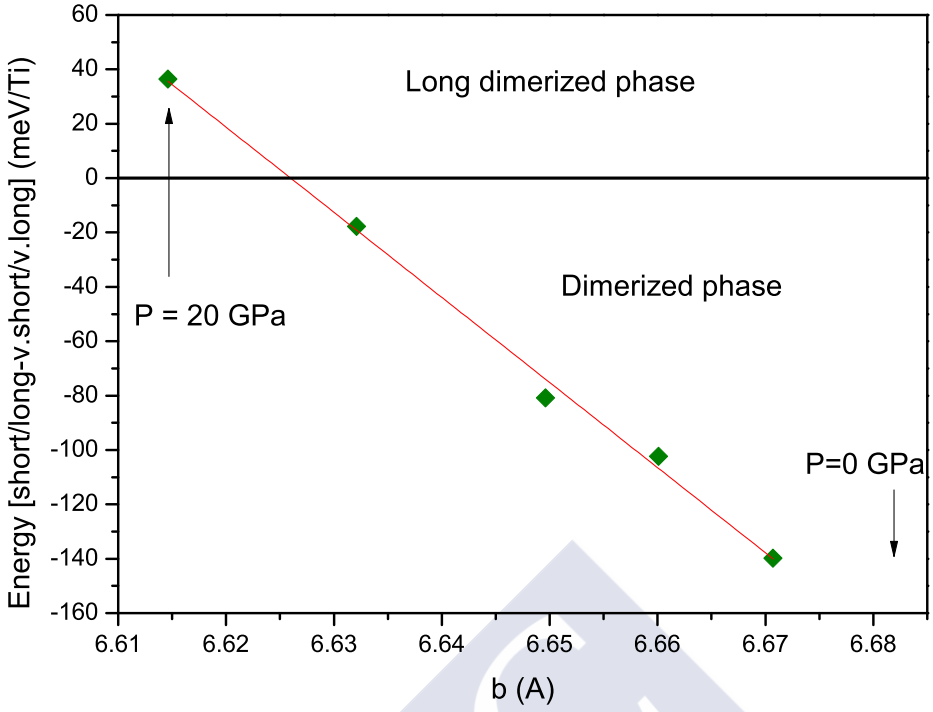

Figure 2.9:
Total energy difference between "short-" and "long"-dimerized structures at several values of b parameter (associated with different pressures). We can see the transition at about P = 15 GPa.

2.4.4 Structural transition: Spin-Peierls to Peierls

Two types of dimerized structures could be converged for this material in a monoclinic space group. This is an important consequence that follows also from the non-monotonic evolution of the degree of dimerization (difference of short-long distances) in the dimerized chain with pressure.

At P = 0, the Ti-Ti distances along the *b*-axis are 3.25 Å in the short bond and 3.43 Å in the long bond, a difference of about 3 %. At higher pressures (not stable at P = 0 GPa), a different type of dimerization can be analyzed which we have named "long-dimerized". In these structures, Ti-Ti distances along the *b*-axis is about 2.95 Å in the short bond and is about 3.69 Å in the long bond, a difference of about 11 % with respect to the undimerized values (values calculated at P = 15 GPa, where this structure becomes the most stable). Hence, at every pressure we

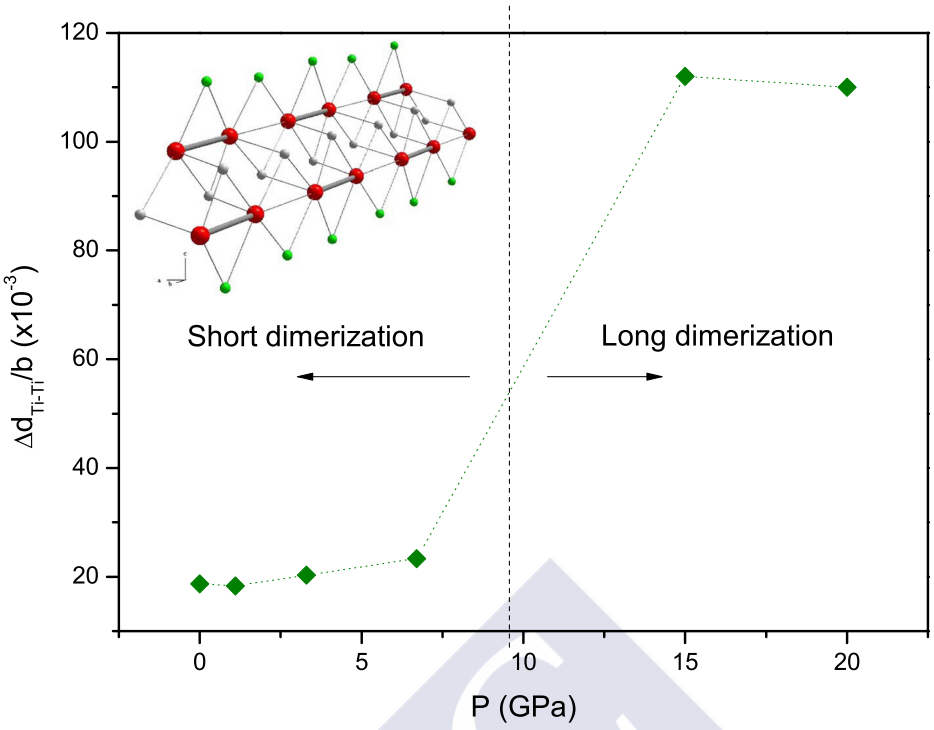

Figure 2.10:
Difference between short and long distances in the dimerized monoclinic phase with pressure. The inset shows the dimerized structure proposed at 15 GPa, highlighting the short Ti-Ti bonds along the *b*-axis. Red points represent Ti atoms, green chlorine and gray oxygen.

have compared the total energy of these two possible dimerized structures. Results are summarized in Figure 2.9.

Above P = 15 GPa, a transition occurs to a high-pressure "long-dimerized" phase. At a similar pressure, an anomaly is found in the resistivity measurements,[39] which can be explained by a strong reduction of the gap in such a structure.[40] In this pressure range, the short Ti-Ti distance approaches the Ti-Ti distance in Ti hcp metal.

In Figure 2.10 it can be seen that the difference in the distances between short and long bonds in the dimerized chain increases dramatically between 10 and 15 GPa. The discontinuity in the evolution of the bond distances in the dimerized phase at high pressures is at odds with expectations for a conventional spin-Peierls scenario. On the other hand, as the short Ti-Ti distance approaches the limit

for electron itinerancy, the spin-Peierls distortion of the 1-D chain increases the difference between the short and long bonds. So, it is most probably the proximity of the material to the itinerant electron limit at high pressure what drives the transition from the short- to long-dimerized structure.

Thus, on the basis of the obtained experimental results and *ab initio* calculations we can propose the following scenario: at ambient pressure TiOCl is a Mott insulator with large energy gap $E_g \approx 1.5$ eV caused by strong Coulomb (Hubbard) repulsion U. Low-energy states in this case are determined by the effective AF Heisenberg model with the exchange constant $J = 2t^2/U$. In the 1-D crystal structure of TiOCl, a SP transition with corresponding dimerizations sets in below certain temperature. With increasing pressure TiOCl apparently approaches an itinerant state and, at P $\approx$ 10 GPa, it would become a metal with U $<$ t. But the electron-lattice coupling in this case again causes instability of such 1-D metal and leads to the ordinary Peierls dimerization. Here, the corresponding critical temperature and dimerization are determined by the energy scale t of the electronic hopping (bandwidth), instead of J in the localized regime.

As a result the dimerized SP phase of TiOCl at P $<$ P_c exhibits, above P_c, a crossover to an insulating and dimerized Peierls phase with a smaller energy gap, but higher T_c and larger dimerization. Such a nontrivial crossover from the Mott insulator with the SP dimerization to an essentially band insulator due to the usual Peierls distortion seems to be a unique feature of TiOCl, or rather TiOCl is the first system in which this phenomenon is observed. There may be other examples of such interesting behaviour in other quasi-one-dimensional inorganic and organic solids. So, our results support an enhanced shortening of the bond in order to form a molecular orbital, i.e. by a purely electronic mechanism. In this case the magnetic structure will play a secondary role, and hence the high-pressure phase departs from the spin-Peierls scenario, and may be rather interpreted as a usual Peierls dimerization, proceeding from the itinerant limit.

2.5 Summary

We have demonstrated the existence of a structural transition at high pressure in TiOCl, at which the Ti^{3+}-Ti^{3+} dimerization is strongly enhanced as compared to that at ambient pressure. We have characterized the structural and physical properties of the high-pressure phase, where Ti^{3+}-Ti^{3+} dimerization is stronger (i.e.,

there is a much larger difference between the large and short Ti-Ti distance) than in the ambient pressure phase. We have analyzed the quasi-one-dimensional electronic structure of TiOCl and also the strong one dimensionality of the magnetic properties. Ti^{3+} (d^1) ions have one t_{2g} orbital occupied (d_{yz}) with a large hopping integral along the *b*-direction of the crystal. Our calculations predict the transition to a high-pressure dimerized phase at room temperature at about 10 GPa, in accordance with the experiment. At around 15 GPa, a dramatic reconstruction of the electronic crystal structure is driven by the proximity ot the itinerant electron boundary in the short Ti-Ti bonds, suggesting a completely different mechanism for the high-pressure dimerization, which should be treated not as a spin-Peierls, but rather as a Peierls transition.

USC
UNIVERSIDADE
DE SANTIAGO
DE COMPOSTELA

3

Analysis of the pressure effects in non-dimerized and dimerized spinels: cases of MgV_2O_4 and ZnV_2O_4

3.1 Introduction

In the first chapter of the Thesis we have observed that TiOCl is a compound that aproaches a metal-insulator transition by applying pressure. In this chapter we study another type of compounds which are near a metal-insulator transition by increasing mechanical pressure and also by chemical pressure. As in the case of TiOCl the onedimensionallity of its electronic structure leads to an unexpected Peierls transition. In this chapter we study what similar electronic nature phenomena take place in a 3-D structure as spinels.

Transition metal oxides often present an interplay between various degrees of freedom (orbital, spin and charge) resulting in the formation of different superstructures.[53] Among these, oxide spinels with chemical formula AB_2O_4, that present a frustrated pyrochlore lattice for the B cations (transition metal), are particularly interesting because they allow to study the importance of direct cation-cation interactions in a series with single valent B-B interactions. Moreover, being the A-site non-magnetic simplifies the interpretation of the magnetic structure of the compounds in terms of only those direct B-B interactions.

The series of oxide spinels AV_2O_4 (A = Cd, Mn, Zn or Mg), that presents a frustrated pyrochlore lattice for V cations, approaches an insulator-metal (Mott)

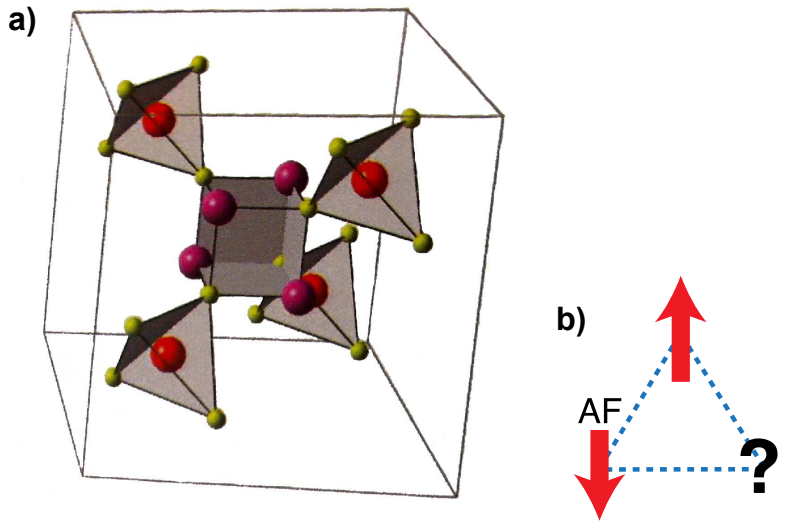

Figure 3.1:
a) Crystallographic structure of the spinel lattice. Red balls denote A^{2+} tetrahedral position, violet for octahedral B^{3+} and yellow corresponds to the O^{2-} positions. b) Antiferromagnetically interacting spins in a triangular arrangement.

transition when the V-V distance is reduced sufficiently, by applying pressure or by changing the size of the A^{2+} cation.[41, 54] ZnV_2O_4 is the closest member of the series to the metallic state, considering those with a non-magnetic A^{2+} cation. Recently, the transition has been confirmed in CoV_2O_4.[55]

The materials crystallize in the spinel structure (AB_2O_4) that presents two types of sites, A and B, with tetrahedral and octahedral coordination with surrounding oxygens, respectively. Oxygen atoms in spinels have a cubic close-packed arrangement. A scheme of a spinel structure can be observed in Figure 3.1 a)[1]. The great versatility of this structure allows to accommodate many different ions, both in the A and B site, being possible to find spinels with magnetic ions at the A and B position (MnV_2O_4, $CoCr_2O_4$...), only at the B position (ZnV_2O_4, $CdCr_2O_4$...), only at the A position ($FeAl_2O_4$, $FeSc_2O_4$...), or none at all ($ZnAl_2O_4$).

The ground state of the AV_2O_4 spinel compounds has produced an intense theoretical research in the last years,[42, 56–59] specially related to the magnetic frustration in the pyrochlore lattice.

[1]Figure 3.1 a) has been taken from the Doctoral Thesis of S. Blanco-Canosa

Geometrical frustration is an important feature in magnetism, where it stems from the geometrical arrangement of spins. A simple 2D example of the concept of frustration in a triangular lattice is shown in Figure 3.1 b). Three magnetic ions reside on the corners of a triangle with antiferromagnetic interactions between them (the energy is minimized when each spin is aligned opposite to its neighbours). Once the first two spins align anti-parallel, the third one is frustrated because its two possible orientations, up and down, give the same energy. The third spin cannot simultaneously satisfy its interactions with both of the other two. Thus the ground state is twofold degenerate in a triangular lattice, the total degeneracy is 2^N, with N the number of sites, which is enormous in real materials. This huge degeneracy leads to interesting physics like the proposed spin liquids, that would be a unique state of matter with no long-range magnetic ordering even an zero temperature, but have not been found experimentally so far. This effect also occurs to some degree in the case of pyrochlore lattice ZnV_2O_4. Very recently, the frustrated pyrochlore lattice has drawn even more attention with the finding of magnetic monopoles as a result of the frustrated nature of the lattice.[60, 61]

The tetragonal distortion at $T_S = 51$ K makes the t_{2g} levels split into a lower d_{xy} level and two-fold degenerate d_{xz} and d_{yz} levels. It is clear that the first electron of V^{3+}:d^2 occupies entirely the d_{xy} level, whereas the second one is located in a combination of the other t_{2g}-orbitals d_{xz} and d_{yz}.[53] The d_{xy} electron, according to Goodenough-Kanamori-Anderson (GKA) rules, leeds to a relatively strong in-plane AF coupling. The question that remains open concerns the occupations on the d_{xz}/d_{yz} doublet and what magnetic ordering results from that.

Three main models try to solve these d_{xz} and d_{yz} occupations: the real orbital ordered model, where the ground state consists of alternating occupation of the d_{yz} or d_{xz} orbital in successive layers along the c-axis;[56] the complex orbital order model where the second electron occupies the complex orbital $(d_{yz} \pm i d_{xz})$ which has an unquenched value of the orbital angular momentum;[57] and a third model that takes into account the proximity of ZnV_2O_4 to the itinerant-electron boundary,[42] showing a dimerization along the V-V chains, which is described by the formation of homopolar molecular V-V bonds, characterized by a partial electronic delocalization (the orbital wave functions in this case would be a real combination of orbitals $(d_{yz} \pm d_{xz})$ with no net orbital moment). This model explains easily the observed off-plane $\uparrow\uparrow\downarrow\downarrow$ magnetic order and also the appearance of electronic polarization in these spinels,[62] through a structural distoriton (dimerization of the V-V chains).

In this chapter we make an analysis of the effects of applied pressure in the dimerized structure of ZnV_2O_4 and will analyze the importance of the structural distortion in preventing the occurrence of a pressure-induced metallization.

3.2 Computational Details

General characteristics of the calculations were described in section 1.2.7. In this chapter, the exchange-correlation potential utilized was the Perdew, Burke and Ernzerhof (PBE) version of the general gradient approximation (GGA).[13] The geometry optimization was carried out minimizing the forces in the atoms and the total energy of the system to all the pressures calculated in this work. We converged with respect to the k-mesh and to $R_{mt}K_{max}$. We have used a $6 \times 6 \times 4$ sampling of the full Brillouin zone for electronic structure calculations and geometry optimization. $R_{mt}K_{max} = 7.0$ is chosen for all the calculations. Muffin-tin radii chosen were the following: 1.89 a.u. for Zn, 1.96 a.u. for V and 1.68 a.u. for O.

For modelling the behaviour of d electrons, we included strong correlation effects by means of the LDA+U scheme.[28] A value of $U_{eff} = 3.0$ eV was used in the calculations. This value has been chosen because it reproduces the gap obtained experimentally by Pardo et al.[42]

For the calculations of transport properties we utilized the BoltzTraP code,[30] that uses the energy bands obtained from the WIEN2k software and performs a semiclassical calculation to solve Boltzmann equation. We used a $42 \times 42 \times 30$ sampling of the full Brillouin zone, where convergence was achieved. The calculation of transport properties requires a fine mesh to carry out the integrations in the Brillouin zone.

3.3 Non-dimerized spinels: MgV_2O_4

We have mentioned earlier that the series AV_2O_4 (with A being Cd, Mn, Zn, Mg) approaches a metal-insulator transition when the V-V distance is reduced sufficiently. This can be observed with the measurements of the Seebeck coefficient made by Blanco-Canosa *et al*. presented in Figure 3.2. A reduction in the absolute value of the thermoelectric power is evident in Zn and Mg samples, with respect to Mn and Cd samples. Moreover, typical activated behaviour is no longer present in Zn and Mg, and thermopower tends to a constant value at low temperature. This result

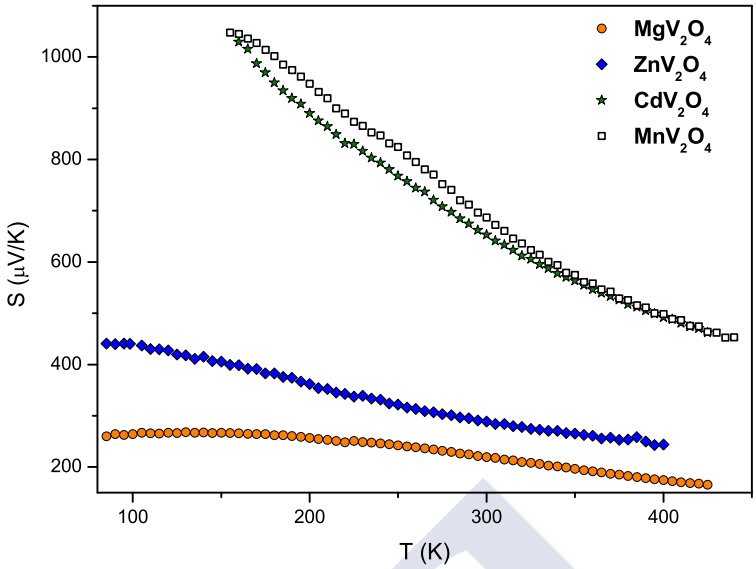

Figure 3.2:
Temperature dependence of the thermoelectric power for the series AV_2O_4 (A = Mg, Zn, Cd and Mn) taken from [54].

is fully consistent with a scenario in which progressive electronic delocalization in cation-cation bonds occurs as the metal-metal distance is reduced across the series. These conclusions about partial electronic delocalization are also supported by the strong reduction in the magnetic moment observed from CdV_2O_4 to ZnV_2O_4, in spite of having in every case V^{3+}: d^2 cations with nominally the same S=1 state in both compounds.[63]

The V-V distance, determined from a Rietveld refinement of the X-ray patterns, reduces along the series from 3.07 Å in the Cd compound to 2.97 Å for MgV_2O_4. Changing the A-site from Cd to Mg acts like chemical pressure. On the basis of experimental considerations, the critical distance for the metal-insulator transition was estimated by Goodenought to be at about 2.94 Å for compounds including V^{3+} cations.[64] Below that V-V distance, compounds should cross to the itinerant limit. One way to study this transition could be to apply pressure to the Mg compound

Table 3.1:
Experimental atomic positions of the MgV_2O_4 spinel for space group $Fd\bar{3}m$ (no. 227)

Atom	Crystallographic position	Atomic positions
V	16c	(0.125, 0.125, 0.125)
Mg	8b	(0.500, 0.500, 0.500)
O	32e	(0.260, 0.260, 0.260)

since it is closest to the critical distance. An experimentally accessible pressure is expected to produce the transition.

We have studied the cubic phase of MgV_2O_4, with lattice parameter $a = 8.4378$ Å measured at room temperature. The atomic positions are presented in Table 3.1, for space group $Fd\bar{3}m$. We performed total energy calculations to optimize the volume of the material using the GGA-PBE.[13] The ground state volume obtained is in agreement with the experimental one (0.3% smaller, within the typical GGA accuracy). The value of the bulk modulus of 196 GPa is also consistent with previous results on oxide spinels.[65]

It is well known that the trigonal distortion of the oxygen octahedron surrounding the V^{3+} cations varies with the V-V distance, and this changes slightly the oxygen positions. For our studies under pressure, we made the approximation of keeping fixed the oxygen coordinates and only varying the cell parameters.

From our total energy vs. volume calculations, the predicted critical V-V distance (2.94 Å) is reached at about 5 GPa. For the equation of state around the minimum, we used fittings to a Murnaghan[66] and a Birch-Murnaghan equation,[67] leading both to the same quantitative results for equilibrium volumes and bulk moduli. According to our calculations, the transition occurs very close to that distance, at some 6.5 GPa (V-V distance of 2.937 Å , in close agreement with the prediction by Goodenough[64]).

In Figure 3.3, the transition from a narrow-band insulator to a metal can be observed. For the experimental structure measured (Figure 3.3 a)), the material is an insulator with a band gap of approximately 0.2 eV. The value of U was chosen to fit the experimental value of the band gap[64] (it turns out to be about 3.1 eV within the so-called self-interaction corrected LDA+U method). The material shows the typical electronic structure of a Mott-Hubbard insulator with a $d - d$ gap. Figure 3.3 a) shows the partial DOS for O and V (including multiplicities) inside the unit

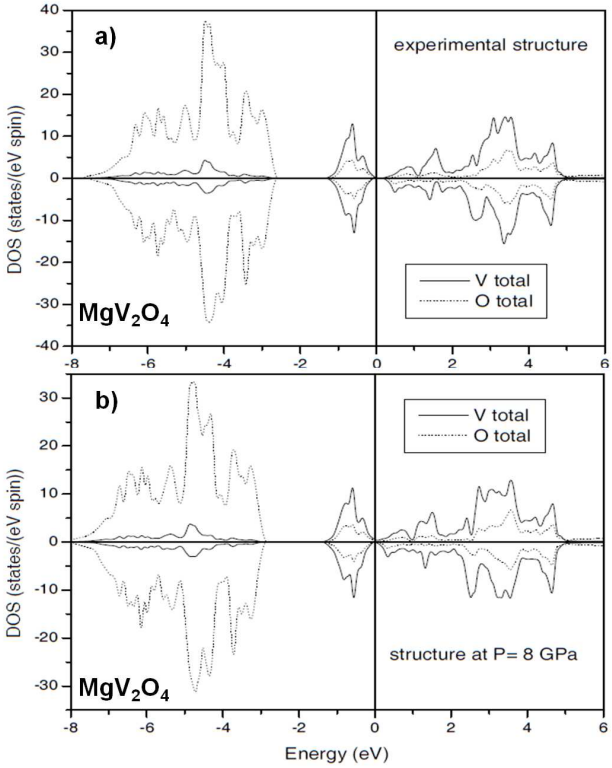

Figure 3.3:
DOS plots for all the V and O levels in the unit cell for the low pressure a) and high pressure (P = 8 GPa) b) in the MgV_2O_4 structure. Upper panel a) shows the $d-d$ character of the narrow gap of only 0.2 eV according to the literature. In the lower panel b) we observe that metallicity occurs by overlapping of the d bands that come together due to the small V-V distance. Positive (negative) values represent the spin-up (down) channel. Fermi level is at zero.

cell. Both the conduction and the valence band have a strong d character, being the O p contribution to those bands smaller, but non-negligible. Figure 3.3 b) shows the density of states for the structure under an applied pressure of approximately 8 GPa. The reduced V-V distance leads to a stronger $d-d$ interaction. At a high enough pressure, the valence and conduction bands eventually overlap yielding a metallic behaviour.

Thus, using the tetragonal structure obtained experimentally and applying pressure, a transition to a metallic state is predicted at about 6.5 GPa, when the V-V

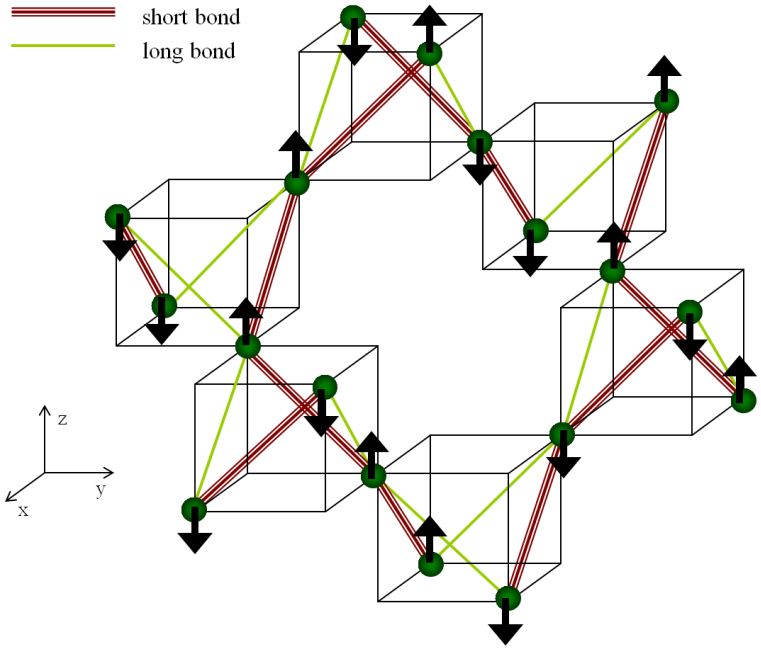

Figure 3.4:
Schematic representation of the "dimerized" structure resulting from *ab initio*, all-electron calculations for realistic values of U in ZnV_2O_4. Bold (thin) line represents short (long) in-chain bonds. The magnetic state is indicated by arrows.

distance is close to the critical distance for a localized-to-itinerant crossover in V^{3+} compounds with direct metal-metal bond.

3.4 Dimerized spinels: ZnV_2O_4

ZnV_2O_4, as we have explained above, crystallizes in a cubic spinel structure, where the V atoms form a pyrochlore lattice of corner-sharing tetrahedra. Because of the geometry of the pyrochlore lattice, the AF interactions between the V atoms are highly frustrated. The lattice formed by the V atoms can be described as built up by V-V chains running along the [110], [011] and [101] directions. The magnetic structure, found by neutron diffraction measurements,[68, 69] is AF along the [110] direction (within the *ab* plane), but along the [101] and [011] (off-plane) directions the V moments order ↑↑↓↓↑↑.

Table 3.2:
Crystallographic positions of the dimerized structures in the space group $P4_12_12$ (no. 92) in the low pressure phase of ZnV_2O_4 spinel.

Atom	Crystallographic position	Coordinates
Zn	4a	(0.2543, 0.2543, 0.0000)
V	8b	(0.4945, 0.7583, 0.8766)
O1	8b	(0.7412, 0.5159, 0.8833)
O2	8b	(0.7485, 0.5201, 0.3866)

The spinel ZnV_2O_4 is an excellent candidate for studying the possibility of the crossover between localized and itinerant electrons, close to the insulator-metal (Mott) transition. This crossover can occur via partial electron delocalization, but not in the whole system right away. It takes place first in certain clusters, e.g., in dimers.[41] This is because ZnV_2O_4 is a magnetic insulator close to the itinerant electron limit.

Ab initio calculations with structural optimization could be very useful to study possible lattice instabilities. For small values of the electron-electron (Hubbard's) repulsion U, the most stable structure always consists of V-V dimers along the [011] and [101] directions, with ferromagnetic bonds becoming shorter that helps to understand the intriguing magnetic structure of this material (note that similar distortions may exist also for strongly localized electrons on a spinel lattice, but with antiferromagnetic bonds being shorter[70]). The dimerization obtained is a dramatic example of a strong electron-lattice coupling due to the partial electronic delocalization in the proximity of the itinerant-electron limit.

Structural optimization[42] based on GGA concludes that, for small values of U, the minimum-energy structure of the material forms dimers along the off-plane V chains, the short V-V distance being 2.92 Å (lower than the estimated critical distance for metal-insulator transition) and the long one 3.01 Å (see Figure 3.4) in the low-pressure phase. The structure so obtained can be indexed within the space group $P4_12_12$ (no. 92) leading to the structural parameters that are summarized in Table 3.2

This space group allows us to form an alternation of short/long bonds along the V chains (as mentioned before, [101] and [011]). If we make a structural relaxation using the LDA+U scheme (i.e. including strong-correlation effects in the

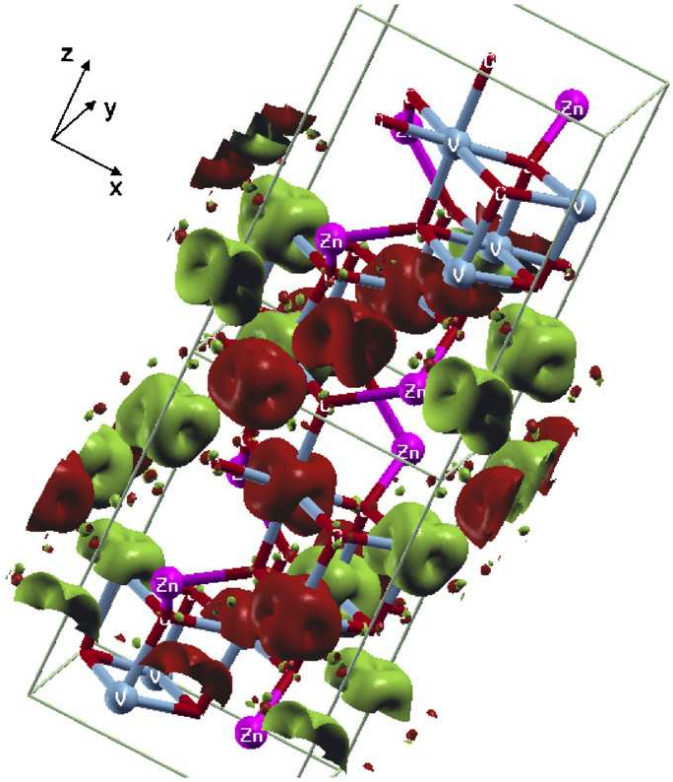

Figure 3.5:
Spin density of the dimerized structure (isosurface at 0.1 e/$\AA^3$) of ZnV_2O_4 at low pressure including spin-orbit effects made using XCrysDen software.[47] Red (green) colours represent spin up (down). Observe the in-plane AF coupling and out-of-plane up-up-down-down sequence. Also notice the lack of any orbital ordering.

structure optimization), we observe the same interatomic distances within less than 0.1%, showing the validity of the structural relaxation carried out within the GGA approximation. Forces were converged to less than 2 mRy/a.u. for a value of U_{eff} = 2 eV. The lattice parameters utilized were not relaxed, they were taken from experiment,[68] and only the internal positions were optimized. This is fully justified because the experimental lattice parameters can be obtained with better precision than a computational optimization of the structure. However, small distortions of the internal coordinates, as the one presented here, can be difficult to detect experimentally, especially for polycrystalline samples.[59, 62]

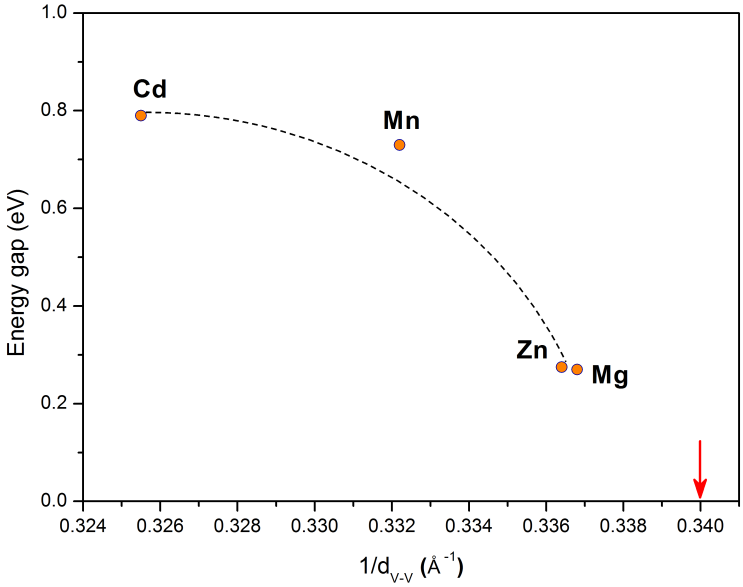

Figure 3.6:
Variation of the gap along the AV_2O_4 series (with A: Cd, Mn, Zn, Mg) as a function of the V-V distance. The red arrow marks the critical V-V distance for metal-insulator transition. The line is just a guide for the eye.

We have analyzed the electronic structure in this dimerized structure, considering also spin-orbit effects, at low pressure. The main results are summarized in Figure 3.5, presenting a picture of the three-dimensional spin density calculated in the dimerized structure, including the experimentally found magnetic structure: AF within the xy-plane, and $\uparrow\uparrow\downarrow\downarrow\uparrow\uparrow$ along the [011] and [101] chains. As we can also see in Figure 3.5, the orbital occupation of the V^{3+}:d^2 consists of a lower-lying d_{xy} orbital (fully occupied) and a higher-lying singly-occupied doublet, with equally populated d_{xz} and d_{yz} levels. Thus, in this state, close to the itinerant-electron limit (for small values of U where this structure is stable), there is no orbital ordering, in contrast to other pictures proposed in Refs. [57, 71, 72].

Calculations for the standard tetragonal structure,[68] the one that is stable for large values of U_{eff},[42] show that an orbitally ordered solution with an alternation of $d_{xz} \pm i d_{yz}$ orbitals (orbital angular momentum is antiparallel to spin at each site)

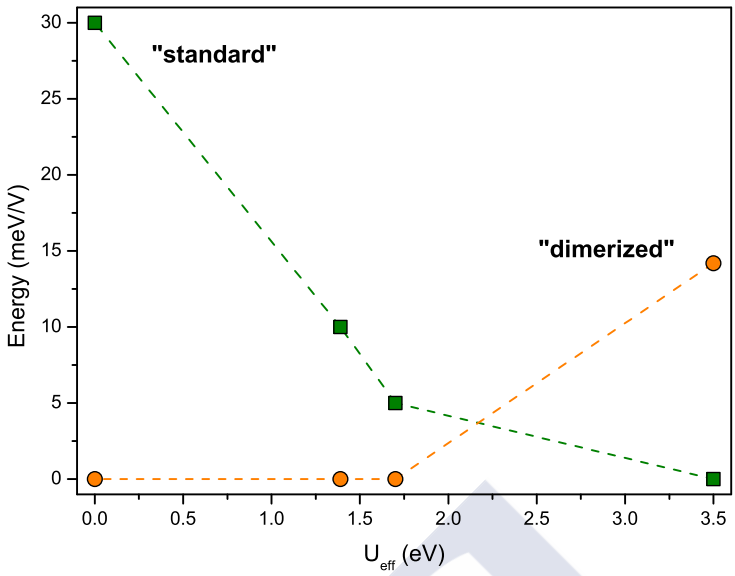

Figure 3.7:
Total energies (in meV/Vanadium ion) of the two structures as a function of U_{eff}. For small values of U_{eff} the "dimerized" structure proposed is more stable. Note that, for any U_{eff} ($U_{eff} < 2.2$ eV), we take as zero the energy of the most stable structure.

would be the ground state. However, this orbital ordering does not easily explain the magnetic structure observed experimentally.[73]

The proximity to the itinerant electron limit can be readily seen in Figure 3.6. This figure shows the variation of the energy gap obtained from resistivity measurements in polycrystalline samples of different V spinel compounds. As the series approaches the itinerant electron limit, the energy gap gets drastically reduced. Both experimental[41] and theoretical[42] results are consistent with ZnV_2O_4 being close to the itinerant regime. It has been found that even though MgV_2O_4 and ZnV_2O_4 are still semiconducting, some delocalization starts to take place in the form of molecular orbitals in an ionic matrix. It is in this regime of small U/W (W is the average bandwidth of the t_{2g} occupied levels that form the valence band) that a dimerized structure is stable. Our calculations show that W is about 2 eV for ZnV_2O_4 (estimated from non-magnetic calculations) and for $U \leq 2$ eV the dimerized solution indeed corresponds to the minimum energy. We have compared the

Table 3.3:
Different magnetic couplings in the two structures considered calculated *ab initio* from total energy differences. The coupling within the xy-plane is AF, J_{in} and the off-plane coupling (J_{out}) can be subdivided, in the case of the "dimerized" structure, in a FM coupling for the short bonds, J_s, and an AF coupling for the long bonds, J_l. All the energies are given in meV.

	Standard	Dimerized
J_{in}	-16	-16
J_{out} (J_s/J_l)	-12	10/-3

total energy of the two structures, the best "standard" (non-distorted) one and the one with dimerization, for different values of U_{eff} (see Figure 3.7). For small values of U_{eff} (below about 2.2 eV) the "dimerized" structure is more stable than the "standard" one.[2]

The obtained dimerized structure naturally explains the intriguing magnetic structure of ZnV_2O_4. The magnetic coupling within the xy plane is strongly AF due to the large direct hopping between σ-bonding d_{xy} orbitals. Along the [011] and [101] off-plane chains, we have now a strong FM coupling in the short V-V bonds due to the gain in kinetic energy caused by the strong reduction of the U/W ratio close to the itinerant electron limit.[74] Considering these two as the strongest magnetic interactions in the system, one can easily understand the magnetic structure. The long V-V off-plane bonds are forced to be AF by these bigger magnetic couplings. As we can see in Table 3.3, in the "dimerized" structure this is precisely the case: J_s (the exchange constant for the short V-V bonds) is FM, with a value of 10 meV, but J_l in the long bonds is AF and much smaller (its value is -3 meV). This readily explains the $\uparrow\uparrow\downarrow\downarrow\uparrow\uparrow$ magnetic structure in off-plane directions.

It is to be noted that this structural distortion that shows strong coupling between spin, orbital and lattice degrees of freedom in this material close to the itinerant electron limit, occurs without orbital ordering being involved. Our calculations show that the ground state is not orbitally ordered in this regime. This is purely an effect of the delocalization caused by the proximity to a transition towards itineracy, which leads to a lattice instability and to a structural deformation. This is so small that neutron data on single crystals misses it and an average of the

[2] Values of data in the Figure 3.7 have been taken from [42].

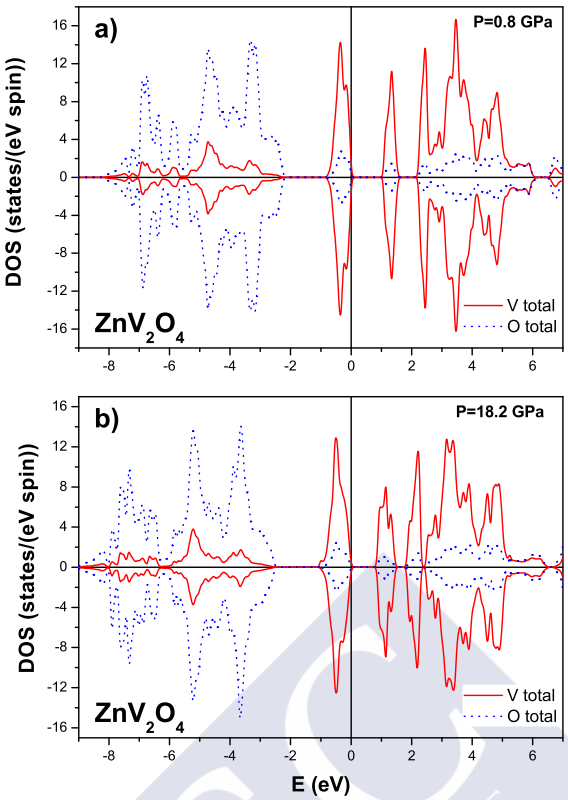

Figure 3.8:
DOS plots for all the V and O levels in the unit cell for the dimerized structure at a) $P = 0.8$ GPa and b) $P = 18.2$ GPa. The d-d character of the narrow gap of 1.0 eV can be noticed in the low pressure density of states a). A reduction of the gap to 0.8 eV can be noticed in the high pressure DOS b), leading to a non-metallized state. Upper (lower) panels show the spin-up (down) channel. Fermi energy is at zero.

V-V off-plane distances is obtained.[59] It has been argued theoretically[74] that LDA+U would overestimate the distortion, which indeed exists, but could be an order of magnitude smaller.

Let us analyze in detail the evolution with pressure of the electronic structure of dimerized ZnV_2O_4.[75] We have seen that the proximity to the transition causes lattice instabilities that lead to bond-length fluctuations that stabilize the formation of V-V molecular orbitals.

We have also seen that in the series AV_2O_4[41, 42] the reduced V-V distance (from 3.07 Å for Cd^{2+} ion to 2.97 Å for Mg^{2+} ion) can drive these systems close to

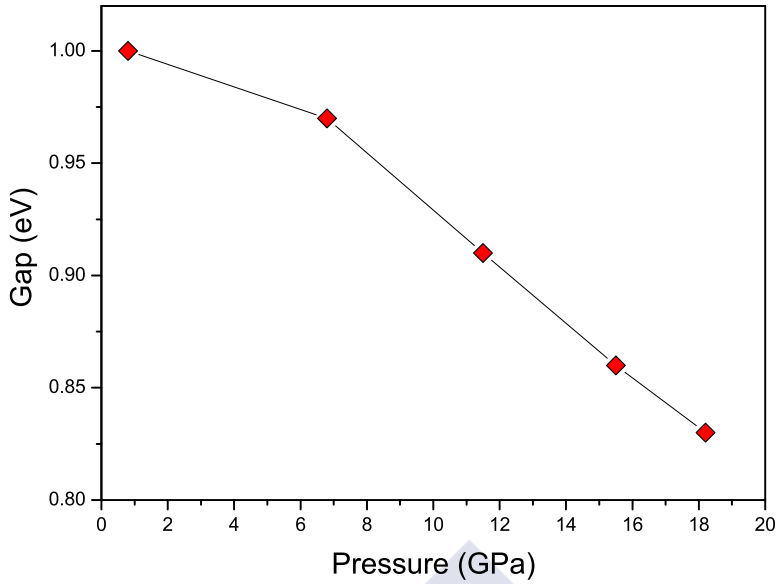

Figure 3.9:
Gap evolution with pressure in the dimerized state of ZnV_2O_4 calculated *ab initio*. The line is just a guide for the eye.

an insulator-metal transition. The critical distance for itineracy was estimated at about 2.94 Å,[64] attainable with a reasonably small pressure for the compounds with a smaller cation, like Mg^{2+} or Zn^{2+}, as we saw before.

Just like the non-dimerized structure of MgV_2O_4,[54] where applying pressure produces the transition (above P=6.5 GPa in the non-dimerized structure of MgV_2O_4), ZnV_2O_4 should present a similar behaviour, due to the almost identical size between Mg^{2+} and Zn^{2+} cations (leading to a very similar V-V distance). Let us see in detail what happens when pressure is applied to this dimerized structure.

In Figure 3.8, we present the DOS plots of the dimerized structure of ZnV_2O_4 at low (P=0.8 GPa) and high (P=18.2 GPa) applied pressure.[76] The value of the gap at low pressure was obtained experimentally from resistivity measurements by Pardo *et al*,[42] giving a value of ≈1.1 eV. At P=0.8 GPa (Figure 3.8 a)) with U=3 eV the material is an insulator with a band gap of approximately 1.0 eV, reproducing very nicely the experimental gap.[42] The electronic structure of a Mott-Hubbard insulator with a $d-d$ gap can be observed in the plot, where the V d

character contribution near the highest lying occupied states and lower unocuppied states dominates (O p levels have less contribution in these energy ranges, but it is non-negligible). Figure 3.8 b) still shows an insulating character of ZnV_2O_4 at P=18.2 GPa in the dimerized state. The V-V distance is reduced to 2.84 Å in the short V-V bond and 2.95 Å in the long V-V bond (the shorter one would be well below the critical value for itineracy). While the non-dimerized structure of MgV_2O_4 becomes metallic when pressure is applied, the dimerized state in ZnV_2O_4 does not allow metallization to occur. In this geometry, the system remains a Mott-Hubbard insulator. If we analyze the evolution of the gap in the dimerized structure at various pressures (Figure 3.9) we observe a slow reduction of the gap, that would only predict a metallized state at very high pressures (above 100 GPa). The dimerized structure of ZnV_2O_4 prevents the metal-insulator transition to occur, as it would happen in the non-dimerized structure. A pressure-induced metallic phase is not obtained for ZnV_2O_4. The reason for this behaviour is the additional Peierls-like gap produced by the dimerization of the V-V chains along the [011] and [101] directions of the spinel structure. The dimerized structure "protects" the system against crossing to the itinerant electron limit. Recent Quantum Monte-Carlo (QMC) calculations and additional experiments[77] confirm this hypothesis of the two gaps competing and evolving differently with pressure (the band gap being reduced with pressure and the Peierls gap becoming more robust). A non-monotonic pressure dependence has been actually observed, but the physics is the one we can describe *ab initio*, the actual details can be obtained only via more computationally demanding techniques, that deal with strong correlation effects in a more accurate way.

In the dimerized structure at 18 GPa, we have also found the same magnetic structure than the low-pressure one, and equal orbital occupation of the V^{3+}:d^2, with a lower lying d_{xy} orbital (fully occupied) and a higher lying singly occupied doublet (d_{xz} and d_{yz} levels) which alternates from one ion to its nearest V ion, as can be seen in Figure 3.10. As long as the dimerized structure is stable, this is the expected behaviour.

Further experimental evidences have been found very recently in favour of the dimerized structure,[62] with the observation of electrical polarization coexisting with the magnetically ordered phase, consistent with the appearance of dimerized chains in ZnV_2O_4. The polarization is smaller than the one predicted, which could

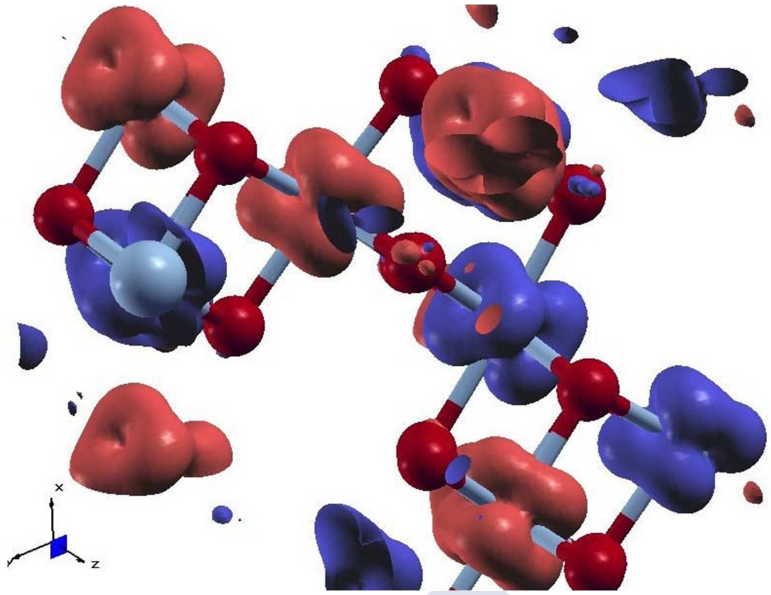

Figure 3.10:
Spin density of the dimerized structure of ZnV_2O_4 at high pressure.[47] Red (blue) colours represent spin up (down). We observed the ↑↑↓↓↑↑ spin configuration along the [011] and [101] directions. Orbital occupation of V^{3+} remains unchanged from the low pressure structure. Small red spheres represent O atoms. Zn atoms are not plotted for simplicity. This spin density plot corresponds to an isosurface at 0.1 e/Å^3.

be a sign of the DFT overestimation of the Peierls-like distortion, but at the same time a confirmation of the main physics our calculations predict to occur.

To further test the validity of our proposed structure, we have also calculated the thermoelectric power evolution with temperature and have compared it with experimental data. Taking the conductivity (σ) and Seebeck coefficient (S) calculated from spin-up and spin-down channels, the total thermopower is obtained according to the two-current model[78] expression:

$$S = \frac{\sigma'(\uparrow)S(\uparrow) + \sigma'(\downarrow)S(\downarrow)}{\sigma'(\uparrow) + \sigma'(\downarrow)} \tag{3.1}$$

where $\sigma'=\sigma/\tau$, in the constant relaxation time approximation.

We used the BoltzTraP code[30] to calculate the Seebeck coefficient, solving Boltzmann equation using a semiclassical approach. We used a 42 × 42 × 30 sampling of the full Brillouin zone, where convergence was achieved (calculation

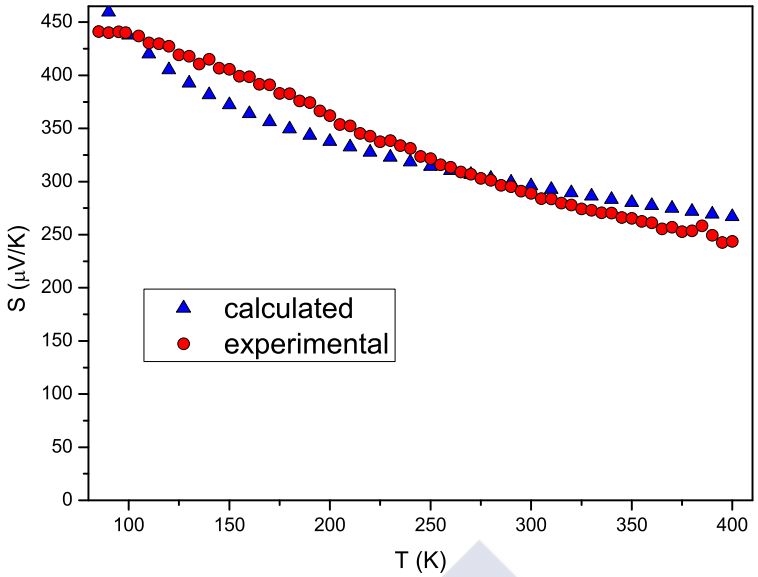

Figure 3.11:
Experimental and calculated temperature dependence of the thermopower. Observe that calculated values fit well with experimental measurements.

of transport properties requires a fine mesh to carry out the integrations in the Brillouin zone).

We present both the calculated data and the experimental values of the Seebeck coefficient (taken from Ref. [41]) in Figure 3.11. The calculated values are in good agreement with the experimental ones. The approximately linear Seebeck coefficient (compared with the values of thermopower of other compounds of the AV_2O_4) is consistent with the material being close to a metal-insulator transition, away from the standard activated behaviour found in the more insulating isoelectronic compounds.[41] This gives further evidence for the validity of our description of the dimerized compound.

3.5 Summary

We have shown that a structure optimization carried out for ZnV_2O_4 including strong-correlation effects confirms that the structure of the material close to the

itinerant electron limit, where U/W is small, is distorted below tetragonal symmetry. A symmetry reduction from the standard space group is predicted by our calculations, that would allow for different V-V distances along the [011] and [101] direction of the spinel structure. The proximity to the transition causes a structural deformation leading to the formation of V-V molecular orbitals in an ionic matrix. Such a distortion naturally explains the magnetic structure of the material experimentally observed. This structure would lead to an electrical polarization below the magnetic ordering temperature, that has been recently found experimentally.

We have analyzed the electronic structure of the oxide spinel ZnV_2O_4: we have studied the effect of applying pressure on the compound in the dimerized structure and have observed a Mott-Hubbard insulating character at high pressure. The dimerization of the V-V chains in the spinel structure, produced by the proximity to a metal-insulator transition, prevents the system to reach a fully metallic state. The appearance of an additional Peierls-like gap retains the system on the insulating side of the transition. This has also been recently seen experimentally. This contrasts with the the non-dimerized case, as we also studied here for the case of MgV_2O_4. If a non-dimerized structure occurs, and the V-V distance becomes small enough, below 2.94 Å, itineracy is reached, as has been found for CoV_2O_4 recently.[79]

We have also calculated the thermopower of the Zn dimerized spinel and have compared it with experimental measurements. Calculated Seebeck coefficient of the dimerized structure shows a linear (non-activated) behaviour, and fits nicely with experimental measurements. This provides additional support to our description of the lattice distortions that occur in ZnV_2O_4 close to the metallic state.

USC
UNIVERSIDADE
DE SANTIAGO
DE COMPOSTELA

4

Charge transfer in CrN magnetic phase transition and anomalous bulk modulus reduction.

4.1 Introduction

We have so far seen how approaching a metal-insulator transition changes the nature of the chemical bond, it can delocalize charge into homopolar bonds like in ZnV_2O_4. In this chapter we see that the consequences of the changes in the chemical bond that occur close to a metal-insulator transition not only affect the electronic properties of materials but they can also drastically change their mechanical properties.

The four sp^3 hybrids of carbon in diamond form the strongly covalent and directional bonds responsible for its hardness and ultralow compressibility. These properties make diamond widely used in coatings, polishing and cutting in the tool industry even though the cost of its artificial synthesis and its ineffective cutting of ferrous materials limits its practical applications. Group IV nitrides, BN, PtN and some metallic carbides or borides present a set of mechanical properties that could make these materials an alternative to diamond.[80, 81] However, some of them are economically and environmentally expensive as a result of synthesis under extreme conditions, which has hampered their widespread application. On the other hand, chromium nitride (CrN) has raised great expectations over recent years as it combines an ease of film deposition, high thermal stability and corrosion resistance with the prediction of a very large bulk modulus ($K_0 \approx 361$ GPa[82]). Yet, in spite of this high potential, experimental measurements of K_0 in CrN are lacking.

Here we report a drastic, about 25%, reduction of K_0 in stoichiometric CrN above ≈ 1 GPa. Our *ab initio* calculations were used to understand and confirm the experimental (structural and magnetic) data available. We demonstrate that this anomalous softening has its origin in a purely electronic effect that lies at the very nature of the chemical bond.

4.2 Computational Details

Calculations based on the density functional theory were carried out with the WIEN2k software[23, 24] and a full-potential, all-electron scheme on the basis of the APW+lo method,[21] as we described in section 1.2.7. The muffin-tin radii chosen were 1.99 a_0 for Cr and 1.76 a_0 for N, where a_0 is the Bohr radius. Local orbitals were added to improve the flexibility in dealing with semicore states (Cr $3s$, $3p$ and N $2s$). All the calculations were converged with respect to the parameters used, up to $R_{mt}K_{max} = 6$ and a k-mesh $12 \times 12 \times 12$ in the irreducible wedge of the Brillouin zone.

The electronic structure was calculated by introducing strong correlations by means of the LDA+U method[28] to deal with the Cr d electrons. We used a value of $U = 4$ eV (effective U, $U - J$, where U is the on-site Coulomb repulsion and J the on-site Hund exchange coupling).

4.3 Results and Discussion

Stoichiometric CrN presents a cubic rock-salt (space group $Fm3m$) paramagnetic structure at high temperatures that becomes orthorhombic (space group $Pnma$) and antiferromagnetic (AF) below 285 K; the structural transition was tentatively attributed to a large exchange-striction effect.[83] A depiction of the cubic rock-salt structure, typical of CrN, can be observed in Figure 4.1 a). It consists of a fcc structure (formed by Cr atoms, large blue balls) where each Cr atom is surrounded by an octahedral environment of six N atoms (small green balls), along the main lattice directions. In Figure 4.1 b) we display the orthorhombic $Pnma$ structure in the (001) cation planes of the $Fm3m$ cubic structure, with the unit cell indicated with dashed lines and the AF order found at this low-temperature orthorhombic structure.

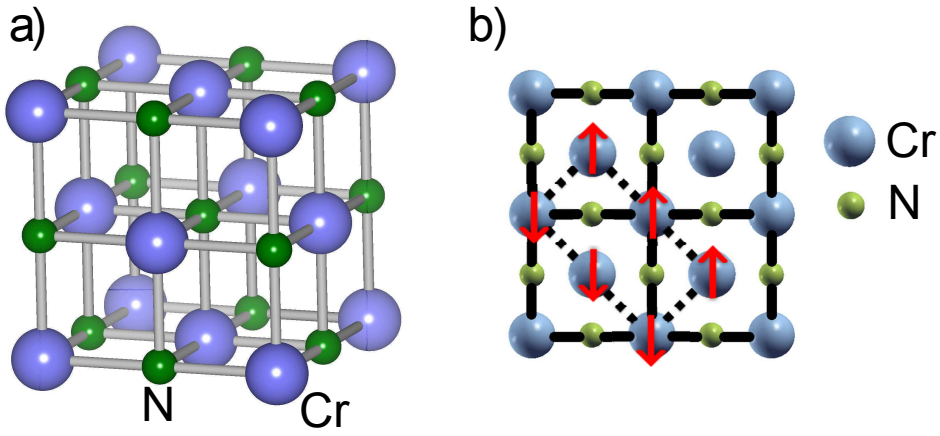

Figure 4.1:
Structure of cubic rock-salt CrN. Large blue balls represent Cr atoms and small green balls represent N atoms. In figure a) we observe the alternation in the atomic positions between Cr and N atoms, as it occurs in NaCl. Figure b) shows the (001) cation planes of the $Fm3m$ (cubic) structure of CrN, with the $Pnma$ (orthorhombic) unit cell indicated with dashed lines and Cr magnetic order with red arrows after Ref. [84].

It can be observed that a pressure-induced structural transition at ≈ 1 GPa from the low-pressure $Fm3m$ to the high-pressure $Pnma$ structure. The application of the Birch-Murnaghan equation[66] over the volume-pressure data measured[85] allows to calculate the value of the bulk modulus of these two phases of CrN (cubic rock-salt $Fm3m$ and orthorhombic $Pnma$). These fittings of $V(P)$ above the structural transition result in $K_0 = 243(10)$ GPa for the orthorhombic structure stable at high pressure. But the small number of points that are available below 1 GPa makes the estimation of a reliable value for K_0 in the cubic phase difficult for experimentalists. The error increases very much as P is reduced, increasing the difficulty of the analysis for the low-pressure cubic phase to check the large value of K_0 obtained by a direct fitting of the Birch-Murnaghan equation.

To provide further confirmation of the reduction of K_0 at the structural transition, as well as to confirm the values measured, we have calculated *ab initio* the bulk modulus in both phases. We have used the data obtained from the high-resolution synchrotron experiments as the starting point for the structural relaxation, and use the GGA approximation for that. Calculations show a change from $K_0(Fm3m) = 340(10)$ GPa to $K_0(Pnma) = 255(5)$ GPa, confirming a drastic

Table 4.1:
Experimental and calculated values of bulk modulus for VN and CrN (in the cubic and the orthorhombic phases). Calculated ones include the GGA approximation and the LDA approximation.

Material	Experimental	Calculated (GGA)	Calculated (LDA)
VN	265(5) GPa	280(2) GPa	250(10) GPa
CrN (cubic)	410(20) GPa	340(10) GPa	430(10) GPa
CrN (orthorhombic)	240(10) GPa	255(5) GPa	260(10) GPa

reduction ($\approx$ 25%) of the compressibility in the orthorhombic phase. The value of the bulk modulus in both structures of CrN was calculated with the GGA approximation.[13]

The paramagnetic phase was simulated by using the structural parameters in the paramagnetic regime and carrying out a non-magnetic calculation without considering the spin degrees of freedom of the system. Typical deviation in the determination of the bulk modulus B are within 5-10% with respect to experimental determinations is typically due to the quality of the fittings and the different number of points used.

We have also calculated the values of K_0 within the LDA approximation to the exchange-correlation potential, obtaining the following results: 430 GPa for cubic CrN and 260 GPa for orthorhombic CrN. Although the value for the cubic phase is larger in this case, these results give a strong support to our conclusions about the change in the bulk modulus of CrN at the pressure-induced structural transition. Also, we have calculated a value of 280(10) GPa for VN in the GGA approximation and 250 GPa within the LDA. Any of them correlates very well (within 10%) with the experimental estimation of 265(5) GPa. This agreement provides extra support for the accuracy of the calculations. In Table 4.1 the values of bulk modulus for VN and CrN are presented using different approximations for the exchange-correlation potential, together with the available experimental measurements. Note that the agreement between calculations and experiment are reasonable in all cases.

The value of the cubic K_0 is among the largest reported in nitrides, comparable to those of PtN_2, IrN_2, MoN, BN, RuN_2 or other systems such as OsB_2. In the high-pressure orthorhombic phase, K_0 decreases to values typical for other metallic nitrides such as TiN or VN (K_0=265(5) GPa from the experimental estimations[85]).

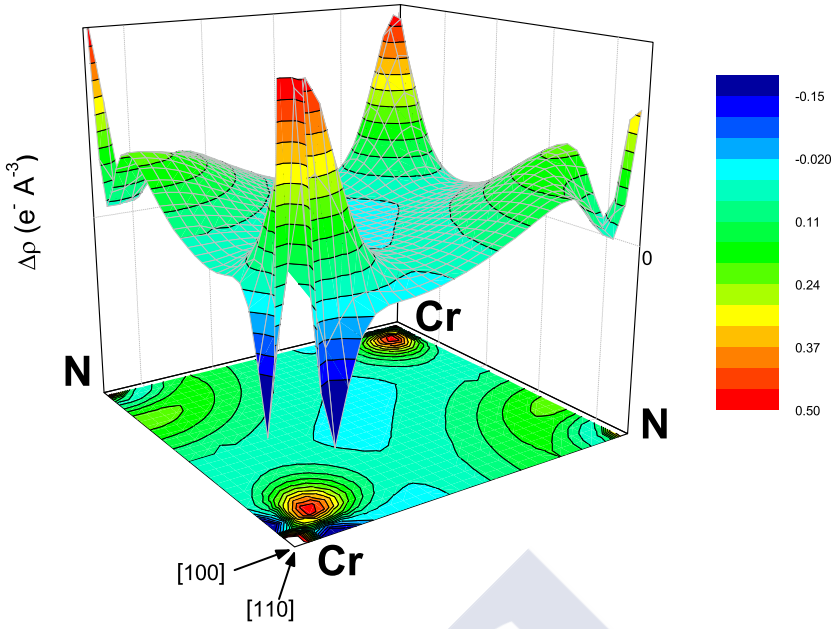

Figure 4.2:
Ab initio calculation of the charge-density difference between the high-pressure $Pnma$ and low-pressure $Fm3m$ phases of CrN. There is an appreciable charge transfer from the Cr e_g orbitals directed along the covalent Cr-N bond towards the more ionic t_{2g} orbitals of the Cr-Cr bonds.

The strong reduction of K_0 will most probably be reflected in a variation of the hardness of CrN owing to the correlation that normally exists between the two effects. This could have important technological implications, because the $Pnma$ phase should be avoided for certain practical applications (the same phase will also occur below 285 K at ambient pressure). Similar variations in the hardness/compressibility have been reported in other systems (Zr_3N_4 or BN) to be associated with structural transitions.[86]

The large K_0 of cubic CrN is presumably due to the strong covalent and highly directional bonds between the Cr:3d (e_g) and N:2p orbitals that must be modified in the $Pnma$ phase at some energy cost. We have analyzed the characteristics of this chemical bond by means of our electronic structure calculations. The result of the charge density redistribution across the structural transition confirms this point.

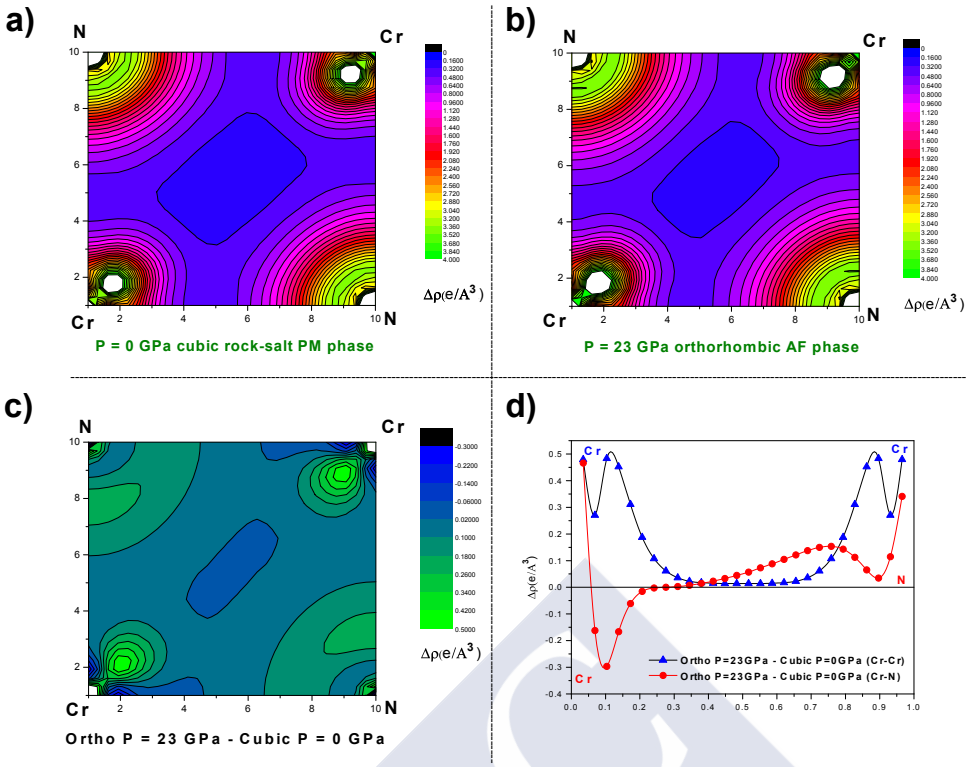

Figure 4.3:
Charge distribution along Cr-Cr bonds an Cr-N bonds on the low pressure paramagnetic cubic rock-salt structure (a) and high pressure antiferromagnetic orthorhombic structure (b) on the (001) plane. c) shows the difference between b) and a). On the down-right figure (d) we observed the charge redistribution along the main directions Cr-Cr bonds and Cr-N bonds.

Figure 4.2 shows the calculated charge-density difference between the high-pressure orthorhombic and low-pressure cubic phases of CrN. Cr-Cr and Cr-N distances at both pressures were normalized for the subtraction of electron densities. There is a considerable charge transfer from the Cr e_g orbitals that form the covalent Cr-N bonds (negative peaks along [100] and [010]) towards the more ionic t_{2g} orbitals of the Cr-Cr bonds (positive peaks along [110]) at the transition. Most of the charge was accumulated around the Cr ion, with a small charge variation in the intermediate zones of Cr-N bonds and Cr-Cr, because of the small quantity of charge in that region in both phases.

Structural data of CrN shows that the ambient pressure Cr-Cr distance of ≈ 2.933 Å in the cubic phase splits into two non-equivalent distances below the orthorhombic transition: a longer one (≈ 2.965 Å) along the FM $[1\bar{1}0]$ direction, and a shorter one (≈ 2.883 Å) along the AF [110] direction. The Cr-N distance remains practically unchanged. The same effects are observed with increasing pressure, which reduces the short Cr-Cr distance along [110] even further. The charge redistribution associated with this transformation can be still analyzed in more detail.

Figure 4.3 shows the data of the charge distribution on the (001) plane in the low-pressure cubic phase (Figure 4.3 a)) and the high-pressure orthorhombic phase (Figure 4.3 b)) after the normalization of the Cr-Cr and the Cr-N distances. It can be observed that most of the charge is accumulated around the Cr and N ions, with no important amount of charge in the intermediate Cr-N and Cr-Cr bonds. There are some differences between both phases in the charge distribution. In order to compare the changes in the charge distribution between the two phases we make the subtraction between the charge distribution of these two phases. These allows to observe the charge transfer from the Cr-N bonds (near Cr atoms) to the Cr-Cr bonds (near the Cr atoms) in Figure 4.3 c), remaining the charge density in the intermediate zone of Cr-N and Cr-Cr bonds invariable. A one-dimensional picture of the charge redistribution (Figure 4.3 d)) is even clearer to observe the situation. In that figure we plot the charge redistribution only along the Cr-Cr and the Cr-N bonds, and not along the full (001) plane and the same charge transfer behaviour can be observed. We observe a reduction of the charge near the Cr ions along the Cr-N bonds, that practically goes fully to the Cr-Cr bonds near Cr ions, as could be seen in the three dimensional plot in figure 4.2. What this means is a change in the nature of the chemical bond between the two phases. In the magnetic orthorhombic phase, larger charge accumulates along the more ionic Cr-Cr bond, whereas in the non-magnetic/paramagnetic cubic phase, charge piles up along the more covalent Cr-N bond, with the corresponding increase in bulk modulus. The increase in charge along covalent bonds is, hence, associated with an increased hardness in CrN. This charge transfer at the phase transition is brought about by the proximity of CrN to the itinerant electron limit that allows, as we have seen in previous chapters, for charge delocalization and bond-length fluctuations.

Our results suggest that the strong electronic correlations not considered in previous LDA calculations[83] could be an important ingredient to understand the

structural instability. It is perhaps pertinent to note that the softer K_0 values of VN and TiN may also be due to an itinerant-electron M-M (metal-metal) bond that is longer than its equilibrium value. In these materials, both cation and anion vacancies are introduced to reduce the M-M separation, but at the expense of the M-M bonding. Pressure reduces the M-M separation towards the equilibrium value for itinerant-electron bonding, thereby softening K_0. The Cr-N distances remain practically invariant across the transition, and hence we could assume that their force constant changes little. Then, the higher compressibility of the lower-volume phase is made possible by the longer-than-equilibrium Cr-Cr bond length, which results in a smaller variation of the internal energy with volume than expected.

4.4 Summary

CrN is a material that softens dramatically in the low-temperature/high-pressure AF *Pnma* phase. Such softening is connected with a change in the very nature of the chemical bond, as we have shown by an analysis of the charge transfer between a more covalent Cr-N bond (typically mechanically strong) to a more ionic Cr-Cr direct bond (softer). These bond softening effects occur in CrN due to the proximity to the itinerant electron limit. In such case, bond length fluctuations take place and in the case of CrN the result of those is the charge transfer we observe.

Important technological implications result from this work. In order to make use of the high K_0 and hence its good mechanical properties, the transition towards the AF phase needs to be prevented. This can be done by growing CrN in thin film geometry (which is good for coatings and other applications), on top of the appropriate substrate so that the in-plane strain prevents the system from having a structural/magnetic transition, and thus retaining the mechanical properties of the paramagnetic cubic phase.

5

Phase separation in $La_{1-x}Ca_xMnO_3$ via nanoscale doping inhomogeneities

5.1 Introduction

To continue our study of phenomenology close to a metal-insulator transition, we turn now to one of the most studied systems, perovskite manganites, whose phase diagram includes various metal-insulator transitions. We will study the consequences on the electronic structure of a doping-induced metal-insulator transition, focusing on the phase separation that occurs close to the localized-to-itinerant crossover.

The study of perovskite oxides has attracted the interest of the scientific community for more than 50 years already. Since the beginning of the fifties, the properties of transition metal oxides in general have been understood through using perovskite-based compounds. Seminal works by Anderson,[87, 88] Zener,[89, 90] Goodenough,[91, 92] Mott[93, 94] or de Gennes,[95] among others, first showed that the magnetic properties of transition metal oxides were far from trivial, due to the interplay between structure, magnetism and conduction properties, mainly caused by the versatility of the d electrons to behave either as localized or itinerant particles.

The perovskite structure, ABX_3, whose name comes from the Russian mineralogist L. A. Perovski (1792-1856), shows a great chemical flexibility, which allows, in the case of oxides ($X{=}O^{2-}$) 25 different elements of the periodical table to occupy the A position, and about 50 elements in the the B site. In the case of transition metal oxides (especially when B is a $3d$ ion) the possibility of doping with

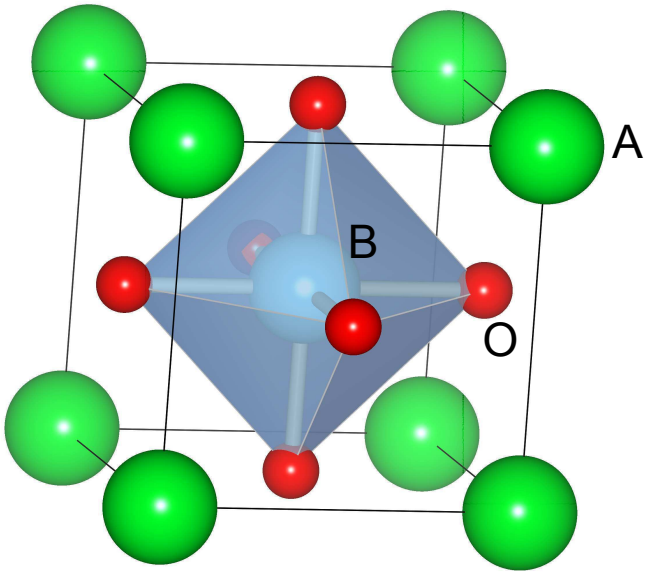

Figure 5.1:
Representation of a cubic perovskite structure. A is a di- or trivalent cation (such as La, Ca or Sr) and B is a transition metal ion (such as Ti, Co or Mn). B is octahedrally coordinated by six O atoms.

elements in different oxidation states in the A position introduces mixed valence in the transition metal site.

One of the important factors that allows transition metal oxides to present a vast amount of different physical properties is their versatility to accept different dopants. Many of them crystallize in structures derived from the cubic perovskite structure ABO_3, where A is often a divalent or trivalent cation (typically an alkaline or rare earth) and B is a transition metal ion.

In the cubic perovskite structure, shown in Figure 5.1, it can be seen that the transition metal ion (B) is octahedrally coordinated by six oxygen atoms, and in the corners of the cubic cell there are eight A cations, equidistant to the B cation. In general, we can discuss about two fundamental distortions in this kind of materials. These are:

1. **Cooperative distortion of the BO_6 octahedra.**

   This distortion is due to the size of the A cation (normally a lanthanide or an alkaline-earth) being much smaller than required to fill the empty space between the octahedra. The cooperative rotations of the BO_6 octahedra reduce the B-O-B bonding angle from 180°, at the time that drive the structure towards a situation of maximum packing. This distortion is the most important to determine the crystal symmetry of the resulting perovskite.

   Goldschmidt introduced a quantity called "tolerance factor", t, to evaluate the distortion of the perovskite due to this size mismatch with respect to the ideal cubic structure:

   $$t = \frac{d_{A-O}}{\sqrt{2}d_{B-O}} \tag{5.1}$$

   where the A-O and B-O distances can be approximated by the sum of the ionic radius for the different ions in the structure in order to make predictions about the expected distortions.

   The ideal cubic structure shows a value of $t = 1$, although the perovskite structure is stable in the interval $0.75 < t < 1$. As the tolerance factor decreases the symmetry also decreases:

   (a) $0.90 < t < 1$**:** rhombohedral structure, whose space group is $R\bar{3}c$ (no. 167). This is the case of $La_{2/3}Sr_{1/3}MnO_3$.

   (b) $0.75 < t < 0.90$**:** The compound shows orthorhombic structure and the space group is Pbnm (no. 62). This is the case of $La_{2/3}Ca_{1/3}MnO_3$.

2. **Distortion of the BO_6 octahedra due to the existence of a Jahn-Teller ion.**

   According to the Jahn-Teller theorem, when the ground electronic state of an ion is degenerate, a spontaneous structural distortion will appear that will break the electronic degeneracy. This is the case of Mn^{3+} in octahedral coordination, as shown in Figure 5.2. In that figure, it can be observed the distortion along the *c*-axis (small-long oxygen-B-oxygen bonds) and in the *ab*-plane. This distortion, the Jahn-Teller distortion, produces in the case of B=Mn^{3+} ($3d^4$) the break-up of an orbital degeneracy because of a new

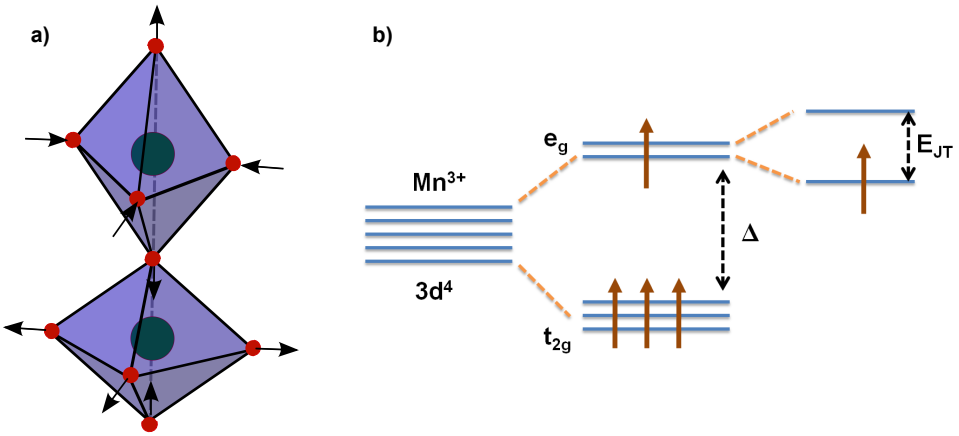

Figure 5.2:
a) Example of the Jahn-Teller distortion. Red points indicate oxygen atoms in an octahedral coordination whith the B ion (drawn in the centre of the octahedra). The arrows show the sense of the distortion. b) Energy levels of the Mn^{3+}:d^4 ion in octahedral coordination. The right part of the figure shows that when only one electron occupies the e_g levels, a Jahn-Teller distortion occurs to break the orbital degeneracy with the corrresponding energy gain, E_{JT}. Δ indicates the crystal field splitting.

energetic term, namely E_{JT}. This type of distortion only changes the bond distances, but does not change the group symmetry of the crystal.

Perovskite manganites belong to a class of materials that have become increasingly important in the last few years, particularly because of the large variety of phenomena they exhibit, closely tied to the strongly correlated nature of their electrons. The series of manganites $A_{1-x}B_xMnO_3$ (A^{3+} being a lanthanide and B^{2+} an alkaline earth) is one of the most intensively studied families.[96] The interest in these materials grew rapidly after the discovery of colossal magnetoresistance (CMR), a large negative magneto-resistance taking place under an applied magnetic field,[97] but also considerable research has focused on their unusual properties such as phase separation,[98] charge and orbital ordering[99, 100] and also for their potential applications in thin-film devices,[101–103] derived of its peculiar electronic structure properties.

The case of A = La^{3+} and B = Ca^{2+} has become a prototypical example of manganite compounds,[105, 106] showing a very rich phase diagram,[104, 107] as can be seen in Figure 5.3, where the phase diagram as a function of the Ca concentration and temperature is presented. In the figure we observe different regions at zero

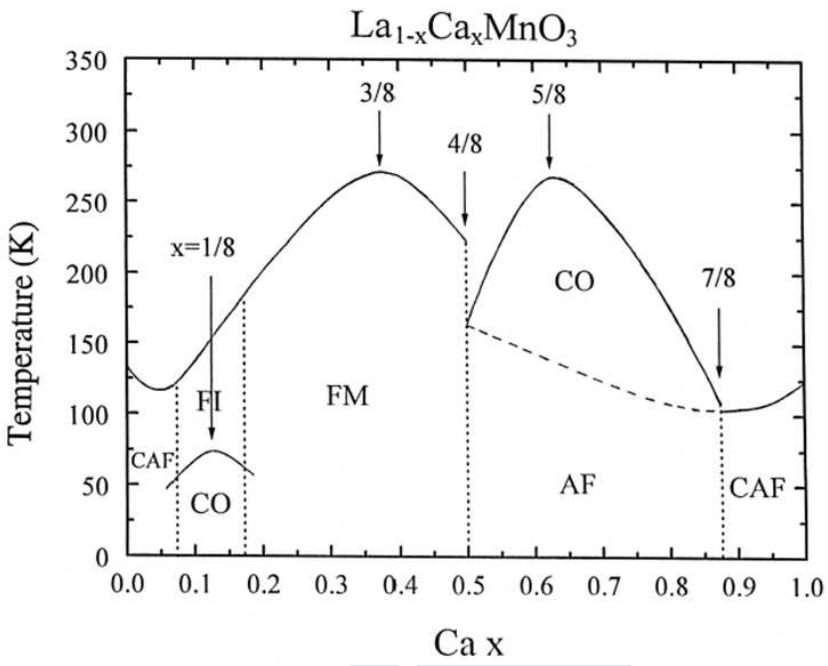

Figure 5.3:
Magnetic and electronic phase diagram of the series $La_{1-x}Ca_xMnO_3$, taken from ref. [104]. CAF: canted antiferromagnetic; FI: ferromagnetic insulator; CO: charge order; FM: ferromagnetic metallic; AF: antiferromagnetic.

temperature. Increasing x in the $La_{1-x}Ca_xMnO_3$ we explore all the possibilities from $LaMnO_3$ to $CaMnO_3$. At low Ca concentrations, the system is magnetically canted antiferromagnetic (CAF) insulator, as in high Ca concentrations, but in the region near $0.07 < x < 0.17$ a charge order (CO) phase appears, as in $x = 0.5$. Between $x \approx 0.18$ and $x \approx 0.5$, the system is a metallic ferromagnet (FM), and the region $0.5 < x < 0.87$ it is an antiferromagnetic (AF) insulator. While we introduce Ca^{2+} ions in the structure, we decrease the number of e_g electrons per Mn atom, varying the valence of Mn from Mn^{4+} to Mn^{3+}. Thus, we have a Mn^{3+} ($3d^4$ electrons with 1 electron in the e_g orbital doublet) in $LaMnO_3$ and a Mn^{4+} in $CaMnO_3$ ($3d^3$ electrons with no electrons in the e_g orbital doublet). The regions in the phase diagram with concentrations very close to 18% and 50% of Ca^{2+} have been thoroughly studied, because samples exhibit the phenomenon

of phase separation, intrinsic to the proximity to the magnetic/electronic phase transition. In those two regions of the phase diagram, $La_{1-x}Ca_xMnO_3$ presents mixed Mn^{3+}/Mn^{4+} valencies and a strong electron-phonon coupling, the magnetic coupling being a modified version of the double-exchange interaction to take into account the coupling between the electronic states and vibrational modes (vibrons). The mechanism for FM ordering in manganites exhibiting CMR has been recently considered,[108] suggesting a breakdown of the adiabatic approximation for the itinerant electrons. These results are related with dynamic phase segregation into hole-rich itinerant-electron regions and hole-poor localized-electron regions, leading to a suppression of the conventional double-exchange mechanism.

It is now widely accepted that some sort of electronic phase segregation is at the origin of the CMR effect in manganites. Moreo *et al.*[109] proposed a scenario where the coexistence of two phases with different charge densities is unstable against breakup into nanometer-size clusters due to the Coulomb force. Two different kinds of electronic phase segregation have been proposed to exist in manganites:[110] equal density vs. different density electronic phase segregation at the micro- and nano-scale, respectively. Experimentally, magnetic phase separation has been observed in the form of nanoscale phases with different magnetic properties,[111] i.e. regions in the crystal with nanometric size that present a different magnetic ordering. Imaging techniques[112] have recently shown the close relationship between nanoscale phase separated regions of an electronic/magnetic origin and CMR. According to those studies, these regions, on the several nm range, have not chemical origin. However, the role of nanometer-size chemical inhomogeneities has never been fully addressed.

The fundamental problem is to give a correct description of how the holes are distributed in the system. It has been known for long that even the simplest models[113] predict a non-uniform density distribution of dopants, which are unstable against segregation into hole-rich and hole-poor regions.

To gain insight into this problem, we have taken into account a structure with Ca^{2+} doping levels close to $x \sim 0.2$ (exactly $x = 0.1875$) in $La_{1-x}Ca_xMnO_3$ from a computational point of view via "ab initio" calculations. Typically, this is not done, and models are utilized instead, due to the large supercells that are required, but even the crudest supercells can help us, as we will see, to understand the electronic and chemical origins of phase separation or at least the crucial role that chemical inhomogeneities play in the properties of a phase separated system. It is worth recalling that the above mentioned doping level is experimentally placed around the

critical boundary in which the FM insulating to FM metallic transition occurs below the Curie temperature.[104, 107] we have constructed several superstructures in different magnetic configurations to explore the magnetic origin of phase separation. Since our calculations yield a homogeneous FM ground state (see section 5.3.1), we will analyze the influence of the Ca^{2+} dopant distribution in the lattice in this ground state. Varying the Ca^{2+} positions from a random distribution to a slightly correlated one (section 5.3.2.1), we can analyze the influence of the dopant distribution in the electronic structure and the physical properties of the compound by means of "ab initio" calculations. An analysis of the influence of the dopant distribution in the superconductivity and the phase separation has recently appeared[114] that studies the chemical inhomogeneities at the nanoscale in $(Ba_{1-x}K_x)Fe_2As_2$ superconducting pnictide, where it can be observed that variations of K dopants in the atomic scale results in a mixed scenario of phase coexistence and phase separation despite the strong local electronic inhomogeneities.

For the sake of completeness, we make a similar analysis (section 5.3.2.2) in a very different Ca^{2+} concentration ($x = 0.375$), in which the ground state is FM metallic becoming paramagnetic insulating at high temperatures (it can be seen in Figure 5.3, showing the phase diagram that at that x there is no competition between phases). The idea of that calculation is to study a concentration away from $x = 0.1875$ and also from $x = 0.5$, where the ground state becomes an insulating antiferromagnetic (AF) and charge ordered (CO) state. At those two hole densities there is a strong tendency towards phase separation caused by intrinsic inhomogeneities[96] but $x = 0.375$ (unlike $x = 0.1875$ and 0.5) is not close to the boundary between different ground states in the $La_{1-x}Ca_xMnO_3$ solid solution.[104, 107] These analyses will help us to discuss the implications of chemical inhomogeneities in these phase separated compounds.

5.2 Computational details

The method used to calculate the properties of the material was describe in section 1.2.7. Details of the calculations are the following. Values of U_{eff}: 2.7, 4.0 and 5.5 eV were used in the calculations. These values are on the range of those used in the past for various Mn oxides.[115, 116] The structural minimization was carried out using the GGA−PBE scheme[13] (generalized gradient approximation in the Perdew-Burke-Ernzerhof scheme) minimizing the forces on the atoms and the total

energy of the system. The parameters of our calculations[27] depend on the type of calculation but for any of them we converged with respect to the k-mesh and to $R_{mt}K_{max}$, up to 75 k points (15 in the irreducible Brillouin zone, in a 3 × 3 × 5 sampling of the full Brillouin zone) and up to $R_{mt}K_{max} = 6.0$. Muffin-tin radii chosen for $La_{0.8125}Ca_{0.1875}MnO_3$ were the following: 2.43 a.u. for La, 2.29 a.u. for Ca, 1.96 a.u. for Mn and 1.73 a.u. for O. Calculations with $La_{0.625}Ca_{0.375}MnO_3$ structure were carried out using muffin-tin radii values: 2.40 a.u. for La, 2.27 a.u. for Ca, 1.94 a.u. for Mn and 1.72 a.u. for O.

5.3 Results and discussion

5.3.1 Magnetic study

The goal of the first part of the work is to simulate a magnetically phase separated state by embedding a FM (AF) phase into an AF (FM) matrix. For this reason, we have set up several superstructures based on the unit cell $La_{0.8125}Ca_{0.1875}MnO_3$ (at a concentration close to a metal-insulator transition in the phase diagram), using a 2×1×2 and a 2×2×2 supercell (in perovskite unit cell units), as shown in Figure 5.4. The larger and initially more realistic cases (2×2×2) in Figure 5.4 (a), serve as a model of the experimentally observed situation of a magnetic phase (antiferromagnetic (AFREAL) in the upper panel, ferromagnetic (FMREAL) in the lower panel) completely surrounded by a magnetically different phase (FM and AF, respectively). Figure 5.4 (b) shows the cases of an AF chain surrounded by a FM guide (AFCHAIN) and vice versa (FMCHAIN), a more one-dimensional realization (probably less realistic). We have also calculated the system in the simple ferromagnetic (FM) and G-type AF cases (Figure 5.4 (c)).

All these phase separated superstructures have been calculated and their relative stability (total energy calculations) was compared with respect to an entirely FM structure and also an entirely AF structure (G-type). Results can be seen in Figure 5.5. We can see that the purely FM structure is the most stable one in every case, the stabilization energy ranging from 130 meV/Mn compared to the FMCHAIN and AFREAL structures to 400 meV/Mn with respect to the AF structure. Calculations predict that these magnetically phase separated states are not stable. The picture is the same for all values of U that have been tested. From these calculations, we can conclude that the FM configuration at the concentration $x_0 = 0.1875$ is the most

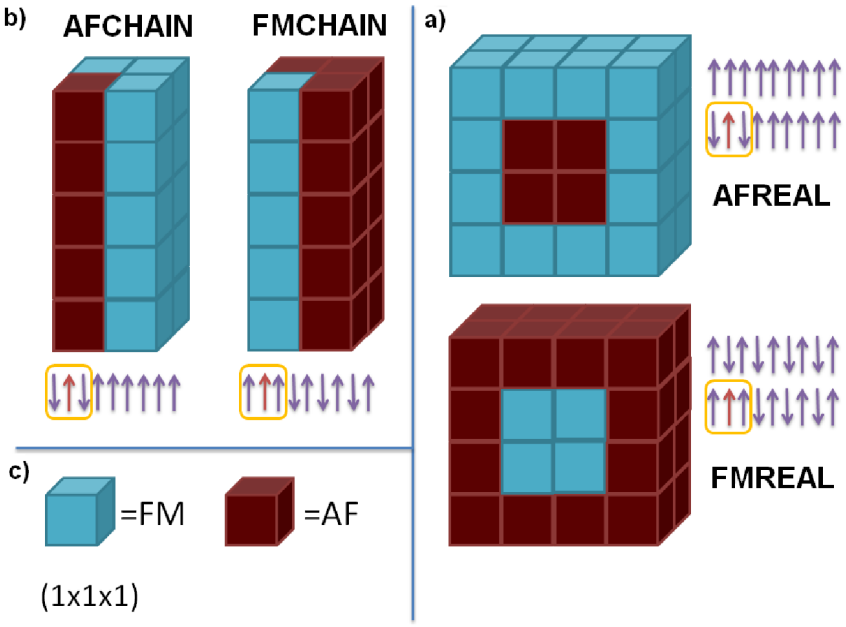

Figure 5.4:
Schematic cases of phase separated structures studied. On the right (a) we represent both realistic cases of phase separation (2×2×2): an AF nanometric region completely surrounded by a FM region (upper) and vice versa (lower). On the upper left (b) we represent the (2×1×2) cases, one dimensional AF chains surrounded by a FM guide and vice versa. On the lower left (c) we see a representation of the unit cell of $La_{0.8125}Ca_{0.1875}MnO_3$ (1×1×1) in the ferromagnetic (FM, blue) configuration and in the antiferromagnetic (AF, red) configuration.

stable, in agreement with experimental observations at that concentration.[104, 107] These results suggest that the coexistence of two magnetic phases in the compound require some other changes in the crystallographic and electronic structure for it to be stable. It becomes clear that magnetism alone cannot drive the system to a phase separated state with electronically segregated phases. Other mechanisms might be playing a role.[117]

5.3.2 Chemical study

There might be many mechanisms apart from pure static magnetic ordering that can play a role in inducing a phase separated state in perovskite manganites close to a metal-insulator transition. In this section we will focus on the possible effects of

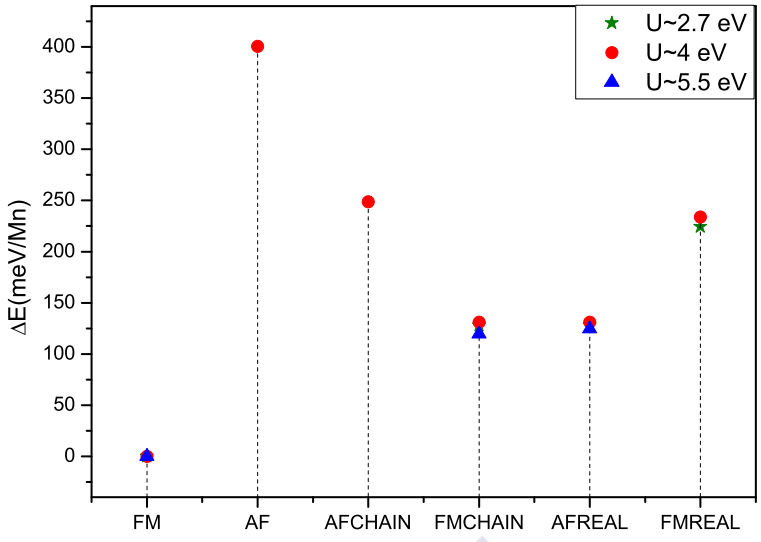

Figure 5.5:
Calculated energies of the constructed structures at several values of U within the LDA+U approximation. We take the more stable calculated case (FM case) as the zero energy state. All energies are expressed in meV/Mn.

nanoscale chemical inhomogeneities in driving the system towards a phase separated state, or at least being present in a system showing phase separation.

5.3.2.1 The case of x=0.1875

Holes in the e_g Mn levels can be introduced by substitution of La^{3+} by Ca^{2+} over the entire compositional range in the $La_{1-x}Ca_xMnO_3$ solid solution. Additionally, hole doping can be created by means of cationic vacancies. $La_{0.8125}Ca_{0.1875}MnO_3$ is a distorted perovskite with a pseudocubic lattice parameter (a_c) of 3.89 Å. The tilting of the MnO_6 octahedra results in an orthorhombic symmetry (space group *Pnma*, no. 62) with lattice parameters $a_o \approx c_o \approx \sqrt{2}a_c$ and $b_o \approx 2a_c$ for this composition. The ability to oxidize $La_{1-x}Ca_xMnO_3$ materials with $x \leq 0.2$ leads to important structural, electronic and magnetic variations related to the presence of cationic vacancies.[106, 118, 119] Thus, differences between non-stoichiometric and stoichiometric samples should always be considered.

It is common practice to assume, for carrying out electronic structure calculations with as small supercells as possible, that the La^{3+} and Ca^{2+} atoms (the dopants) are distributed in a random fashion throughout the crystal. Stoichiometric $La_{0.8125}Ca_{0.1875}MnO_3$ compound, i.e., with no cationic (and anionic) vacancies is considered in the present study. A perfectly homogeneous distribution of the dopants throughout the crystal was initially assumed. But, experimentally, this might not be the case; nano-sized chemical inhomogeneities in the structure can happen and will not be detected below the few nm limit,[112] but they could have a key role in the origin of phase separation. These inhomogeneities could have effects in the properties of the compound,[120, 121] including electronic structure. If they are present prior to the phenomenon of phase separation, they can provide an initial density imbalance between nanometric regions in the sample, that can act as a precursor of an electronic/magnetic phase separation if this is reinforced by additional mechanisms. For that reason, it is very important to elucidate how the dopants are distributed on the nanoscale.

The next step of the work is to study if such dopant inhomogeneities can occur, and if so, whether they would explain the observed nanoscale phase separation or at least see if they occur on a reasonable scale in space to complete/compare with the observed phase separated regions in the compound. To do this, we have varied the atomic positions of the Ca^{2+} atoms to distribute them in various manners throughout the crystallographic unit cell. In the $La_{0.8125}Ca_{0.1875}MnO_3$ structure we can change the distribution of the Ca^{2+} cations to create four possible inequivalent chemical configurations. These can be seen in Figure 5.6. Defining $< r >$ as the average distance between Ca^{2+} atoms in the lattice, and use it as a measure of how homogeneously these dopants are distributed, we have the following expression:

$$< r >= \sum_{i=1}^{N} \frac{d_i}{N} \tag{5.2}$$

Where d_i is the distance between nearest Ca^{2+} atoms and N is the number of nearest Ca^{2+} atoms.

In principle, inserting chemical inhomogeneities into the lattice will generate uncompensated forces and increase the elastic energy in the structure, but we need to calculate all the energetic terms involved to obtain the most stable configuration. In this work this is done using *ab initio* calculations.

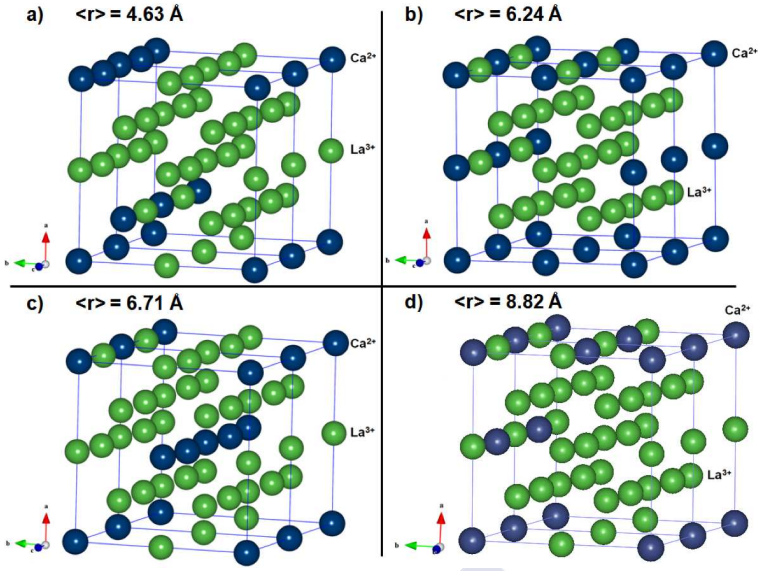

Figure 5.6:
Schematic representation of Ca^{2+} atoms distribution in the lattice of $La_{0.8125}Ca_{0.1875}MnO_3$. $< r >$ is the average distance between Ca^{2+} atoms in the lattice. These figures show the four possible atomic ordering of Ca^{2+} atoms in the lattice (because of its symmetry) and its $< r >$ from the most inhomogeneous case distribution (a) to the homogeneous case distribution (d).

Because of the symmetry of the structure, only four different configurations can be searched, with values of $< r >$ 4.3 Å, 6.24 Å, 6.71 Å and 8.82 Å, from the more homogeneous case to the more inhomogeneous case, respectively. We have constructed these four possible cases using a FM ordering, the most stable magnetic structure we explored previously. Fixing magnetic ordering allows to study the effects of chemical disorder alone. We have performed a full lattice relaxation for each of the cases, and then total energies of such structure have been calculated. The results are presented in Figure 5.7. We can observe that the most stable structure corresponds to an intermediate case between a totally homogeneous and a totally inhomogeneous case. Taking the ground state structure as the $< r >= 6.71$ Å, we found this one is more stable by about 19 meV/Mn with respect to the second more stable configuration, and by 219 meV/Mn to the more unstable configuration (largest chemical homogeneity attainable at this concentration). This means that a non-homogeneous dopant distribution occurs in the material that would lead to

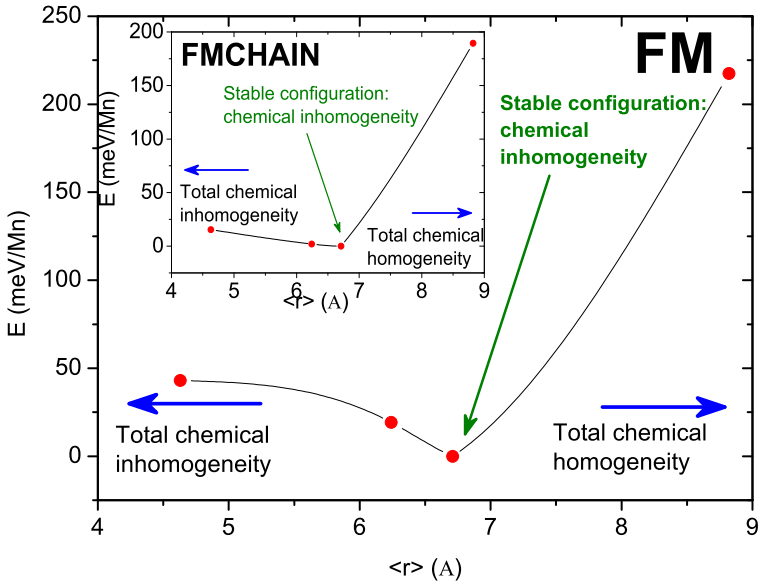

Figure 5.7:
Energies of the new calculated structures for $La_{0.8125}Ca_{0.1875}MnO_3$ in the FM configuration. The energies are normalized to the lowest value of the four possible Ca^{2+} chemical distribution configurations. The variable on the x axis is the value of $< r >$ for each structure, from the larger one on the right (total homogeneity structure corresponds with Figure 5.6 d) to the shorter one on the left (total inhomogeneity structure corresponds with Figure 5.6 a). The inset shows an analogous study for the second most stable magnetic configuration calculated in Figure 5.5, which is the FMCHAIN configuration.

a nanoscale distribution of effective concentrations. Analogous results in terms of dopant distribution energetics can be found in other magnetic configurations, as can be seen in the inset of Figure 5.7, so it is not an issue of the FM solution.

The most stable $< r >$ value is, hence, larger than one cubic perovskite lattice parameter. Several perovskite subcells will be involved in forming this ground state Ca^{2+} distribution. Let us remind ourselves that the closest Ca-Ca distance in a perovskite structure is one cubic lattice parameter. Moreover, variations in the atomic position of Ca^{2+} cations will imply different environments for each of the Mn atoms in the unit cell. Thus, the existence of areas with such a typical size suggests the magnetic and electronic characteristics differ inside and outside the clusters leading to an electronically inhomogeneous state on a nanometric scale in

Table 5.1:
Values of the atomic magnetic moment in units of μ_B inside the muffin-tin sphere for the ground state configuration. Values of total magnetic moment are 3.8125 μ_B per Mn atom, with an average valence $Mn^{3.1875+}$, the value expected from the electron count in a fully polarized half-metallic ferromagnet.

	Magnetic Moments		Magnetic Moments
Mn1	3.56	Mn5	3.56
Mn2	3.52	Mn6	3.52
Mn3	3.56	Mn7	3.56
Mn4	3.52	Mn8	3.52

$La_{0.8125}Ca_{0.1875}MnO_3$. Zones where Ca^{2+} atoms are grouped lead to a local concentration displacement towards the hole-rich region (Ca^{2+}-rich) in the phase diagram of $La_{1-x}Ca_xMnO_3$. Instead, zones where the density of Ca^{2+} atoms is lower, we have a La^{3+}-rich (electron-rich) zone, being a local concentration displacement to the AF region in the phase diagram. This scenario is consistent with the stable FM order[118] near Mn^{4+}, localized near the Ca^{2+}-rich region, in agreement with the hole distribution described by Alonso *et al.* as the hole attractor model.[119]

We have calculated the electronic structure of the material in the ground state (both in terms of magnetic ordering and chemical configuration). The values obtained for the total magnetic moment in this structure are of 3.8125 μ_B per Mn atom, as expected. This corresponds to an average Mn valence of 3.1875. We can also analyze the magnetic moments inside the muffin-tin spheres for each of the Mn atoms. These are summarized in Table 5.1, and present differences on the order of 1 % at most. This can be seen in the largely homogeneous electronic structure shown by means of the partial density of states of the inequivalent Mn atoms in the ground state of the compound (Figure 5.8). In a metallic solution, lacking charge localization, the way the chemical phase separation correlates with an electronic phase separation in the system is not obvious, but we observe that the chemical inhomogeneities relate to a different electron count in each Mn atom.

The typical sizes of these hole-/electron-rich zones that turn out from the calculations for the ground state chemical distribution can be seen in Figure 5.9. We observe there a $6.5-7.4$ Å diameter zone where the effective doping of $La_{1-x}Ca_xMnO_3$ has more Ca^{2+} than the real macroscopic average concentration ($x = 0.1875$) and

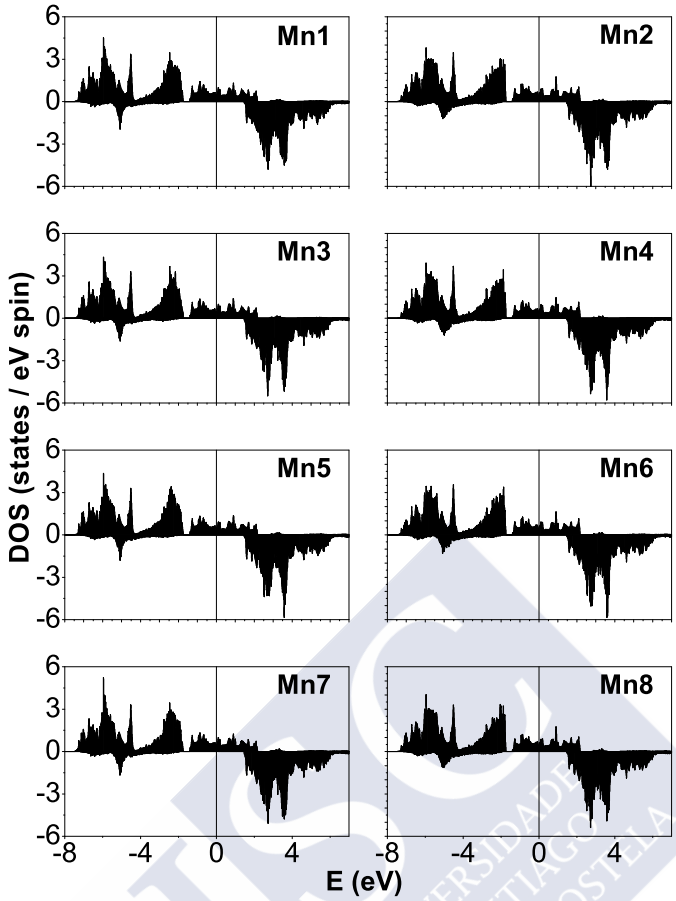

Figure 5.8:
Majority spin (positive values) and minority spin (negative values) partial density of states (DOS) plots of the eight inequivalent Mn atoms in the ground state (chemical and magnetically) configuration. Fermi energy is represented by a vertical line at E=0.

a $4.3 - 6.5$ Å diameter zone where the effective doping is displaced to the La^{3+}-rich zone in the phase diagram. These concentration displacements can be calculated analyzing the environment of the non-equivalent Mn atoms in our supercell. These calculated cluster sizes are comparable, but somewhat lower than those reported in literature[122] concerning the Ca-rich region in the $La_{1-x}Ca_xMnO_3$ solid solution. They show the importance of chemical ordering at the nanoscale as a driving force

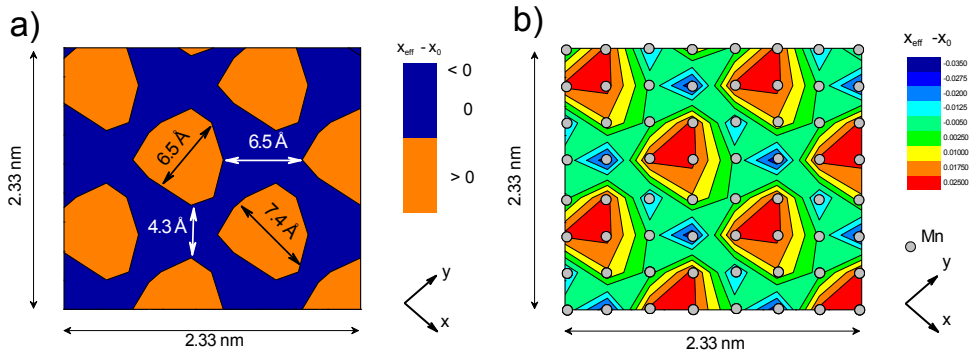

Figure 5.9:
a) Difference between local concentrations and global concentration of $La_{0.8125}Ca_{0.1875}MnO_3$. Orange colors indicate a hole-rich region on the phase diagram of $La_{1-x}Ca_xMnO_3$,[104] leading a concentration where the FM state is the ground state. Blue colors indicate an electron-rich region on the phase diagram (where the ground state is AF). The diagram shows zones of about 7.0 Å in typical size with Ca concentration $x_{eff} > x_0$ and other zones of about 5.5 Å with $x_{eff} < x_0$ ($x_0 = 0.1875$). b) The same image than a), indicating the positions of Mn atoms in the xy plane and the contour lines of the local concentration in the plane.

towards phase separation close to a metal-insulator transition or the presence of chemical inhomogeneities as counterparts or precursors of the electronic/magnetic phase separation scenario experimentally observed. The average deviation around x_0 =0.1875 is about 4% (slightly larger than the deviation in the magnetic moments of Mn atoms in a metallic phase, which is about 1%). Chemical variations are stronger than the observable local electronic variations in an itinerant solution. Changes seen in the local doping of each Mn vary from $0.167 < x < 0.208$, which are enough to move the system to the other side of the magnetic/electronic phase transition, that occurs at about $x = 0.18$. In fact, different nanosize domains have been experimentally detected around this compositional range: FM clusters of 16 Å for $x = 0.17$ whereas an approximate size of 8 Å has been observed for $x = 0.2$.[111] This last result confirms the existence of FM clusters confined in about two perovskite subcells. According to our calculations for $x = 0.1875$, chemical inhomogeneities of that same size will always be present in the samples, acting as nucleation centres for a possible phase separation phenomenon. If the sizes were on a different scale, chemical inhomogeneities could probably be ignored, but this is not the case. The zones with a lower Ca^{2+} concentration will have an AF ground state and the zones with higher values of x will be in their FM ground state, according to the phase

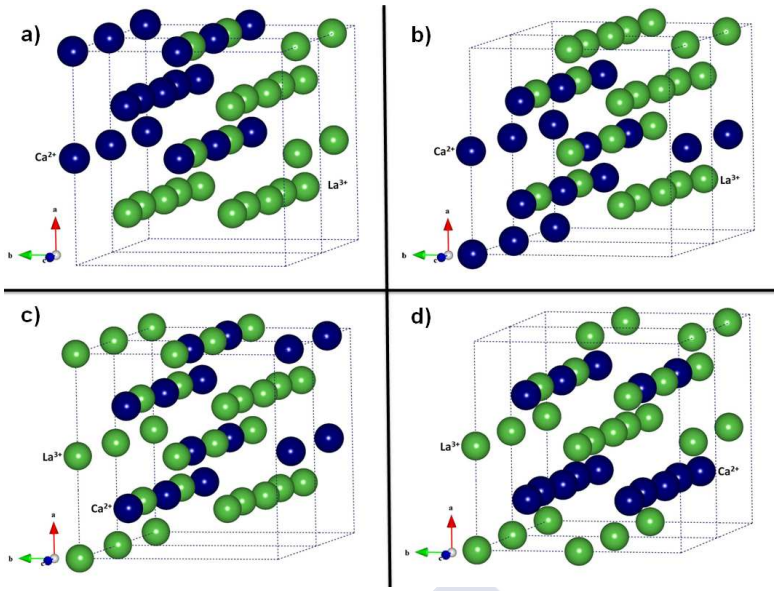

Figure 5.10:
Image of the distribution of La^{3+} and Ca^{2+} in $La_{0.625}Ca_{0.375}MnO_3$ in the four configurations of the dopants distribution. a) shows the totally dopant-inhomogeneous case (Ca^{2+} atoms are nearly between them in the lattice). Instead, d) represents the dopant-homogeneous case (Ca^{2+} atoms are distributed homogeneously in the lattice). Cases b) and c) represent intermediate cases between a) and d).

diagram of the system, and to the calculations.

5.3.2.2 The case of x=0.375

In order to further check the reliability of these calculations, we have analyzed a different Ca^{2+} concentration ($x = 0.375$) which is not at the boundary between different ground states in the $La_{1-x}Ca_xMnO_3$ solid solution.

$La_{0.625}Ca_{0.375}MnO_3$ crystallizes in an orthorhombic (space group *Pnma*) symmetry below a certain structural transition temperature T_s according to the work of C.-H. Yang *et al.*[123] The cell parameters measured correspond to a=5.4730Å, b= 7.7309Å and c=5.4875Å. We have constructed our unit cell from these parameters, and created a supercell ($2 \times 1 \times 2$) in order to introduce all the La^{3+}/Ca^{2+} atoms necessary to obtain the desired $x = 0.375$ concentration. We have performed a structural relaxation of the internal atomic positions for each of the structures analyzed, maintaining the same lattice parameters obtained from experiments. We

have exchanged the atomic positions of the Ca^{2+} and La^{3+} atoms of the structure to distribute them in various manners throughout the crystalline unit cell. In the $La_{0.625}Ca_{0.375}MnO_3$ structure we can construct four different structures (Figure 5.10), because of its symmetry, depending on how these Ca^{2+} atoms are arranged,[124] which can be described, as before, using the parameter $< r >$ defined in Eq. 5.2. We have labelled the case of total dopant homogeneity as the "away" case and the full dopant inhomogeneity structure as the "bulk" case. We introduce the parameter c as the degree of homogeneity of the Ca^{2+} distribution in the lattice, so that $c = 0$ indicates a situation of total inhomogeneity (associated with the case labeled "bulk") and $c = 1$ indicates a situation of total homogeneity (associated with the case labeled "away"). The two cases which are intermediate between "away" and "bulk" are called "inter" (Figure 5.10 c)) and "inter2" (Figure 5.10 b)) cases, for the more homogeneous and the more inhomogeneous intermediate structures, respectively. The evolution of c is linear.

Just like before, we need to calculate all the energy terms involved in the introduction of random dopants in the system. All the elastic energy terms will be captured by our full-potential *ab initio* calculations.

Table 5.2:
Energies of the calculated structures for $La_{0.625}Ca_{0.375}MnO_3$. The energies are given with respect to the lowest value of the four possible Ca^{2+} chemical distribution configurations. Structures are ordered from total homogeneity (top), corresponding to Figure 5.10 d) to total inhomogeneity (bottom), that corresponds with Figure 5.10 a). c is the degree of homogeneity in the Ca^{2+} distribution in the lattice

		U=2.7 eV	U=4.0 eV	U=5.5 eV
Structure	c	ΔE (meV)	ΔE (meV)	ΔE (meV)
away	1.0	79	78	78
inter	0.8	0	0	0
inter2	0.5	403	407	410
bulk	0.0	403	410	415

Once we have relaxed each structure, we can study the electronic structure properties using the LDA+U approximation to the exchange-correlation potential, utilizing several values of U that are typical for these moderately correlated compounds (U=2.7, 4.0 and 5.5 eV). As we can see in Table 5.2, the most stable configuration corresponds to one of the intermediate cases, that are midway between the totally

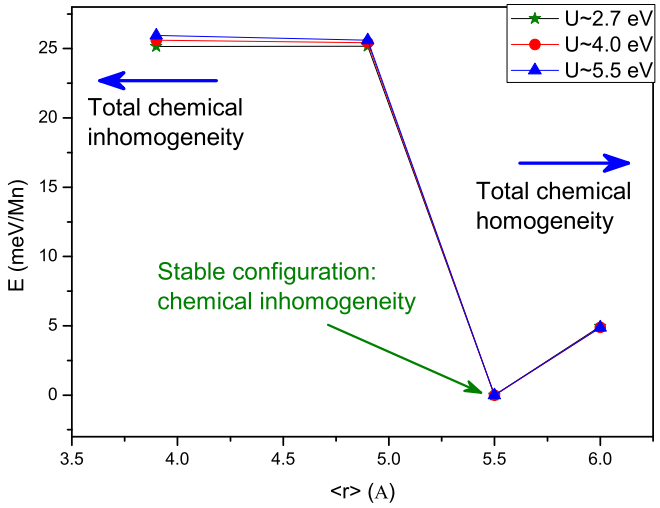

Figure 5.11:
Analogous study of energies for $La_{0.625}Ca_{0.375}MnO_3$ than Figure 5.7. Calculations were performed in a FM configuration (the more stable at this concentration) at several values of U, leading to similar results than $La_{0.8125}Ca_{0.1875}MnO_3$.

homogeneous ("away") and the totally inhomogeneous Ca^{2+} distribution on the lattice ("bulk" case). Results are largely U-independent.

This is an energy analysis similar to the one made in Figure 5.7 and shows that the chemical inhomogeneities that occur at this concentration are even larger in magnitude. The displacements in the local concentration of the $< r >= 5.5$ Å structure can be observed in Figure 5.11. They vary in the range $0.335 < x < 0.407$. Note that $< r >$ is smaller than in the $x = 0.1875$ case (i.e. 6.71 Å). This is related to the richer calcium concentration in $x = 0.375$. The above range of Ca^{2+} concentrations is always far enough from the FM insulator ground state at $x = 0.18$ as well as the AFM with CO ground state observed at $x = 0.5$. In spite of this, experimental evidence of inhomogeneities in manganites has been experimentally obtained.[96]

Random chemical doping in a lattice introduces local distortions propagating with a power-law decay $1/r^3$. This creates a long-range interaction among the ions of anisotropic nature, being attractive or repulsive depending on the direction.[125]

Table 5.3:
Values of the atomic magnetic moment in units of μ_B inside the muffin-tin sphere for the "bulk" and "away" configuration. Values of total magnetic moment are $3.625\mu_B$ per Mn atom for both cases, including the contributions from the interstice, with an effective valence $Mn^{3.375+}$, the value expected from the electron count in a fully polarized half-metallic ferromagnet (region where a plane wave expansion is used; instead a linear combination of radial functions times spherical harmonics is used inside the atomic spheres defined by the LAPW method).

	bulk	away		bulk	away
Mn1	3.15	3.21	Mn5	3.19	3.12
Mn2	3.17	3.13	Mn6	3.16	3.13
Mn3	3.15	3.21	Mn7	3.20	3.12
Mn4	3.16	3.21	Mn8	3.17	3.21

Hence, cooperative lattice distortions are fundamental for the long-range propagation of this effect. In a manganite at large doping, the interaction between different size La^{3+} and Ca^{2+} ions will result in a non-homogeneous distribution of the dopants, in order to meet the requirement of cooperativity and reduce the elastic energy.

We can also analyze how the introduction of dopant inhomogeneities changes the electronic structure of the system. According to the work of Schiffer *et al.*,[107] $La_{0.625}Ca_{0.375}MnO_3$ at low temperatures is a FM metal. The calculations were carried out using this magnetic configuration. The values obtained for the total magnetic moment in this structure are of $3.625\mu_B$ per Mn atom, that remains unchanged independently of the dopant distribution. This corresponds to a Mn valence of 3.375, being all the Mn valence electrons fully polarized in this half-metallic (see below) ferromagnet. We can also analyze the magnetic moments inside the muffin-tin spheres for Mn atoms. The values are summarized in Table 5.3 for the two most different structures (the more inhomogeneous one and the more homogeneous one). The value of the magnetic moment of the Mn cations can be used as a measure of the number of electrons per Mn to check how the local environment affects the particular valence of each Mn atom in the structure. Being the system metallic, we observe that the local dopant distribution does not affect the electronic structure of each particular Mn atom. The magnetic moments are very much the same for each Mn atom, irrespective of its local environment. Differences are on the order of 1% at most, as in the $x = 0.1875$ case.

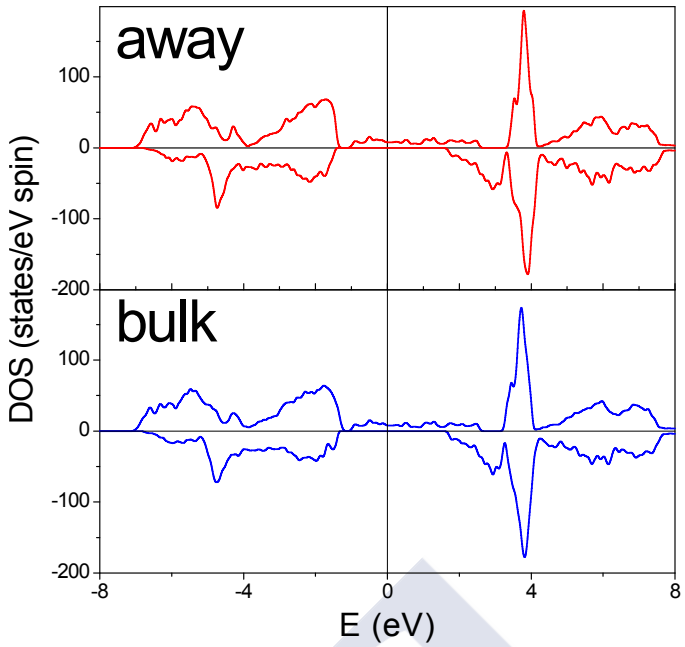

Figure 5.12:
Majority spin (positive values) and minority spin (negative values) total density of states (DOS) plots of $La_{0.625}Ca_{0.375}MnO_3$ in the "away" (upper) and "bulk" (bottom) configuration. Fermi level is represented by a vertical line at E= 0.

We can further explore this conclusion with the aid of the density of states (DOS) plots for both the most inhomogeneous and the most homogeneous structure (see Figure 5.12). No appreciable changes in the energy distribution of the occupations can be observed. The material is half-metallic (viz. conduction occurs only through one of the spin channels, leading to a perfectly polarized electron current). The contribution near the Fermi energy comes from the Mn d levels (Figure 5.13). The partial density of states of Mn atoms shows a homogeneous electronic structure of the inequivalent Mn atoms in the material, independent of the Ca^{2+} distribution. The minority spin channel does not present any Mn d occupation due to the large Hund's rule exchange constant typically observed in manganites. Mn perovskites often occur in a high-spin state because of this. In our case, we see that the majority e_g levels are lower in energy (hence slightly occupied) than the minority t_{2g} levels, confirming the expected situation of $J_{Hund} > \Delta_{cf}$, typical of Mn ions coordinated with oxygen atoms. Thus, there is only non-zero DOS for the majority channel at

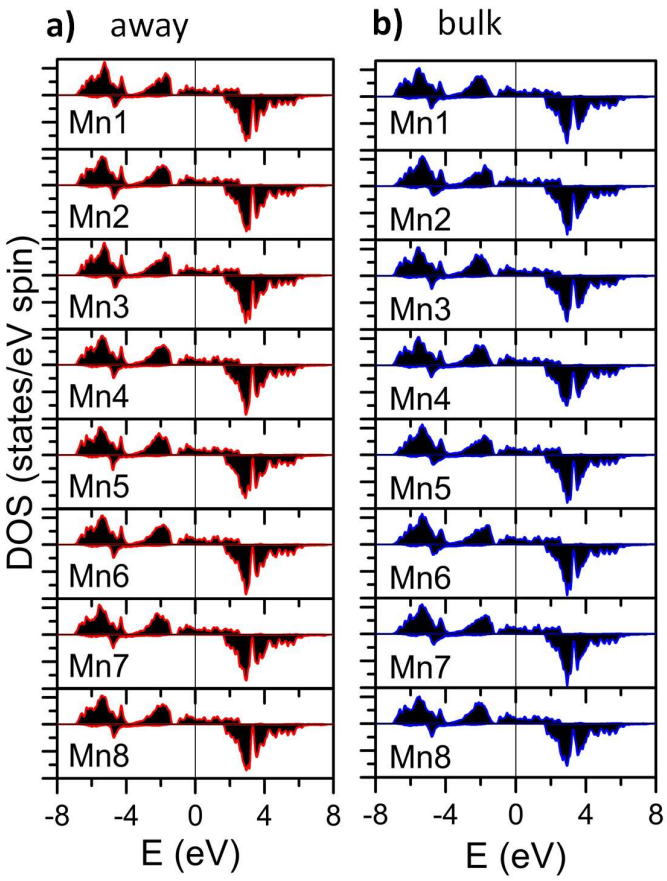

Figure 5.13:
Majority spin (positive values) and minority spin (negative values) partial density of states (DOS) plots of the 8 inequivalent Mn atoms in the "away" (most homogeneous) (a)) and "bulk" (most inhomogeneous) (b)) configuration. Fermi level is represented by a vertical line at E= 0.

the Fermi level (defined at zero energy in the plots), while the minority spin channel presents a gap of approximately 3 eV. The value of this gap is somewhat dependent on the choice of U, but all the other conclusions are independent of U, for the values studied in this work.

5.4 Summary

All these results show important evidences about an often forgotten factor (mainly due to the complications for its direct calculation) in studying the origin of electronic and magnetic phase separation close to a magnetic phase transition. We have calculated, by means of *ab initio* calculations, that magnetism is not the only player in driving phase separation. We have studied mixed magnetic phases but none of them is stable. However, chemical inhomogeneities caused by cation disorder in a scale smaller than 1 nm are stable in the system according to our total energy calculations. Introducing random chemical doping in a lattice produces local distortions and a long-range interaction among the ions of anisotropic nature, being attractive or repulsive depending on the direction. Thus, cooperative lattice distortions are fundamental for the long-range propagation of this effect. The interaction between different size La^{3+} and Ca^{2+} ions results in a non-homogeneous dopant distribution, in order to meet the requirement of cooperativity and reduce the elastic energy. Close to a FM/AF phase transition, these nanoscale doping inhomogeneities are large enough to drive the system to a phase separated state, leading to hole-rich/hole-poor regions in the compound on the nanometer scale. Chemical inhomogeneities on this small scale will always be present in this system, whether driving electronic/magnetic phase separation or accompanying it. If phase separation exists on the same nanometer scale, chemical inhomogenities are expected to play a big role as charge attractors and nucleation centres for a particular magnetic/electronic phase to develop locally. This would not be the case for a micrometer-size phase separation, in that case the effect of the inhomogeneities studied here would be negligible.

The electronic structure remains largely unchanged, irrespective of the Ca^{2+} distribution. The system is a ferromagnetic half-metal, with vast unoccupation of the minority-spin Mn states leading to a gap in the minority-spin density of states. The metallicity of the system leads to a homogeneous electronic structure of the inequivalent Mn atoms in the structure, leading to no appreciable changes in the Mn electronic structure among the different dopant distributions.

USC
UNIVERSIDADE
DE SANTIAGO
DE COMPOSTELA

6

Electronic structure and magnetism in weak itinerant ferromagnet CoS_2

6.1 Introduction

To finalize our journey, we conclude with results on an itinerant system, but a peculiar one, both because one of the spin-channels presents a gap (it is a so-called half-metal) and because its itineracy occurs with the presence of spin fluctuations (a so-called weak itinerant ferromagnet). We will see how one can understand its peculiar physical properties with the aid of *ab initio* calculations.

Half-metals[126, 127] are materials where metallic conduction occurs only through one of the spin channels, leading to a perfectly spin-polarized electron current. As depicted in Figure 6.1, one of the spin channels presents a gap at the Fermi energy (E_F) but the other one has bands crossing it. This makes them an interesting family of materials, in particular for applications in the field of spintronics,[128] where spin injection is required for controlling the charge and spin currents separately. Moving a strongly spin-polarized current is highly sought for, and half-metals are a good candidate for this. A few materials have been characterized as half-metals, starting from CrO_2 in the 80's by R. A. de Groot and others.[129] Experimentally, those highly spin-polarized compounds remain elusive and research is needed both for understanding the physics of these compounds and also to obtain better candidates for their use as spininjectors.

Several DFT-based electronic structure calculations have been done in the last few years, describing CoS_2 as a half-metallic ferromagnet.[130–135] However, the

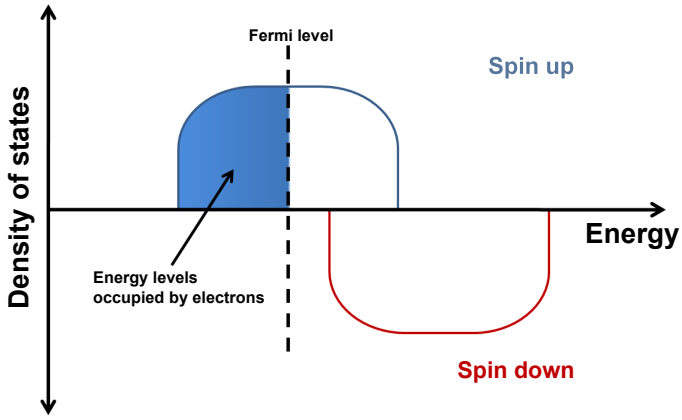

Figure 6.1:
Scheme of a half-metal. In the electronic state shown in the figure, spin-up electrons exist at the Fermi level, and there are no spin-down electrons. Namely, only spin-up electrons contribute to the conduction of electricity, while spin-down electrons do not contribute to it. This state is known as a half-metal.

electronic and magnetic properties of this material are not fully understood. Point-contact Andreev reflection measurements[136] showed a relatively low spin polarization of 56% at 4.2K.[137] This picture was confirmed in the studies by Wang[138] and Umemoto[139] in the $Co_{1-x}Fe_xS_2$ series, where they show that the spin polarization can be continuously tuned in the range $-56\% < P < +85\%$ and $-75\% < P < +100\%$ respectively. Recently the value of the polarization has been calculated as P= -72%[140] for CoS_2. Brown *et al.*[141] found from polarized neutron diffraction measurements that half-metallicity does not occur in the ferromagnetic phase. A sharp photoemission peak at the E_F in the ferromagnetic phase originates in the bottom of the $e_{g\downarrow}$ subband due to exchange splitting, indicating that the $e_{g\downarrow}$ band is partially filled in the ferromagnetic phase,[142] destroying the half-metallicity.

Recently it was found that the resistivity, specific heat and magnetic susceptibility of CoS_2 are dominated by exchange-enhanced spin-density fluctuations.[143] This previous work also showed that the GGA method[13] is enough to describe the electronic and magnetic behaviour of CoS_2 due to the non-localized nature of the compound. The introduction of strong correlation effects is not necessary to describe accurately its electronic structure properties but it is not enough to describe the enhancement of, e.g. the value of γ obtained from specific heat, which is

enhanced due to spin fluctuations unaccounted for in DFT calculations.

The important role of spin-orbit coupling (SOC) in a realistic description of half-metallic materials has been discussed in literature.[126, 144] Usually, the coupling between spin-up and spin-down states caused by a sizable SOC introduces non-negligible minority states at the Fermi level, destroying the half-metallicity. In general, this will depend on the strength of the interaction (that increases with atomic size) and also on the size of the gap and the position of the band edges in the insulating spin channel. The importance of minimizing the effects of SOC on destroying half-metallicity when designing new half-metals has been discussed in the past,[145] where utilizing cations with completely filled shells was suggested in order to reduce spin-orbit effects by minimizing the orbital angular momenta and, in the case of studying possible compensated half-metals, increasing the likelihood of the materials having no net magnetization.

However, most works have based their studies solely on the changes in the density of states at the Fermi level, but the degree of half-metallicity will be influenced by the changes in the conduction properties that derive from the reordering of states around the Fermi level introduced by SOC. Moreover, the conductivity of the minority spin channel will have an activated component that needs to be quantified beyond the value of the density of states at E_F.

We make an analysis of the electronic and magnetic properties of the ground state of CoS_2 and introduce SOC to determine its importance in the half-metallicity of this material. We also focus on explaining, from a band structure point of view, the features that help us to understand its behavior as an itinerant ferromagnet, governed by spin fluctuations. For analyzing the conduction properties of the material, its spin-dependence and the importance of SOC, we have made several transport properties calculations and have compared them with experimental measurements.

6.2 Computational details

Electronic structure calculations were performed within density functional theory[6] using WIEN2K software.[23, 24] In this chapter the exchange-correlation potential utilized was the Perdew, Burke and Ernzerhof (PBE) version of the GGA.[13] The geometry optimization was carried out minimizing the forces on the atoms and the total energy of the system. The parameters of our calculations depend on the type of calculation but for any of them we converged with respect to the k-mesh and to

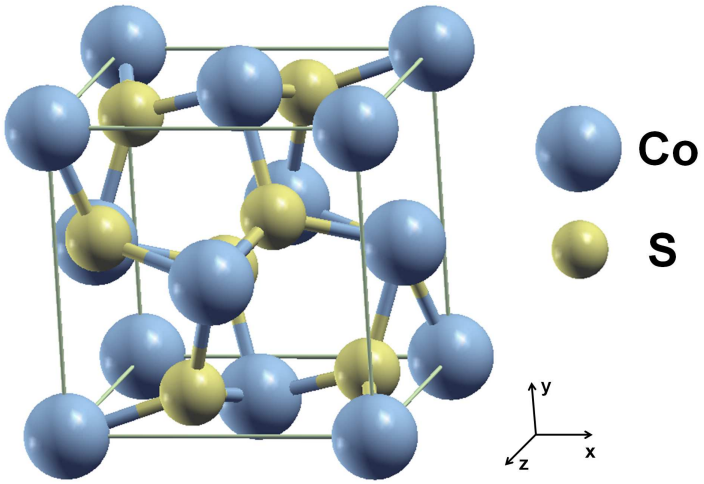

Figure 6.2:
Cubic pyrite structure of the CoS_2 compound. Large blue spheres represent Co atoms located on an fcc sub-lattice, and small yellow spheres represent S atoms, which are octahedrally coordinated with Co atoms.

$R_{mt}K_{max}$. Values used for the k-mesh are a $7 \times 7 \times 7$ sampling of the full Brillouin zone for electronic structure calculations and geometry optimization, $40 \times 40 \times 40$ for the density of states calculations and the very fine details of the influence of SOC in the half-metallicity of the compound. $R_{mt}K_{max} = 6.0$ is chosen for all the calculations. Local orbitals were added for a bigger flexibility in dealing with the semi-core states. Muffin-tin radii chosen were the following: 2.31 a.u. for Co and 2.04 a.u. for S.

All the calculations were converged with respect to all the parameters used, to the precision necessary to support our calculations (converged forces, total energy differences, etc.). For the calculations of transport properties we utilize the BoltzTraP code,[30] that uses the energy bands obtained from the WIEN2k software, we used a k-mesh in a $43 \times 43 \times 43$ sampling of the full Brillouin zone, where convergence was achieved. The calculation of transport properties requires a fine mesh to carry out the integrations in the Brillouin zone. SOC was introduced in a second-variational procedure.[27]

6.3 Structure

CoS_2 crystallizes in a cubic pyrite structure,[130] as shown schematically in Figure 6.2. Co and S atoms are located, respectively, at the Wyckoff positions 4a (0,0,0) and 8c (u,u,u) of the space group $Pa\bar{3}$, no. 205. Co atoms are octahedrally coordinated by 6 S neighbours. From X-ray diffraction experiments on large single crystals ($3 \times 3 \times 3$ mm^3),[143] the lattice parameter obtained for the material was a= 5.518 Å. Also, electronic structure calculations were performed to optimize *ab initio* the structural free parameter characterizing the S position. This was calculated in order to minimize interatomic forces and the total energy of the system. The value obtained was u= 0.387 (see Table 6.1), smaller than that measured by Wyckoff[146] and in in good agreement with a structure relaxation performed in a previous work.[135] Calculations to obtain the lattice parameter from *ab initio* were carried out yielding a value of a = 5.55 Å, which is within the typical accuracy of density functional theory calculations (2% in volume).

Table 6.1:
Crystallographic positions at $T = 0$ that result from our structure optimization. The structure is a cubic pyrite structure, with space group $Pa\bar{3}$, no. 205. Lattice parameter is a= 5.518 Å.

Atom	Crystallographic position	Coordinates
Co	4a	(0,0,0)
S	8c	(0.387,0.387,0.387)

6.4 Results

6.4.1 Electronic structure and magnetism

The electronic structure of CoS_2 is characterized by a large covalency due to the extended S p bands overlapping largely the Co d bands close to the Fermi level. Also, the itineracy of the compound helps in making difficult to establish an ionic picture for the material. Some earlier reports suggest an effective Co^{2+}:d^7 state,[133] distinct from the purely ionic picture, that would naively yield Co^{4+}:d^5 if one assumes an S^{2-} valence. This is far from the real electronic structure of the compound.

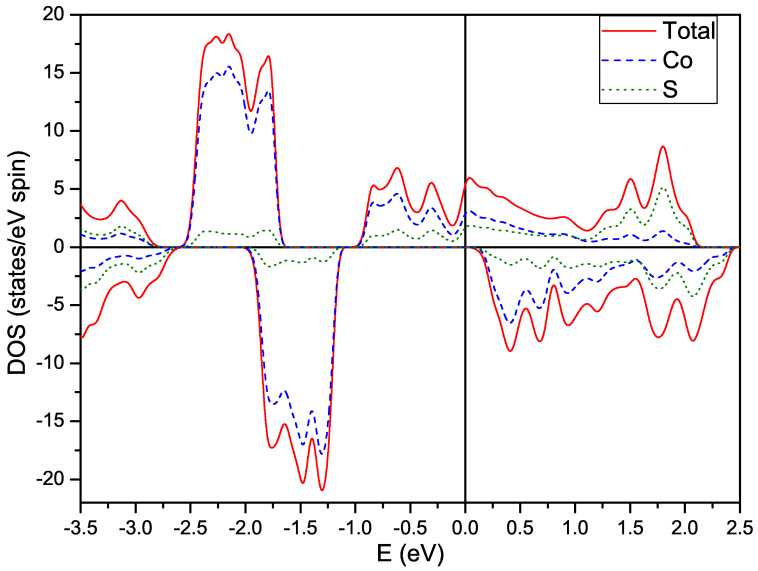

Figure 6.3:
Spin-up (positive values) and spin-down (negative values) total density of states (DOS) plots for the CoS_2 in the ground state ferromagnetic configuration. Partial density of states have been plotted also (dashed blue lines for Co total DOS and dotted green lines for S total DOS). Fermi energy is at zero. The system is half-metallic.

Our results show that the orbital occupations are close to the Co^{2+}:d^7 state. As expected, large covalency occurs in the compound, as can be seen in the density of states (DOS) plot shown in Figure 6.3. Big spectral weight from S p states appears near E_F and also significant weight can be seen at the top of the conduction band, showing the S p bands are not fully occupied. In this DOS plot, calculated within the GGA approach, we see CoS_2 presents a half-metallic character, as noted in several previous works.[133, 147] It shows the fully occupied t_{2g} bands of about 0.7 eV bandwidth at around -1 to -2 eV, that are spin-split by approximately 0.6 eV, and the broad $e_g^{\uparrow}$ bands crossing the Fermi level in the majority channel, being 2 eV wide. The $e_g^{\downarrow}$ bands are unoccupied, with their edge lying very close to the Fermi level. This proximity will make their occupancy non-zero under perturbations such as SOC, temperature or the application of an external magnetic field. A small amount of electron doping would also be able to populate them.

The value of the total moment obtained by ab initio calculations is 1.00 μ_B/Co

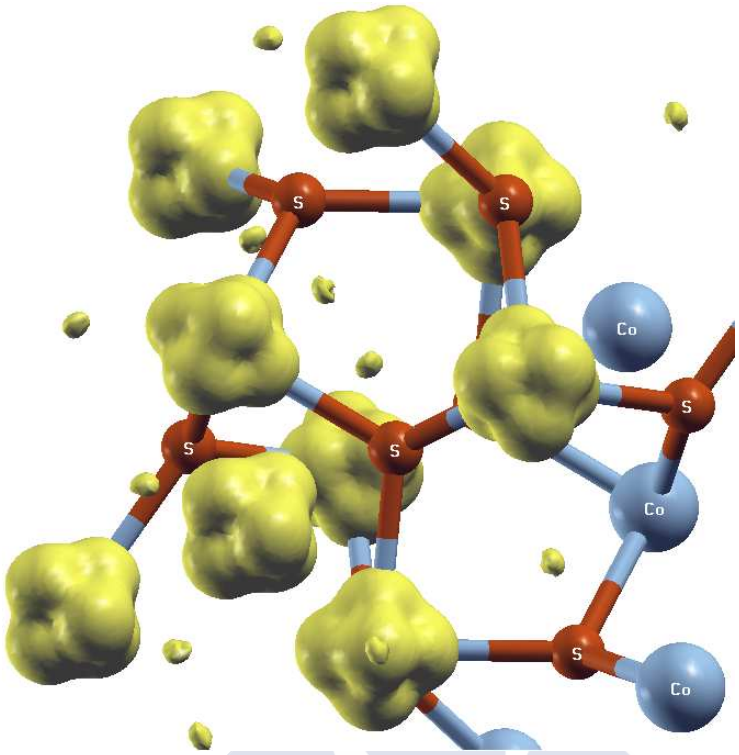

Figure 6.4:
Charge difference between the majority and minority states of CoS_2 compound. Large blue spheres represent Co atoms and orange small spheres represent S atoms. The charge difference plot corresponds to an isosurface at 0.05 e/Å^3 produced using XCrySDen.[47] The shape of the spin density isosurface represents the orbital that carries the spin moment, this being a mixture of e_g states.

in the ground state ferromagnetic solution, in agreement with the value of the saturation magnetization found experimentally, of about 0.9 μ_B/Co.[143] These data confirm the values obtained using different exchange-correlation potential approximations reported in previous publications.[130, 132, 133, 137, 139, 148] The moment comes from the partially filled majority e_g band. To illustrate this description of the electronic structure, we have produced a differential electron spin-density plot (Figure 6.4). This shows the difference in electronic density between the majority and minority states of the compound (yellow), in order to see the spatial distribution of the only unpaired electron (charge difference plot will show basically the density that corresponds to the $e_g^{\uparrow}$ electron, because the t_{2g} bands are completely

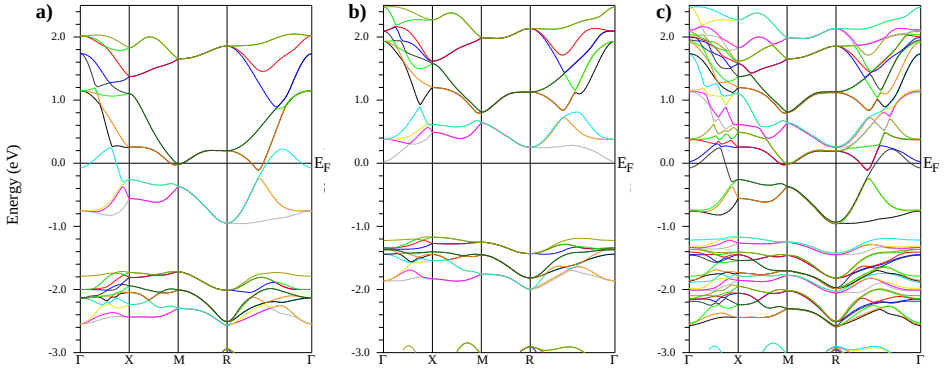

Figure 6.5:
Band structure plot of the: a) majority spin states, b) minority spin states and c) calculation including spin-orbit coupling with the magnetization along the 001 direction. Observe that the curvature of the bands remains unaltered when spin-orbit coupling is turned on. Fermi level is at zero energy. Values of Γ, X, M and R correspond to $(0,0,0), (0,\frac{1}{2},0), (\frac{1}{2},\frac{1}{2},0)$ and $(\frac{1}{2},\frac{1}{2},\frac{1}{2})$ respectively.

full). Charge accumulation can be seen along the Co-S direction (like $d_{3z^2-r^2}$ or $d_{x^2-y^2}$ in an octahedral environment). The large bandwidth of the e_g bands (about 2 eV), much higher than the crystal-field splitting between the e_g sub-levels, leads to a similar occupation of both e_g orbitals, as we see in Figure 6.4.

Our results show that a calculation at the GGA level is enough to capture the features of the electronic structure of this itinerant ferromagnet, as shown in a previous work.[143] The introduction of strong correlation effects by the LSDA+U method[28] does not provide more information about the electronic structure of this itinerant system, in agreement with the work of Kwon *et al.*[132] The correct ferromagnetic ground state is obtained at the GGA level (a FM solution is more stable by 75 meV/Co than the non-magnetic phase). A peak of the DOS at the Fermi energy (not shown) is found in a non-magnetic calculation, suggestive of the system being close to a ferromagnetic instability according to the Stoner criterion[149] ($N(E_F)I > 1$ to favor ferromagnetism).

Band structure plots (Figure 6.5a and b for the majority and minority spin channel, respectively) can be used to understand the essential features of the electronic structure of CoS_2. Being a half-metal, all the spectral weight around the Fermi level comes from the majority-spin channel (Figure 6.5a). The minority-spin channel (Figure 6.5b) shows a gap of about 1 eV at the Fermi level. A big electron

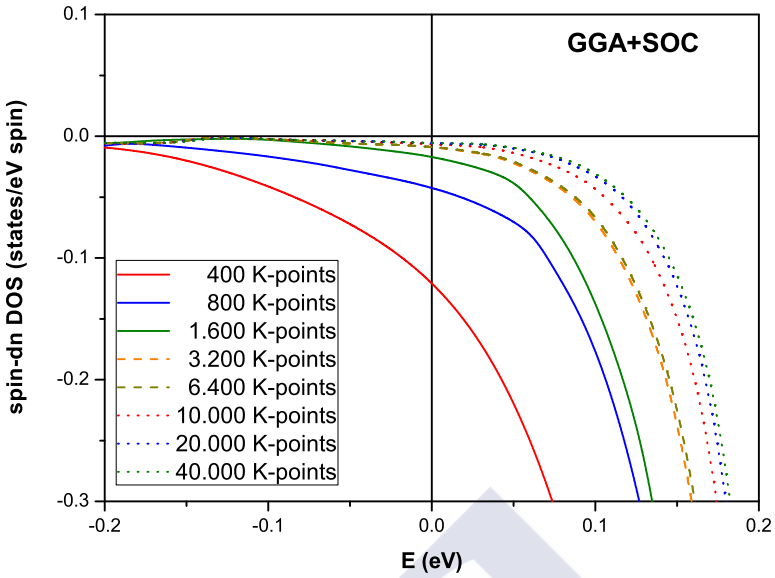

Figure 6.6:
Blow-up close to the E_F of the minority DOS of CoS_2 in a GGA+SOC (001) calculation at several values of k-mesh. Values of 40,000 total k-points are sufficient to achieve convergence. Fermi energy is at zero.

pocket, centered at the Γ point, and a large hole pocket appear in the Γ-R direction. Additional electron pockets appear near the M point. These results are similar to other band structure plots published using the GGA scheme,[133] except for the electron pocket centered at the Γ point, which is absent from their calculations (performed using a structure where the u parameter is 0.389) Instead, in the work of Wu *et al.*[135] where they used $u = 0.387$ (like this work), the band structure plot shows the same electron pocket at the Γ point too. Other band structure calculations done within LSDA show a similar behaviour in the majority spin channel, but with a shift of about 0.3 eV in the minority-spin channel around the Fermi level.[133, 139]

We have reported before that the SOC may introduce non-negligible minority states at the Fermi level, destroying the half-metallicity. This can be an important effect on the electronic structure of CoS_2. SOC contributes in a very small energy

window to the system, and because of this, the k-mesh required to calculate the properties of this material is not trivial. Thus, we have done a k-mesh test by calculating several DOS based on GGA+SOC with magnetization along the (001) direction. The main results are plotted in Figure 6.6. We have plot only the values of minority DOS near the Fermi energy, and it is clear that values of total k-points over 40,000 yield a converged DOS. It is also clear that a very fine mesh is required to study this kind of effects. We use higher k-mesh densities to analyze the electronic structure of CoS_2 including SOC effects.

The next step of the work consists in calculating the electronic structure including SOC, with the magnetization along the main directions of the cubic structure: (001), (110) and (111). Calculations yield an orbital magnetic moment $0.037\mu_B$ (quenched by the crystal field[150]), similar to other values reported.[132, 148, 151] Together with the local spin magnetic moment of $0.92\mu_B$ (inside the Co muffin-tin sphere) we obtain $M_l/M_s = 0.04$, i.e., $< l_z > / < s_z >= 0.08$, in good agreement with experimental measurements (0.1).[152]

A very small energy difference is obtained between the calculations with the magnetization along the three main directions of the crystal, suggesting a very small magnetocrystalline anisotropy in this largely isotropic material. The energy difference between the easy and hard axis is smaller than 50 μeV/Co atom.

Analyzing the band structure (Figure 6.5c) obtained from a GGA+SOC (001) calculation, we observe that the introduction of SOC leads to small shifts in the bands, but the positions of the pockets in the Brillouin zone and the curvature of the bands remain roughly unchanged (we see all the electron and hole pockets discussed above). A splitting in the bands corresponding to the electron pocket in the Γ-R direction, and a variation in the size of the other pockets can be seen. Below we discuss further the quantitative effects in the electronic structure caused by introducing SOC.

For a better description of the states near the Fermi level, Figure 6.7 shows the Fermi surface of the compound,[153] within a GGA+SOC-based calculation with the magnetization set along the (001) direction. In the plot we observe a large isotropic electron pocket around the Γ point. This feature was already predicted by Zhao *et al.*[130] using self-consistent linear combinations of atomic orbitals (LCAO)[154] to describe the Fermi surface in $k_x - k_y$ planes for various values of k_z. Experimentally, [143] the spin susceptibility of this compound can be understood in terms of spin fluctuation theory.[155] For this type of systems, peaks in the spin susceptibility

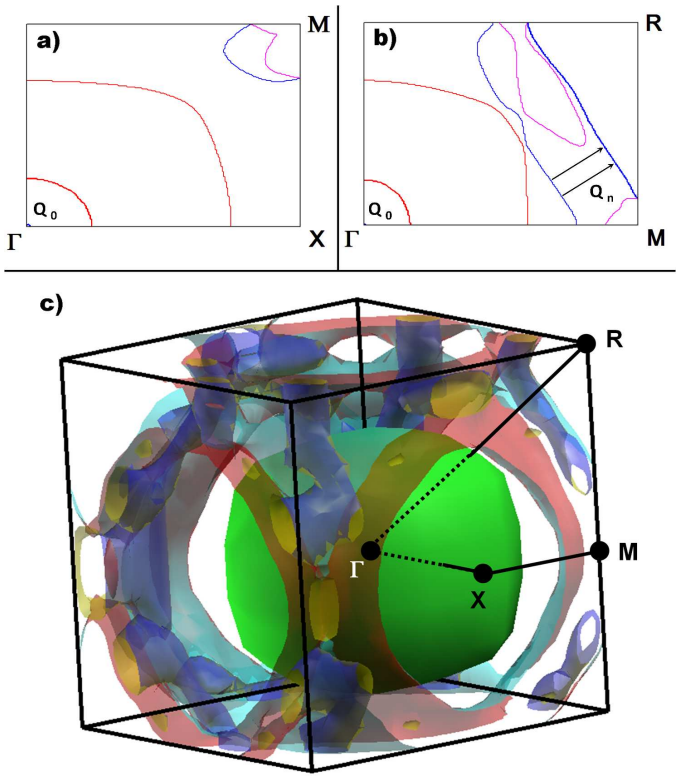

Figure 6.7:
Fermi surface of CoS_2 obtained for the majority spin channel in a FM solution, within a GGA+SOC-based calculation along the (001) direction. a) and b) show the 2-dimensional Fermi surface in the Γ-X-M and Γ-M-R planes, respectively. c) shows the 3-dimensional Fermi surface. In the inset b) we have denoted the nesting vector as Q_n (which corresponds to a wavelength of approximately 6 times the lattice parameter). This would lead to a peak in the spin susceptibility associated with that wave-vector, together with the ferromagnetic ones.

can be associated to nesting features in the Fermi surface. In the case of CoS_2, some nesting features can be observed in the $\Gamma - M - R$ plane (Figure 6.7 b), with a nesting vector that we have denoted as Q_n. The magnitude of Q_n would correspond to long-wavelength spin fluctuations, ($\lambda = 6a$, with a being the lattice parameter), and are believed to have key importance in governing the magnetic properties of weak ferromagnets such as CoS_2[143] and also MnSi,[156] together with many other systems.[155] The rest of the Fermi surface, i.e. the hole pocket along the Γ-R direction and the small electron pockets in the X-M direction near M,

are largely incoherent and will lead to negligible nesting. Electrons perform open orbits within this Fermi surface, and this has implications for the Lorentz-force-type magneto-resistance,[31] as we will discuss below.

6.4.2 Half-metallicity

CoS_2 has been predicted to be a good source of spin-polarized electrons;[137] hence, we will try to address this point with our calculations. GGA alone leads to a half-metallic behavior. Due to the proximity of the conduction band edge to the Fermi level in the minority spin channel, SOC destroys the half-metallicity, as we can see in Figure 6.8. No minority DOS is seen in the GGA calculation, but magnifying the minority DOS of the calculation including SOC (in the inset), we see the DOS is non-zero at the Fermi level for the minority-spin channel. This has important consequences for the conduction properties of the material. We can compare the values of the DOS at the Fermi level for the two spin channels, being no longer infinite but $N(E_F)_\uparrow/N(E_F)_\downarrow = 540$ when SOC is obtained, giving a polarization of the DOS at the Fermi level $P = [N_\uparrow(E_F) - N_\downarrow(E_F)]/[N_\uparrow(E_F) + N_\downarrow(E_F)]$ of 99.6%, very large still.

For analyzing further the degree of spin polarization of the carriers in this system, we have calculated the transport properties from our band structure calculations using a semiclassical approach based on Boltzmann transport theory.[30] In order to understand the spin polarization of the carriers, it is necessary to go beyond the values of the DOS at the Fermi level. One possible way is to compare the conductivities of both spin channels. The inset of Figure 6.9 shows the temperature dependence of the ratio between the subtraction and the sum of the conductivities coming from both spin channels, i.e. $P_\sigma = (\sigma_{up} - \sigma_{dn})/(\sigma_{up} + \sigma_{dn})$, defined analogously to that of the DOS. This quantity ranges from ± 1 for a full-polarization to 0 for no polarization and will give us the spin polarization of the carriers at a given temperature. When no SOC is considered and polarization of the DOS is infinite, it is still very large in terms of the conductivities (spin polarization of the carriers), being approximately $P_\sigma = 0.998$ at room temperature.

One would naively expect that the introduction of SOC leads to a substantially larger conductivity coming from the minority spin channel compared to the case without SOC, because of the non-zero DOS at the Fermi level. To gain some insight on that, we present in Figure 6.9 the temperature dependence of the calculated

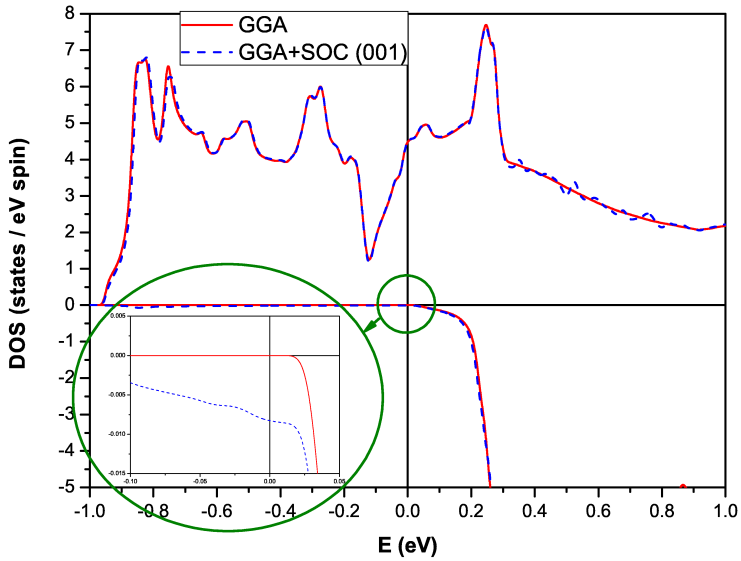

Figure 6.8:
Spin-up (positive values) and spin-down (negative values) total DOS plots for the CoS_2 in the ferromagnetic configuration within GGA (solid red line) and GGA+SOC (SOC along (001) direction) (dashed blue line). Fermi energy is at zero. The system is half-metallic in the GGA approximation and becomes metallic in the GGA+SOC approximation. The inset shows a zoom of the minority DOS near the Fermi level of both solutions (GGA and GGA+SOC).

ratio between the subtraction and the addition of the conductivities calculated with and without SOC: $P_{SOC} = (\sigma_{nosoc} - \sigma_{soc})/(\sigma_{nosoc} + \sigma_{soc})$. We observe that the solution without SOC has a larger conductivity than the one including SOC up to room temperature, both values differing by about a few percent. Thus, the bigger change in the conductivity when introducing SOC in the calculations is not the additional contribution from the minority spin states, but an overall reduction in the conductivity. Even though a separation in conductivity from both spin channels is not possible when calculating with SOC, the results suggest a very large polarization of the carriers will still be present when the calculations include SOC. This effect will account for a reduction in the half-metallicity of just a few percent. However, to understand the experimental observations, one needs to consider other effects as possible sources against a full spin polarization, such as defects, spin excitations or non-quasiparticle states[157, 158] to be important.

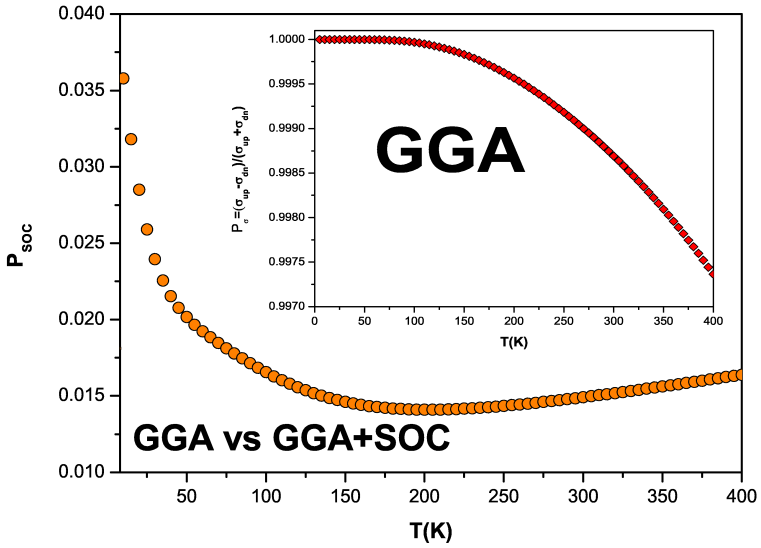

Figure 6.9:
Percentage (P_{SOC})of the better conduction of GGA versus GGA+SOC calculations. This is calculated by subtraction of the conductivities coming from GGA and GGA+SOC calculations, normalized to the sum of both them (solid orange circles) ($P_{SOC}= (\sigma_{nosoc} - \sigma_{soc})/(\sigma_{nosoc} + \sigma_{soc})$). GGA alone leads better conduction properties, so the GGA+SOC implies larger resistivity. The inset shows the subtraction of the conductivities coming from both spin channels over the sum of these conductivities within the GGA approximation (solid red diamonds). At room temperature, σ_{up} contributes in a 99.8 % and σ_{dn} contributes 0.2 % to the total conductivity in the GGA approximation, half-metallicity is almost complete.

In a material with such a large polarization of carriers at the Fermi level, a negative magnetoresistance is expected to occur in the FM region of the phase diagram. The work of Wang *et al.*[137] shows the measurements of the magnetoresistance (MR) in an external magnetic field of 17 T. These show a negative MR in a temperature range within the FM phase (below the Curie temperature $T_c = 122K$[143]) with a value about -12%. At low temperatures, a large positive value of the MR is observed. Figure 6.10 shows the measurements of MR (carried out by F. Rivadulla) in an external magnetic field of 9 T, defining $MR = 100(\rho_{9T} - \rho_{0T})/\rho_{0T})$. The data confirm the previous observations of a negative MR in a temperature range within the FM phase with a value ranging between -3% and -9%. These are related to the non-closed orbits we analyzed previously in the Fermi surface. This causes the positive magnetoresistance to grow with field, as it is observed experimentally.[159]

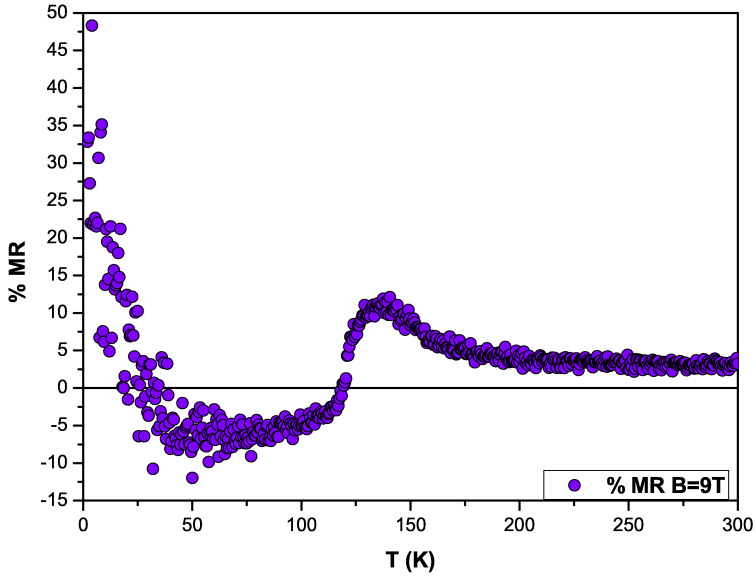

Figure 6.10:
Evolution of the magnetoresistance with temperature measured comparing the values of resistivity at $H = 9T$ and $H = 0T$ applied magnetic field according to the formula MR=$100(\rho_{9T} - \rho_{0T})/\rho_{0T}$. Below 25K we observed positive MR, and negative MR are obtained in the rest of FM phase.

This behavior is opposed to the case of closed orbits, where the high-field magnetoresistance should approach a constant value.[31] This observation further confirms the validity of our Fermi surface calculations, that is able to describe correctly the electronic structure of CoS_2. Above the Curie point, in the paramagnetic phase, the MR becomes again positive, approaching a constant value of about 3% at high temperatures. The picture is the same in a lower applied field. Negative MR does not reach a very high value, consistent with the fact that spin polarization of the carriers is not complete, as discussed above.

6.5 Summary

We have analyzed the electronic structure and magnetic properties of this itinerant weak ferromagnet, dominated by spin-density fluctuations. We have related them to the nesting features in the Fermi surface associated to long-wavelength

nesting vectors. They have been shown to dominate the thermodynamics of this compound and other related weak ferromagnets, and to have an origin in the electronic structure and, in particular, in the peculiar properties of its Fermi surface, that our calculations accurately describe. Calculations without SOC predict CoS_2 to be half-metallic, but when introducing the important SOC effects, the results of the calculations show SOC destroys the half-metallicity, non-zero occupation (band-crossing) of the minority channel at the Fermi level appears. However, our transport properties calculations show that changes in the conductivity associated to the introduction of SOC in the calculations (or other small perturbation of the states near E_F, like an external magnetic field) do not imply a significant break-up of the half-metallic behavior, but just of a few percent. These results are consistent with the experimental observation of a negative magnetoresistance in the material. Our Fermi surface plots are also consistent with the large positive magnetoresistance at low T, not saturating with increasing field, because electrons can perform open orbits in k-space along the Fermi surface.

A

List of Publications

1.- V. Pardo, P. M. Botta, D. Baldomir, J. Rivas, **A. Piñeiro**, C. de la Calle, J. A. Alonso and J. E. Arias, *PHYSICA B* 403, 1636-1638 (2008).

2.- D. Baldomir, V. Pardo, S. Blanco-Canosa, F. Rivadulla, J. Rivas, **A. Piñeiro** and J. E. Arias, *PHYSICA B* 403, 1639-1641 (2008).

3.- M. Otero-Leal, F. Rivadulla, M. García-Hernández, **A. Piñeiro**, V. Pardo, D. Baldomir and J. Rivas, *PHYSICAL REVIEW B* 78, 180415-1–180415-4 (2008).

4.- D. Baldomir, V. Pardo, S. Blanco-Canosa, F. Rivadulla, D. I. Khomskii, Hua-Wu, **A. Piñeiro**, J. E. Arias and J. Rivas, *JOURNAL OF MAGNETISM AND MAGNETIC MATERIALS* 321, 679-681 (2009).

5.- S. Blanco-Canosa, F. Rivadulla, **A. Piñeiro**, V. Pardo, D. Baldomir, D. I. Khomskii, M. M. Abd-Elmeguid, M. A. López-Quintela and J. Rivas, *PHYSICAL REVIEW LETTERS* 102, 056406-1–056406-4 (2009).

6.- F. Rivadulla, M. Bañobre-López, C. X. Quintela, **A. Piñeiro**, V. Pardo, D. Baldomir, M. A. López-Quintela, J. Rivas, C. A. Ramos, H. Salva, J.- S. Zhou and J. B. Goodenough, *NATURE MATERIALS* 8, 974-951 (2009).

7.- S. Blanco-Canosa, F. Rivadulla, **A. Piñeiro**, V. Pardo, D. Baldomir, M. A. López-Quintela and J. Rivas, *JOURNAL OF MAGNETISM AND MAGNETIC MATERIALS* 322, 1069-1071 (2010).

8.- **A. Piñeiro**, V. Pardo, D. Baldomir, S. Blanco-Canosa, F. Rivadulla, J. E. Arias and J. Rivas, *JOURNAL OF MAGNETISM AND MAGNETIC MATERIALS* 322, 1072-1075 (2010).

9.- **A. Piñeiro**, V. Pardo, D. Baldomir, F. Rivadulla, A. Rodríguez, A. Gómez, J. E. Arias and J. Rivas, *PHYSICA STATUS SOLIDI (C)* 7, 2620-2623 (2010).

10.- **A. Piñeiro**, A. S. Botana, V. Pardo and D. Baldomir, *JOURNAL OF PHYSICS-CONDENSED MATTER* 22, 505602-505607 (2010).

11.- A. S. Botana, P. M. Botta, C. de la Calle, **A. Piñeiro**, V. Pardo, J. Botana, M. Pereiro, D. Baldomir, J. A. Alonso and J. E. Arias, *JOURNAL OF APPLIED PHYSICS* 109, 07E114-1–07E114-3 (2011).

12.- **A. Piñeiro**, A. S. Botana, V. Pardo, J. Botana, M. Pereiro, D. Baldomir and J. E. Arias, *JOURNAL OF APPLIED PHYSICS* 109, 07E158-1–07E158-3 (2011).

13.- A. S. Botana, P. M. Botta, C. de la Calle, **A. Piñeiro**, V. Pardo, D. Baldomir and J. A. Alonso, *JOURNAL OF PHYSICS-CONDENSED MATTER* 24, 275503-275510 (2012).

14.- **A. Piñeiro**, V. Pardo, D. Baldomir, A. Rodríguez, R. Cortés-Gil, A. Gómez and J. E. Arias, *JOURNAL OF PHYSICS-CONDENSED MATTER* 24, 275503-275510 (2012).

B

Resumen de la presente Tesis Doctoral

En la presente Tesis Doctoral, se recoge el trabajo de investigación realizado por el doctorando Alberto Piñeiro Rodríguez durante su etapa de postgrado. En líneas generales el trabajo consistió en el estudio de las propiedades estructurales, eléctricas y magnéticas de diferentes sistemas próximos a una transición metal-aislante, compuestos por metales de transición.

El propósito de la ciencia, y en particular de la física, es tratar de encontrar respuestas a las preguntas que el ser humano se hace sobre la realidad que lo rodea. A lo largo de los siglos se han resuelto muchos misterios, que a su vez daban lugar a una ingente cantidad de nuevas preguntas. Además, cada nuevo paso que da la ciencia produce una gran influencia en la sociedad, incluso los descubrimientos más pequeños. Este es el motivo que hace que muchos jóvenes estudiantes quieran estudiar una licenciatura en ciencias, o incluso continuar posteriormente con una carrera investigadora: descubrir algo nuevo.

La ciencia de materiales estudia compuestos con potenciales aplicaciones tecnológicas, y su principal objetivo es encontrar el material adecuado para cumplir una determinada función en la industria. Hasta hace relativamente poco, este trabajo se realizaba a través de la medición experimental de las propiedades físicas de estos materiales, aunque también es cierto que estas tomas de datos estaban acompañadas por el desarrollo teórico de fórmulas para descubrir sus principales propiedades. El mayor inconveniente radicaba en que no se podían aplicar los modelos teóricos (analíticos) a determinados problemas, como el de los muchos cuerpos (es bien sabido que el problema de los tres cuerpos no se puede resolver

analíticamente). A principios del siglo XX aparecen algunos modelos que simplifican el problema de los muchos cuerpos, y se desarrollan varias teorías que reducen enormemente la complejidad de este problema. Pero hasta que se diseñaron los primeros ordenadores, estos modelos no se pudieron testear. Hoy en día, las prestaciones de los modernos supercomputadores, unido a la precisión que han alcanzado los métodos y programas que se utilizan, hacen posible el estudio de una amplia gama de materiales en situaciones muy diferentes. Este hecho hace que podamos soñar con la posibilidad de conseguir alcanzar el diseño computacional de materiales en un futuro no muy lejano.

El objeto del estudio de esta Tesis son materiales con presencia de metales de transición, dotados de electrones fuertemente correlacionados. Estos materiales presentan propiedades electrónicas y magnéticas inusuales: transiciones metal-aislante, medio-metalicidad, separación de fases, etc. El comportamiento de sus electrones no se puede describir de manera efectiva en términos de partículas no-interactuantes: hay que tener en cuenta las fuertes interacciones entre ellos. Las aplicaciones tecnológicas de este tipo de compuestos son muy importantes, como en el caso de los memristores, ventanas inteligentes, sensores ópticos y magnéticos, cabezales de lectura-escritura de discos duros, etc.

Este trabajo se realizó usando técnicas *ab initio*, es decir, empleando técnicas de primeros principios. Esto se traduce en la resolución de la ecuación de Schrödinger no relativista para un sistema formado por muchos electrones. Nuestra aproximación a un problema tan complejo consiste en el uso de la Teoría del Funcional de la Densidad (DFT), que convierte el problema de muchos cuerpos, considerando cada electrón interactuando con todos los demás electrones, en un problema de un único cuerpo, en el que cada electrón interactúa únicamente con un potencial efectivo creado por la densidad electrónica. La implementación de esta aproximación se realizó principalmente con el programa WIEN2k, hoy en día utilizado por casi 2000 grupos de investigación y empresas en todo el mundo.

A continuación detallaremos los aspectos más importantes de los materiales estudiados.

B.1 Efectos de la presión en sistema electrónico unidimensional: TiOCl

El TiOCl es un aislante de Mott a temperatura ambiente, con cationes Ti^{3+} en una configuración $3d^1$. Este material sufre una transición de espín-Peierls a baja temperatura provocada por la fuerte unidimensionalidad del compuesto (de carácter puramente electrónico, ya que su estructura es altamente bidimensional). Una transición de espín-Peierls corresponde a la dimerización de una cadena antiferromagnética unidimensional de espines $S = 1/2$ acoplada a un medio elástico tridimensional. El compuesto TiOCl recientemente ha emergido como un material antiferromagnético unidimensional, y como segundo ejemplo de un compuesto inorgánico con transición de espín-Peierls (el primero en ser observado fue $CuGeO_3$).

Por otro lado, se ha observado una fuerte supresión de la transmitancia y un aumento brusco de la reflectancia en el infrarrojo cercano por encima de aproximadamente 10 GPa en el TiOCl. Estos efectos fueron interpretados como una metalización inducida por presión de la cadena unidimensional, pero en estas mediciones no se observa la presencia de un pico de Drude (que debe estar presente en una transición metal-aislante cuando se alcanza metalicidad). Una fuerte supresión del gap electrónico aproximadamente a 12 GPa fue confirmada directamente a través de medidas de resistividad a alta presión, aunque el comportamiento semiconductor a presiones altas se sigue manteniendo, con un valor del gap de 0.3 eV aproximadamente.

Nosotros hemos estudiado, a partir de cálculos *ab initio*, la evolución con la presión de la estructura electrónica y química del TiOCl, para corroborar su naturaleza electrónica cuasi-unidimensional (cuyo carácter además aumenta con la presión) y además estudiar la evolución de las temperaturas de transición en función de la presión. Para demostrar que la transición estructural desde la fase ortorrómbica a baja presión a la fase monoclínica dimerizada a alta presión es probablemente más compleja de lo que se creía, hemos realizado relajaciones estructurales de la estructura y calculado su estado fundamental. Los resultados obtenidos arrojan la existencia de una transición estructural a alta presión en TiOCl, en la que la dimerización Ti^{3+}-Ti^{3+} a lo largo del eje b es más estable. Se han caracterizado las propiedades estructurales y físicas de la fase de alta presión, donde la dimerización Ti^{3+}-Ti^{3+} es más fuerte (es decir, hay una diferencia mucho más grande entre las distancias largas y cortas entre los átomos de Ti) que en la fase de la presión

ambiente. Hemos analizado la estructura electrónica cuasi-unidimensional del TiOCl y también la fuerte unidimensionalidad de las propiedades magnéticas. Los iones Ti^{3+} (d^1) tienen un orbital t_{2g} ocupado (d_{yz}) con un valor alto de la integral de hopping a lo largo de la dirección b del cristal. Nuestros cálculos predicen una transición de fase a alta presión (sobre 10 GPa) hacia un estado dimerizado a temperatura ambiente, de acuerdo con los experimentos. Alrededor de presiones de 15 GPa, una reconstrucción dramática de la estructura electrónica es impulsada por la proximidad al límite de electrones itinerantes en los enlaces Ti-Ti cortos, lo que sugiere un mecanismo totalmente diferente para la dimerización a alta presión. En ese rango de presiones, la transición debe ser tratada no como una espín-Peierls, sino más bien como una transición de Peierls.

B.2 Efectos de la presión en espinelas dimerizadas y no dimerizadas

Tras estudiar que el compuesto TiOCl se aproxima a una transición metal-aislante mediante la aplicación de presión, a continuación analizamos otro tipo de compuestos, no unidimensionales, que también se acercan a una transición metal-aislante mediante la aplicación de presión: las espinelas de vanadio ZnV_2O_4 y MgV_2O_4. Al igual que el TiOCl, su estructura electrónica conduce a una transición de Peierls inesperada en estructuras tridimensionales, especialmente una estructura casi cúbica como la espinela.

Las espinelas tienen fórmula química AV_2O_4, donde A es un catión que puede ser, entre otros, Cd, Mn, Zn o Mg (en nuestro caso estudiamos Zn y Mg), y los átomos de V forman una red de pirocloro (que da lugar a frustración magnética). El hecho de que el sitio A sea no magnético simplifica la interpretación de la estructura magnética de los compuestos en términos de interaciones V-V directas. Estas series de espinelas se acercan a una transición aislante-metal de tipo Mott cuando la distancia entre los cationes de V se reduce lo suficiente, bien aplicando presión mecánica o variando el tamaño del catión A^{+2}. De hecho, el ZnV_2O_4 es el miembro de la serie que se acerca más a un estado metálico, desde el límite localizado.

El estado fundamental de las espinelas de vanadio ha producido una intensa investigación teórica en los últimos años, especialmente a causa de la frustración

magnética en la red de pirocloro. Nuestros cálculos predicen que debido a la proximidad de las espinelas a la frontera de los electrones itinerantes, se produce una dimerización a lo largo de las cadenas de V-V, que se caracteriza por una delocalización electrónica. Este modelo explica fácilmente el orden magnético observado fuera del plano ($\uparrow\uparrow\downarrow\downarrow$) y la aparición de polarización electrónica, ambas como consecuencia directa de una leve distorsión estructural.

En nuestro análisis de los efectos de aplicar presión en la estructura dimerizada del ZnV_2O_4, analizamos la importancia de la distorsión estructural para dificultar el paso a metal inducido por presión. En primer lugar, demostramos que una optimización de la estructura realizada para el ZnV_2O_4 incluyendo fuertes efectos de correlación confirma que la estructura del material cerca del límite de electrones itinerantes, donde U/W es pequeño, se distorsiona por debajo de la simple simetría tetragonal. Dicha reducción de la simetría permite diferentes distancias V-V a lo largo de las direcciones [011] y [101]. La proximidad a la transición provoca la formación de orbitales moleculares V-V en una matriz iónica. Tal distorsión explica la estructura magnética del material que se observa experimentalmente de un modo natural, y además daría lugar a una polarización eléctrica por debajo de la temperatura de ordenamiento magnético.

En segundo lugar, estudiamos los efectos de aplicar presión en el compuesto en el caso de la estructura dimerizada, y observamos un comportamiento aislante tipo Mott-Hubbard a alta presión. La dimerización de las cadenas V-V en la estructura de espinela, producidos por la proximidad de una transición metal-aislante, evita que el sistema alcance un estado totalmente metálico. La aparición de un gap adicional de tipo Peierls retiene al sistema en el lado aislante de la transición, en concordancia con los resultados experimentales. Este hecho contrasta con el caso no dimerizado, que también se estudió en la tesis, centrándonos en el MgV_2O_4. De no producirse la dimerización, y si las distancias V-V se hacen suficientemente pequeñas (por debajo de 2,94 Å), se alcanzaría la itinerancia. Calculamos además el poder termoeléctrico de la espinela dimerizada (ZnV_2O_4), y lo comparamos con medidas experimentales. El coeficiente Seebeck calculado para la estructura dimerizada muestra un comportamiento lineal (no activado), y encaja muy bien con las mediciones experimentales, lo que proporciona un apoyo adicional a nuestra descripción de las distorsiones de red que se producen en el ZnV_2O_4 cerca del estado metálico.

B.3 Cambios mecánicos derivados de transferencia de carga en transiciones de fase en el compuesto CrN

Hasta ahora hemos visto cómo al aproximarse a una transición metal-aislante la naturaleza del enlace cambia, por ejemplo, deslocalizándose carga en enlaces homopolares como en el caso del ZnV_2O_4. Lo que haremos a continuación es estudiar las consecuencias de los cambios en el enlace cerca de la transición, observando que no sólo se producen cambios en las propiedades eléctricas del compuesto, sino también cambios drásticos en las propiedades mecánicas.

CrN es un material que se ablanda dramáticamente en la fase antiferromagnética *Pnma* a baja temperatura o alta presión. Tal reblandecimiento está relacionado con un cambio en la naturaleza misma del enlace, como se ha demostrado en la tesis mediante un análisis de la transferencia de carga entre el enlace Cr-N más covalente (que normalmente es mecánicamente duro) hacia el enlace directo Cr-Cr iónico (más blando). Estos efectos se presentan en el CrN debido a la proximidad con el límite de electrones itinerantes. En este caso, tienen lugar fluctuaciones de la distancia de enlace, y en el caso del CrN el resultado de ello es la transferencia de carga que se observa. Lo que encontramos en el trabajo realizado sobre este material es una reducción drástica en el módulo de bulk, sobre un 25%, en el compuesto CrN por encima de presiones en torno a 1 GPa. Nuestros cálculos *ab initio* demuestran que este ablandamiento anómalo tiene su origen en un efecto puramente electrónico.

Como resultado de este trabajo, pueden surgir importantes implicaciones tecnológicas. Para poder usar el alto módulo de bulk del material, y por lo tanto usar sus interesantes propiedades mecánicas, se necesita prevenir la transición de fase AF. Esto se puede hacer haciendo crecer el CrN en un film (lo que es bueno para revestimientos y otras aplicaciones), sobre un sustrato adecuado para que la tensión en el plano evite que el sistema tenga una transición estructural/magnética, y mantener así las propiedades mecánicas de la fase cúbica paramagnética.

Asimismo, este trabajo muestra la estrecha relación entre el conocimiento básico (la propia naturaleza del enlace químico) y las aplicaciones industriales de vanguardia.

B.4 Separación de fases en $La_{1-x}Ca_xMnO_3$ a través de inhomogeneidades de dopado en la nanoescala

Para continuar con el estudio de la fenomenología cerca de una transición metal-aislante, estudiamos también uno de los sistemas más investigados, las manganitas, cuyo diagrama de fases incluye varias transiciones metal-aislante. En esta parte analizamos las consecuencias sobre su estructura electrónica al inducir una transición metal-aislante a través del dopaje, centrándonos en la separación de fases que ocurre en el límite entre localizado e itinerante.

Las manganitas pertenecen a una clase de materiales que se han vuelto cada vez más importantes en los últimos años, especialmente debido a la gran variedad de fenómenos que presentan, estrechamente ligados a la naturaleza de sus electrones fuertemente correlacionados. La serie de manganitas $A_{1-x}B_xMnO_3$ (donde A^{3+} es un lantánido y B^{2+} es un alcalino-térreo) es una de las familias que han sido estudiadas más intensamente. El interés por estos materiales creció rápidamente después del descubrimiento de la magnetorresistencia colosal (CMR), una alta magnetorresistencia negativa que tiene lugar al aplicar un campo magnético, pero también ha surgido un intenso debate debido a inusuales propiedades tales como la separación de fases, ordenamiento de carga y orbital, y también por sus posibles aplicaciones en distintos dispositivos como válvulas de espín, etc, derivado de sus propiedades de estructura electrónica.

El caso de A= La^{3+} y B=Ca^{2+} se ha convertido en un sistema prototipo de manganitas, que presenta un rico diagrama de fases (en función de la concentración de Ca y la temperatura). Las regiones en el diagrama de fase con concentraciones de Ca muy cerca al 18 % y el 50 % se han estudiado a fondo, ya que a estos niveles de dopado aparece el fenómeno de separación de fases.

Experimentalmente, la separación de fases magnética se ha observado en la forma de fases en la nanoescala con diferentes propiedades magnéticas, es decir, regiones en el cristal de tamaño nanométrico que presentan un ordenamiento magnético diferente entre sí. Recientemente se ha puesto de manifiesto la estrecha relación existente entre las regiones en separación de fase en la nanoescala con un origen electrónico/magnético y la CMR. Estas regiones, en el rango de varios nm, no

tendrían un origen químico. Sin embargo, el papel de las inhomogeneidades químicas de tamaño nanométrico nunca ha sido plenamente estudiado.

Para profundizar en este problema, se han tenido en cuenta una estructura con dopajes de Ca^{2+} cercanos a $x \sim$0,2 (exactamente $x = 0,1875$) en $La_{1-x}Ca_xMnO_3$, y se ha procedido a realizar cálculos *ab initio* con ella. Normalmente este tipo de análisis no se realiza debido al enorme tamaño de las superceldas que se deben construir para simular este tipo de compuestos, pero nos ayudarán a entender los orígenes electrónicos y químicos de la separación de fases, o al menos el rol que pueden desempeñar las inhomogeneidades químicas en las propiedades de un sistema que presenta separación de fases. Así pues, construimos varias superestructuras en diferentes configuraciones magnéticas para explorar el origen magnético de la separación de fases. A partir de las simulaciones, encontramos que en el caso de un estado de distribución homogénea de los dopantes, la configuración FM resulta ser el estado fundamental de la estructura. Partiendo de este resultado, se analiza la influencia de una distribución no homogénea del catión dopante Ca^{2+} en este estado fundamental. Para ello, se varían las posiciones del Ca desde una distribución aleatoria homogénea a otras configuraciones más correlacionadas. Este escenario resulta importante explorarlo, ya que en otros compuestos se ha encontrado que el estudio de inhomogeneidades químicas en la escala nanométrica (como en el caso del superconductor $(Ba_{1-x}K_x)Fe_2As_2$) da lugar a un escenario de coexistencia y separación de fases.

Para completar el trabajo, hacemos un análisis similar a una concentración de dopado muy diferente de la estudiada con anterioridad, que será x =0,375, en la que el estado fundamental es FM metálico, y donde no existe un entorno próximo de posibles transiciones de fase. Las inhomogeneidades químicas están presentes también, pero sin dar lugar a regiones con propiedades electrónicas diferentes, debido a su lejanía de la transición metal-aislante.

Todos los resultados que hemos encontrado muestran evidencias importantes acerca de un factor a menudo olvidado (principalmente debido a las complicaciones para su cálculo directo) en el estudio del origen de la separación de fases electrónicas y magnéticas cerca de una transición de fase magnética. Hemos observado, por medio de cálculos *ab initio*, que el magnetismo no es el único factor a tener en cuenta en el fenómeno de la separación de fases. Hemos estudiado fases magnéticas mixtas, sin encontrar el estado fundamental en ninguna de ellas. Sin embargo, la aparición de inhomogeneidades químicas causadas por desorden catiónico en una

escala menor que 1 nm, son estables en el sistema, de acuerdo con nuestros cálculos de energía. Al introducir el dopaje químico en la red de forma no homogénea se producen distorsiones locales y una interacción de largo alcance entre los iones, que será atractiva o repulsiva dependiendo de la dirección. Así, las distorsiones de red cooperativas son fundamentales para la propagación a larga distancia de este efecto. La interacción entre los iones de distinto tamaño, La^{3+} y Ca^{2+}, da como resultado una distribución no homogénea del dopante, con el fin de cumplir con el requisito de reducir la energía elástica de la red. Cerca de una transición de fase FM/AF, estas inhomogeneidades en el dopaje en la nanoescala son lo suficientemente grandes como para conducir al sistema a un estado de fases separadas, dando lugar a regiones ricas/pobres en huecos alternadas en el compuesto en la escala nanométrica. Las inhomogeneidades químicas en esta escala siempre estarán presentes en el sistema, ya sea provocando en el sistema una separación de fases electrónica/magnética o acompañándola. Si se presenta la separación de fases en la misma escala nanométrica, se espera que las inhomogeneidades químicas desempeñen un papel importante como atractores de carga y centros de nucleación para una fase magnética/electrónica determinada a nivel local. Esto no sería el caso para una separación de fases en la escala micrómetrica, ya que en ese caso el efecto de las inhomogeneidades estudiadas en este trabajo sería insignificante.

B.5 Estructura electrónica y magnetismo en el compuesto ferromagnético itinerante débil CoS_2

Para finalizar nuestro recorrido, terminamos analizando los resultados de un sistema itinerante, uno peculiar, tanto porque uno de los canales de espín presenta una gap (lo que se conoce como un medio-metal) como porque su itinerancia se produce con la presencia de fluctuaciones de espín (denominado material ferromagnético itinerante débil). Vamos a ver cómo se pueden entender sus propiedades físicas particulares con la ayuda de cálculos *ab initio*.

Los medio-metales son materiales en los que la conducción se produce sólo a través de uno de los canales de espín, dando lugar a una corriente de electrones con polarización de espín perfecta. En ellos, uno de los canales de espín presenta un gap en la energía de Fermi, mientras que el otro canal tiene bandas que lo cruzan.

Esto los convierte en una interesante familia de materiales, particularmente para aplicaciones en el campo de la espintrónica.

En los últimos años se han realizado varios cálculos basados en DFT de la estructura electrónica del CoS_2, que describen el material como un ferromagnético medio-metálico. Sin embargo, sus propiedades eléctricas y magnéticas no se entienden completamente todavía. Medidas de reflexión por puntos de contacto Andreev muestran un nivel relativamente bajo de polarización de espín, del 56% a una temperatura de 4.2 K. Este hecho fue confirmado mediante estudios en la serie $Co_{1-x}Fe_xS_2$, donde se encuentran valores de polarización de espín que varían en el rango de $-56\% < P < 85\%$ y $-75\% < P < 100\%$, según las fuentes. Recientemente, el valor de la polarización se ha calculado como P=-72% para el CoS_2. Se ha encontrado también a partir de medidas de difracción de neutrones que la medio-metalicidad no tiene lugar en la fase ferromagnética.

Recientemente se ha descubierto que la resistividad, el calor específico y la susceptibilidad magnética del CoS_2 están dominados por fluctuaciones de la densidad de espín. También se ha demostrado que el método GGA es suficiente para describir el comportamiento electrónico y magnético del CoS_2, debido a la naturaleza no localizada del compuesto. La introducción de los efectos de alta correlación no es necesario para describir con precisión sus propiedades de estructura electrónica. Por lo general, el acoplamiento espín-órbita (AEO) introduce estados en el canal minoritario que no son despreciables en el nivel de Fermi, lo que produce la destrucción de la medio-metalicidad. Muchos trabajos basan sus estudios únicamente en los cambios de la densidad de estados en el nivel de Fermi, pero el grado de medio-metalicidad estará influenciada por los cambios en las propiedades de conducción que se derivan de la reordenación de los estados alrededor del nivel de Fermi introducidos por el AEO. Además, la conductividad del canal de espín minoritario tendrá un componente activo que debe ser cuantificado más allá del valor de la densidad de estados en el nivel de Fermi.

En este apartado de la tesis, hemos analizado la estructura electrónica y propiedades magnéticas de este material ferromagnético débil itinerante (CoS_2), dominadas por las fluctuaciones de densidad de espín. Lo hemos relacionado con las características de anidación en la superficie de Fermi, asociadas a vectores de anidación de longitud de onda larga. Se ha demostrado que estos dominan la termodinámica de este compuesto y otros ferromagnetos débiles relacionados, basados en las propiedades peculiares de su superficie de Fermi, que nuestros cálculos describen con exactitud.

Los cálculos sin AEO predicen que el CoS_2 es medio-metálico, pero al introducir los importantes efectos del AEO, los resultados de los cálculos muestran que se destruye la medio-metalicidad, con ocupaciones distintas de cero en el canal minoritario en el nivel de Fermi (con bandas cruzándolo). Sin embargo, nuestros cálculos de las propiedades de transporte del compuesto muestran que los cambios en la conductividad asociada a la introducción del AEO (u otras perturbaciones pequeñas de los estados cerca del nivel de Fermi, como puede ser un campo magnético externo) no implican una ruptura significativa del comportamiento medio-metálico, sino sólo variaciones en pequeños porcentajes. Estos resultados son consistentes con la observación experimental de una magnetorresistencia negativa en el material. Nuestras representaciones de la superficie de Fermi también son consistentes con la aparición de una magnetorresistencia positiva alta a bajas temperaturas, que no satura con el incremento del valor del campo magnético, debido a que los electrones pueden realizar órbitas abiertas en el espacio K lo largo de la superficie de Fermi.

B.6 Resumen general

Como resumen general, observamos que las técnicas *ab initio* permiten describir la física de compuestos cercanos a una transición metal-aislante, o que presentan distintos tipos de conducción según el canal de espín. Asimismo, las propiedades de estructura electrónica y sus variaciones con presión o dopaje pueden ser controlados, y esto nos ayuda a predecir nueva fenomenología y a acercarnos a describir posibles aplicaciones tecnológicas en diversos materiales funcionales.

USC
UNIVERSIDADE
DE SANTIAGO
DE COMPOSTELA

Bibliography

[1] L. H. Thomas, Proc. Cambridge Phil. Soc. **23**, 542 (1927).

[2] E. Teller, Rev. Mod. Phys. **34**, 627 (1962).

[3] V. Fock, Z. Physik **61**, 126 (1930).

[4] J. C. Slater, Phys. Rev. **35**, 210 (1930).

[5] R. G. Parr and W. Yang, *Density-functional theory of atoms and molecules* (Oxford University Press, New York, 1989).

[6] P. Hohenberg and W. Kohn, Phys. Rev. **136**, B864 (1964).

[7] W. Kohn and L. J. Sham, Phys. Rev. **140**, A1133 (1965).

[8] W. Kohn, Rev. Mod. Phys. **71**, 1253 (1999).

[9] M. Born and R. Oppenheimer, Annalen der Physik **84**, 457 (1927).

[10] N. Chamel and P. Haensel, Phys. Rev. C **73**, 045802 (2006).

[11] W. Kohn and L. J. Sham, Phys. Rev. **140**, A1133 (1965).

[12] J. P. Perdew and Y. Wang, Phys. Rev. B **45**, 13244 (1992).

[13] J. P. Perdew, S. Burke, and M. Ernzerhof, Phys. Rev. Lett. **77**, 3865 (1996).

[14] V. Anisimov, F. Aryasetiawan, and A. Lichtenstein, J. Phys. Condens. Matter **9**, 767 (1997).

[15] J. Hubbard, Proc. Roy. Soc. London Ser. A **276**, 238 (1963).

[16] J. Hubbard, Proc. Roy. Soc. London Ser. A **277**, 237 (1964).

[17] J. Hubbard, Proc. Roy. Soc. London Ser. A **281**, 401 (1964).

[18] J. C. Slater, Phys. Rev. **51**, 846 (1937).

[19] O. K. Andersen, Phys. Rev. B **12**, 3060 (1975).

[20] D. D. Koelling and G. O. Arbman, J. Phys. F: Met. Phys. **5**, 2041 (1975).

[21] E. Sjöstedt, L. Nördstrom, and D. J. Singh, Solid State Commun. **114**, 15 (2000).

[22] G. K. H. Madsen, P. Blaha, K. Schwarz, E. Sjöstedt, and L. Nördstrom, Phys. Rev. B **64**, 195134 (2001).

[23] K. Schwarz and P. Blaha, Comp. Mat. Sci. **28**, 259 (2003).

[24] P. Blaha, K. Schwarz, G. K. H. Madsen, D. Kvasnicka, and J. Luitz, *WIEN2k, An Augmented Plane Wave Plus Local Orbitals Program for Calculating Crystal Properties. ISBN 3-9501031-1-2*, Vienna University of Technology, Austria (2001).

[25] J. P. Perdew, S. Kurth, J. Zupan, and P. Blaha, Phys. Rev. Lett. **82**, 2544 (1999).

[26] J. Tao, J. P. Perdew, V. Starovenov, and G. Scuseria, Phys. Rev. Lett. **91**, 146401 (2003).

[27] D. Singh, *Planewaves, pseudopotentials and LAPW method* (Kluwer Academic Publishers, 1994).

[28] A. I. Liechtenstein, V. I. Anisimov, and J. Zaanen, Phys. Rev. B **52**, R5467 (1995).

[29] E. R. Ylvisaker, W. E. Pickett, and K. Koepernik, Phys. Rev. B **79**, 035103 (2009).

[30] G. K. H. Madsen and D. J. Singh, Comp. Phys. Commun. **175**, 67 (2006).

[31] N. W. Ashcroft and N. D. Mermin, *Solid State Physics* (Cornell University, New York, 1975).

[32] E. Pytte, Phys. Rev. B **10**, 4637 (1974).

[33] R. Rückamp, J. Baier, M. Kriener, M. W. Haverkort, T. Lorenz, G. S. Uhrig, L. Jongen, A. Möller, G. Meyer, and M. Grüninger, Phys. Rev. Lett. **95**, 097203 (2005).

[34] M. Shaz, S. van Smaalen, L. Palatinus, M. Hoinkis, M. Klemm, S. Horn, and R. Claessen, Phys. Rev. B **71**, 100405 (2005).

[35] M. Hase, I. Terasaki, and K. Uchinokura, Phys. Rev. Lett. **70**, 3651 (1993).

[36] J. P. Pouget, L. P. Regnault, M. Ain, B. Hennion, J. P. Renard, P. Veillet, G. Dhalenne, and A. Revcolevschi, Phys. Rev. Lett. **72**, 4037 (1994).

[37] K. Hirota, D. E. Cox, J. E. Lorenzo, G. Shirane, J. M. Tranquada, M. Hase, K. Uchinokura, H. Kojima, Y. Shibuya, and I. Tanaka, Phys. Rev. Lett. **73**, 736 (1994).

[38] C. A. Kuntscher, S. Frank, A. Pashkin, M. Hoinkis, M. Klemm, M. Sing, S. Horn, and R. Claessen, Phys. Rev. B **74**, 184402 (2006).

[39] M. K. Forthaus, T. Taetz, A. Möller, and M. Abd-Elmeguid, Phys. Rev. B **77**, 165121 (2008).

[40] S. Blanco-Canosa, F. Rivadulla, A. Piñeiro, V. Pardo, D. Baldomir, D. I. Khomskii, M. M. Abd-Elmeghid, M. A. López-Quintela, and J. Rivas, Phys. Rev. Lett. **102**, 056406 (2009).

[41] S. Blanco-Canosa, F. Rivadulla, V. Pardo, D. Baldomir, J. S. Zhou, M. García-Hernández, M. A. López-Quintela, J. Rivas, and J. B. Goodenough, Phys. Rev. Lett. **99**, 187201 (2007).

[42] V. Pardo, S. Blanco-Canosa, F. Rivadulla, D. I. Khomskii, D. Baldomir, H. Wu, and J. Rivas, Phys. Rev. Lett. **101**, 256403 (2008).

[43] M. Schmidt, W. Ratcliff, P. G. Radaelli, K. Refson, N. M. Harrison, and S. W. Cheong, Phys. Rev. Lett. **92**, 056402 (2004).

[44] L. Palatinus, A. Schoenleber, and S. van Smaalen, Acta Crystallogr., Sect. C: Cryst. Struct. Commun. **61**, i47 (2005).

[45] S. Blanco-Canosa, F. Rivadulla, A. Piñeiro, V. Pardo, D. Baldomir, M. A. López-Quintela, and J. Rivas, J. Magn. Magn. Mater. **322**, 1069 (2010).

[46] A. Piñeiro, V. Pardo, D. Baldomir, S. Blanco-Canosa, F. Rivadulla, J. E. Arias, and J. Rivas, J. Magn. Magn. Mater. **322**, 1072 (2010).

[47] A. Kokalj, J. Mol. Graphics Modell. **17**, 176 (1999).

[48] D. I. Khomskii and K. I. Kugel, Phys. Rev. B **67**, 134401 (2003).

[49] A. Seidel, C. A. Marianetti, F. C. Chou, G. Ceder, and P. A. Lee, Phys. Rev. B **67**, 020405 (2003).

[50] R. Macovez, J. Luzon, J. Schiessling, A. Sadoc, L. Kjeldgaard, S. van Smaalen, D. Fausti, P. H. M. van Loosdrecht, R. Broer, and P. Rudolf, Phys. Rev. B **76**, 205111 (2007).

[51] Y.-Z. Zhang, H. O. Jeschke, and R. Valentí, Phys. Rev. B **78**, 205104 (2008).

[52] C. A. Kuntscher, S. Frank, A. Pashkin, M. Hoffmann, A. Schönleber, S. van Smaalen, M. Hanfland, S. Glawion, M. Klemm, M. Sing, et al., Phys. Rev. B **76**, 241101 (2007).

[53] D. I. Khomskii and T. Mizokawa, Phys. Rev. Lett. **94**, 156402 (2005).

[54] D. Baldomir, V. Pardo, S. Blanco-Canosa, F. Rivadulla, J. Rivas, A. Piñeiro, and J. E. Arias, Physica B **403**, 1639 (2008).

[55] A. Kiswandi, J. S. Brooks, J. Lu, J. Whalen, T. Siegrist, and H. D. Zhou, Phys. Rev. B **84**, 205138 (2011).

[56] H. Tsunetsugu and Y. Motome, Phys. Rev. B **68**, 060405 (2003).

[57] O. Tchernyshyov, Phys. Rev. Lett. **93**, 157206 (2004).

[58] N. B. Perkins and O. Sikora, Phys. Rev. B **76**, 214434 (2007).

[59] E. M. Wheeler, B. Lake, A. T. M. N. Islam, M. Reehuis, P. Steffens, T. Guidi, and A. H. Hill, Phys. Rev. B **82**, 140406(R) (2010).

[60] C. Castelnovo, R. Moessner, and S. L. Sondhi, Nature **451**, 42 (2008).

[61] D. J. P. Morris, D. A. Tennant, S. A. Grigera, B. Klemke, C. Castelnovo, R. Moessner, C. Czternasty, M. Meissner, K. C. Rule, J.-U. Hoffmann, et al., Science **326**, 411 (2009).

[62] G. Giovannetti, A. Stroppa, S. Picozzi, D. Baldomir, V. Pardo, S. Blanco-Canosa, F. Rivadulla, S. Jodlauk, D. Niermann, J. Rohrkamp, et al., Phys. Rev. B **83**, 060402(R) (2011).

[63] Z. Zhang, D. Louca, A. Visinoiu, S.-H. Lee, J. D. Thompson, T. Proffen, A. Llobet, Y. Qiu, S. Park, and Y. Ueda, Phys. Rev. B **74**, 14108 (2006).

[64] J. B. Goodenough, Prog. Solid State Chem. **5**, 145 (1971).

[65] J. M. Recio, R. Franco, A. M. Pendás, M. A. Blanco, L. Pueyo, and R. Pandey, Phys. Rev. B **63**, 184101 (2001).

[66] F. D. Murnaghan, Proc. Natl. Acad. Sci. USA **30**, 244 (1944).

[67] F. Birch, Phys. Rev. **71**, 809 (1947).

[68] M. Reehuis, A. Krimmel, N. Buttgen, A. Loidl, and A. Prokofiev, Eur. Phys. J. B **35**, 311 (2003).

[69] S. Niziol, Phys. Status Solidi A **18**, K11 (1973).

[70] O. Tchernyshyov, R. Moessner, and S. L. Sondhi, Phys. Rev. B **66**, 064403 (2002).

[71] Y. Motome and H. Tsunetsugu, Phys. Rev. B **70**, 184427 (2004).

[72] S. D. Matteo, G. Jackeli, and N. B. Perkins, Phys. Rev. B **72**, 020408 (2005).

[73] T. Maitra and R. Valentí, Phys. Rev. Lett. **99**, 126401 (2007).

[74] Y. Kato, G.-W. Chern, K. A. Al-Hassanieh, N. B. Perkins, and C. D. Batista, Phys. Rev. Lett. **108**, 247215 (2012).

[75] D. Baldomir, V. Pardo, S. Blanco-Canosa, F. Rivadulla, D. I. Khomskii, H. Wu, A. Piñeiro, J. E. Arias, and J. Rivas, J. Magn. Magn. Mater. **321**, 679 (2009).

[76] A. Piñeiro, A. S. Botana, V. Pardo, J. Botana, M. Pereiro, D. Baldomir, and J. E. Arias, J. Appl. Phys. **109**, 07E158 (2011).

[77] C. Kuntscher, K. Rabia, M. K. Forthaus, M. M. Abd-Elmeguid, F. Rivadulla, Y. Kato, , and C. D. Batista, Phys. Rev. B **86**, 020405(R) (2012).

[78] H. J. Xiang and D. J. Singh, Phys. Rev. B. **76**, 195111 (2007).

[79] A. Kiswandhi, J. S. Brooks, J. Lu, J. Whalen, T. Siegrist, and H. D. Zhou, Phys. Rev. B **84**, 205138 (2011).

[80] R. B. Kaner, J. J. Gilman, and S. H. Tolbert, Science **308**, 1268 (2005).

[81] W. P. Tong, N. R. Tao, Z. B. Wang, J. Lu, and K. Lu, Science **299**, 686 (2003).

[82] J. C. Grossman, A. Mizel, M. Côté, M. L. Cohen, and S. G. Louie, Phys. Rev. B **60**, 6343 (1999).

[83] A. Filippetti and N. A. Hill, Phys. Rev. Lett. **85**, 5116 (2000).

[84] L. M. Corliss, N. Elliott, and J. M. Hastings, Phys. Rev. **117**, 929 (1960).

[85] F. Rivadulla, M. Bañobre-López, C. X. Quintela, A. Piñeiro, V. Pardo, D. Baldomir, M. A. López-Quintela, J. Rivas, C. A. Ramos, H. Salva, et al., Nature Mater. **8**, 947 (2009).

[86] J. B. Goodenough, *Magnetism and the Chemical Bond* (Wiley, 1963).

[87] P. W. Anderson, Phys. Rev. **79**, 350 (1950).

[88] P. W. Anderson, Phys. Rev. **79**, 705 (1950).

[89] C. Zener, Phys. Rev. **81**, 440 (1951).

[90] C. Zener, Phys. Rev. **82**, 403 (1951).

[91] J. B. Goodenough, Phys. Rev. **100**, 564 (1955).

[92] J. B. Goodenough, Phys. Rev. **117**, 1442 (1960).

[93] N. F. Mott, Proc. Phys. Soc. A **62**, 416 (1949).

[94] N. F. Mott, Rev. Mod. Phys. **40**, 677 (1968).

[95] P. G. de Gennes, Phys. Rev. **141**, 141 (1960).

[96] E. Dagotto, T. Hotta, and A. Moreo, Phys. Rep. **344**, 1 (2001).

[97] C. N. R. Rao and B. Raveau, *Colossal Magnetoresistance, Charge Ordering and Related Properties of Manganese Oxides* (Singapore: World Scientific, 1998).

[98] V. B. Shenoy, T. Gupta, H. R. Krishnamurthy, and T. V. Ramakrishnan, Phys. Rev. Lett. **98**, 097201 (2007).

[99] E. Dagotto, Science **309**, 257 (2005).

[100] W. Wu, C. Israel, N. Hur, S. Park, S.-W. Cheong, and A. D. Lozanne, Nature Mater. **5**, 881 (2006).

[101] M. Bowen, M. Bibes, A. Barthelemy, J. P. Contour, A. Anane, Y. Lemaitre, and A. Fert, Appl. Phys. Lett. **82**, 233 (2003).

[102] E. Y. Tsymbal and H. Kohlstedt, Science **313**, 181 (2006).

[103] W. Eerenstein, M. Wiora, J. L. Prieto, J. F. Scott, and N. Mathur, Nature Mater. **6**, 348 (2007).

[104] S.-W. Cheong and H. Hwang, *Ferromagnetism vs Charge/Orbital Ordering in Mixed-Valent Manganites, in Colossal Magnetoresistance Oxides* (Gordon & Breach, Monograps in Condensed Matter Science, London, 1999).

[105] H. D. Zhang, M. Li, Y. K. An, Z. H. Mai, J. Gao, F. X. Hu, Y. Wang, and Q. J. Jia, J. Phys. D: Appl. Phys. **40**, 2723 (2007).

[106] E. Herrero, J. Alonso, J. L. Martínez, M. Vallet-Regí, and J. M. González-Calbet, Chem. Mater. **12**, 1060 (2000).

[107] P. Schiffer, A. P. Ramirez, W. Bao, and S.-W. Cheong, Phys. Rev. Lett. **75**, 3336 (1995).

[108] F. Rivadulla, M. Otero-Leal, A. Espinosa, A. de Andres, C. Ramos, J. Rivas, and J. B. Goodenough, Phys. Rev. Lett. **96**, 016402 (2006).

[109] A. Moreo, S. Yunoki, and E. Dagotto, Science **283**, 2034 (1999).

[110] E. Dagotto, *Nanoscale Phase Separation and Colossal Magnetoresistance. The Physics of Manganites and Related Compounds* (Springer, Berlin, 2003).

[111] M. Hennion, F. Moussa, P. Lehouelleur, F. Wang, A. Ivanov, Y. M. Mukovskii, and D. Shulyatev, Phys. Rev. Lett. **94**, 057006 (2005).

[112] J. Tao, D. Niebieskikwiat, M. Varela, W. Luo, M. A. Schofield, Y. Zhu, M. B. Salamon, J. M. Zuo, S. T. Pantelides, and S. J. Pennycook, Phys. Rev. Lett. **103**, 097202 (2009).

[113] V. J. Emery, S. A. Kivelson, and H. Q. Lin, Phys. Rev. Lett. **64**, 475 (1990).

[114] W. K. Yeoh, B. Gault, X. Y. Cui, C. Zhu, M. P. Moody, L. Li, R. K. Zheng, W. X. Li, X. L. Wang, S. X. Dou, et al., Phys. Rev. Lett. **106**, 247002 (2011).

[115] M. J. Han, T. Ozaki, and J. Yu, Phys. Rev. B **73**, 045110 (2006).

[116] W. S. Choi, D. G. Kim, S. S. A. Seo, S. J. Moon, D. Lee, J. H. Lee, H. S. Lee, D.-Y. Cho, Y. S. Lee, P. Murugavel, et al., Phys. Rev. B **77**, 045137 (2008).

[117] A. Piñeiro, V. Pardo, D. Baldomir, A. Rodríguez, R. Cortés-Gil, A. Gómez, and J. E. Arias, J. Phys. Condens. Matter **24**, 275503 (2012).

[118] J. Alonso, E. Herrero, J. M. González-Calbet, M. Vallet-Regí, J. L. Martínez, J. M. Rojo, and A. Hernando, Phys. Rev. B **62**, 11328 (2000).

[119] J. M. Alonso, A. Arroyo, J. M. González-Calbet, A. Hernando, J. M. Rojo, and M. Vallet-Regí, Chem. Mater. **15**, 2864 (2003).

[120] L. M. Rodriguez-Martinez and J. P. Attfield, Phys. Rev. B **54**, R15622 (1996).

[121] J. Fontcuberta, V. Laukhin, and X. Obradors, Appl. Phys. Lett. **72**, 2607 (1999).

[122] R. Cortés-Gil, J. M. Alonso, M. L. Ruiz-González, M. Vallet-Regí, A. Hernando, and J. M. González-Calbet, Chem. Mater. **20**, 3398 (2008).

[123] C.-H. Yang, J. H. Song, S. H. Park, Y. N. Choi, C.-H. Lee, and Y. H. Jeong, J. Phys. Soc. Jpn. **73**, 3051 (2004).

[124] A. Piñeiro, V. Pardo, D. Baldomir, F. Rivadulla, A. Rodríguez, A. Gómez, J. E. Arias, and J. Rivas, Phys. Status Solidi C **7**, 2620 (2010).

[125] D. I. Khomskii and K. I. Kugel, Europhys. Lett. **55**, 208 (2001).

[126] M. I. Katsnelson, V. Y. Irkhin, L. Chioncel, A. I. Lichtenstein, and R. A. de Groot, Rev. Mod. Phys. **80**, 315 (2008).

[127] K. Schwarz, J. Phys. F: Met. Phys. **16**, L211 (1986).

[128] S. Wolf, D. Awschalom, R. Buhrman, J. Daughton, S. von Molnár, M. Roukes, A. Chtchelkanova, and D. Treger, Science **294**, 1488 (2001).

[129] R. A. de Groot, F. M. Mueller, P. G. van Engen, and K. H. J. Buschow, Phys. Rev. Lett. **50**, 2024 (1983).

[130] G. L. Zhao, J. Callaway, and M. Hayashibara, Phys. Rev. B **48**, 15781 (1993).

[131] I. I. Mazin, Appl. Phys. Lett. **77**, 3000 (2000).

[132] S. K. Kwon, S. J. Youn, and B. I. Min, Phys. Rev. B **62**, 357 (2000).

[133] T. Shishidou, A. J. Freeman, and R. Asahi, Phys. Rev. B **64**, 180401(R) (2001).

[134] Y. J. Jin and J. I. Lee, Phys. Rev. B **73**, 064405 (2006).

[135] N. Wu, Y. B. Losovyj, D. Wisbey, K. Belashchenko, M. Manno, L. Wang, C. Leighton, and P. A. Dowben, J. Phys. Condens. Matter **19**, 156224 (2007).

[136] M. J. M. de Jong and C. W. J. Beenakker, Phys. Rev. Lett. **74**, 1657 (1995).

[137] L. Wang, T. Y. Chen, and C. Leighton, Phys. Rev. B **69**, 094412 (2004).

[138] L. Wang, K. Umemoto, R. M. Wentzcovitch, T. Y. Chen, C. L. Chien, J. G. Checkelsky, J. C. Eckert, E. D. Dahlberg, and C. Leighton, Phys. Rev. Lett. **94**, 056602 (2005).

[139] K. Umemoto, R. M. Wentzcovitch, L. Wang, and C. Leighton, Phys. Stat. Sol. B **243**, 2117 (2006).

[140] C. Utfeld, S. R. Giblin, J. W. Taylor, J. A. Duffy, C. Shenton-Taylor, J. Laverock, S. B. Dugdale, M. Manno, C. Leighton, M. Itou, et al., Phys. Rev. Lett. **103**, 226403 (2009).

[141] P. J. Brown, K.-U. Neumann, A. Simon, F. Ueno, and K. R. A. Ziebeck, J. Phys. Condens. Matter **17**, 1583 (2005).

[142] T. Takahashi, Y. Naitoh, T. Sato, T. Kamiyama, K. Yamada, H. Hiraka, Y. Endoh, M. Usuda, and N. Hamada, Phys. Rev. B **63**, 094415 (2001).

[143] M. Otero-Leal, F. Rivadulla, M. García-Hernández, A. Piñeiro, V. Pardo, D. Baldomir, and J. Rivas, Phys. Rev. B **78**, 180415(R) (2008).

[144] P. Mavropoulos, K. Sato, R. Zeller, P. Dederichs, V. Popescu, and H. Ebert, Phys. Rev. B **69**, 054424 (2004).

[145] V. Pardo and W. E. Pickett, Phys. Rev. B **80**, 054415 (2009).

[146] R. W. G. Wyckoff, *Crystal Structures, Vol. 1* (Interscience, New York, 1965).

[147] R. Yamamoto, A. Machida, Y. Morimoto, and A. Nakamura, Phys. Rev. B **59**, R7793 (1999).

[148] S. Saha, M. D. Raychaudhury, and T. Saha-Dasgupta, Phys. Rev. B **77**, 155428 (2008).

[149] E. S. Stoner, Proc. R. Soc. **165**, 372 (1938).

[150] P. Fazekas, *Lecture Notes on Electron Correlation and Magnetism* (World Scientific Publishing Co. Pte. Ltd., Singapore, 1999).

[151] V. N. Antonov, O. V. Andryushchenko, A. P. Shpak, A. N. Yaresko, and O. Jepsen, Phys. Rev. B **78**, 094409 (2008).

[152] T. Muro, T. Shishidou, F. Oda, T. Fukawa, H. Yamada, A. Kimura, S. Imada, and S. Suga, Phys. Rev. B **53**, 7055 (1996).

[153] A. Piñeiro, A. S. Botana, V. Pardo, and D. Baldomir, J. Phys. Condens. Matter **22**, 505602 (2010).

[154] P. J. Feibelman, J. A. Appelbaum, and D. R. Hamann, Phys. Rev. B **20**, 1433 (1979).

[155] T. Moriya, *Spin Fluctuations in Itinerant Electron Magnetism* (Springer-Verlag, Berlin, 1985).

[156] M. Otero-Leal, F. Rivadulla, S. S. Saxena, K. Ahilan, and J. Rivas, Phys. Rev. B **79**, 060401 (2009).

[157] H. Ebert and G. Schütz, J. Appl. Phys. **69**, 4627 (1991).

[158] L. Chioncel, M. Katsnelson, R. de Groot, and A. Lichtenstein, Phys. Rev. B **68**, 144425 (2003).

[159] F. Rivadulla, private communication (2010).